Fast simulation of grain growth based on OrientatedTessellation Updating Method and probabilistic homogenization

Sofia Sakout

École doctorale n°531 : SCIENCES, INGÉNIERIE ET ENVIRONNEMENT (SIE)

Doctorat ParisTech

THÈSE

pour obtenir le grade de docteur délivré par

l'École des Ponts ParisTech

Spécialité doctorale "Science des Matériaux"

présentée et soutenue publiquement par

Sofia SAKOUT

le 22 Octobre 2020

Energetic upscaling strategy for grain growth

Directeur de thèse : **Alain EHRLACHER**

Co-directeur de thèse : **Daniel WEISZ-PATRAULT**

Jury

Samuel Forest,	DR CNRS	Rapporteur
Benoit Appolaire,	Professeur	Rapporteur
Marc Bernacki,	Professeur	Examinateur
Véronique Doquet,	DR CNRS	Examinatrice
Romain Quey,	CR CNRS	Examinateur
Alain Ehrlacher,	Professeur	Directeur
Daniel Weisz-Patrault,	CR CNRS	Co-directeur

Ponts ParisTech, Laboratoire NAVIER

École Polytechnique, Laboratoire de Mécanique des Solides (LMS)

THESE

Contents

List of figures

List of tables

In memory of my beloved grandmother,
I dedicate this work to you Mamie

Acknowledgements

This work would not have been possible without the help and support of some wonderful people.

First of all I would like to thank Daniel Weisz-Patrault, who was present every step of the way. He was a teacher and a mentor, but also a life coach sometimes. It is an honor for me to work with him, and a great opportunity to learn from him.

I would also like to thank Alain Ehrlacher for all his guidance. I remember that one time where we were stuck for few months, and after only one meeting with Alain, everything fell into place and we were able go back on track.

And of course, I would not be where I am now now without the love and support of my family and friends. A special thanks to my mom, to and Hind and Nabil for always being there for me and for always believing in me even when I didn't believe in myself.

I would also like to thank my babies:(i) Rami who took very good care of me, he was always there to cheer me up, to cook for me and to ask me to " believe in him who believed in me". And (ii) Imane, who is more a sister than a friend to me, I will always cherish our long talks and our live working sessions.

I am particularly grateful to les Bichons, especially dob's lo and Mathieu lo, who provided me with moral support and shared their work place with me.

A special thanks goes to the Wolf-Mandroux family, my family in France. Thank you Françoise and Philippe for everything.

Finally, I wish to thank the rest of my friends, Naji, Hamid, Hanane, Karim and Ayoub for their support.

Résumé en français

Modèle mésoscopique rapide de croissance de grain par mise à jour de tessellations orientées et homogénéisation probabiliste

La croissance de grain est un phénomène thermiquement activé qui se produit généralement pendant les phases de recuit des métaux, où le temps de maintien à une température suffisante permet aux joints de grain de gagner en mobilité. Pendant la phase de croissance, certains grains grossissent au détriment d'autres grains en fonction de leur taille et de leur orientation cristalline, dont dépend l'énergie de joint de grain. Les descripteurs statistiques classiques du polycristal tels que la texture morphologique et cristallographique (taille des grains, distribution des orientations et des désorientations cristallines etc.) évoluent pendant les procédés. Ainsi, pour différents procédés de fabrication ou de mise en forme, les conditions de température pourraient être optimisées pour viser des microstructures, en particulier pour les procédés présentant des hétérogénéités spatiales. On peut penser par exemple aux procédés de fabrication additive pour lesquels la formation et l'évolution des microstructures est un enjeu majeur pour garantir les caractéristiques matériaux souhaitées, et dont le contrôle en cours de procédé serait une avancée significative.

Cependant, contrôler les microstructures en optimisant les procédés de fabrication est un défi de taille pour les industries des métaux. En effet, prédire l'évolution des microstructures implique de développer des modèles à l'échelle du polycrystal et notamment des joints de grain, qui est l'échelle pertinente pour décrire correctement les phénomènes mis en jeu. Cependant cette échelle est incompatible avec des simulations complètes de procédés qui nécessitent une description à large échelle.

Ces travaux de thèse visent donc à développer une stratégie de changement d'échelle pour établir les bases d'un modèle macroscopique de croissance de grain qui repose entièrement sur une description du phénomène aux échelles inférieures et dont les variables d'état contiennent les descripteurs statistiques du polycristal. Cette stratégie repose essentiellement sur une description de la croissance de grain à différentes échelles : (i) à l'échelle atomique (potentiel interatomique et arrangement cristallin), (ii) à l'échelle microscopique (joints de grain), (iii) à l'échelle mésoscopique (polycristal) et (iv) à l'échelle macroscopique (descripteurs statistiques de la microstructure).

Puisque les concepts énergétiques existent à toutes les échelles et traversent tous les champs de la physique, notre stratégie repose en substance sur différentes contributions énergétiques apparaissant aux différentes échelles. Cette stratégie énergétique est dévelop-

pée dans le cadre des milieux standard généralisés qui sont caractérisés par leur énergie libre et la puissance dissipée dans n'importe quelle évolution virtuelle. Ces deux potentiels apparaissent dans la forme locale de l'équation des bilans thermodynamiques qui combine le premier et le second principe, et qui fait intervenir les variables d'état macroscopique qui doivent être définies pour que l'état macroscopique du système représente statistiquement le polycristal. La détermination de l'énergie libre macroscopique et du potentiel de dissipation en fonction des variables d'état permet d'établir la loi d'évolution du système. La stratégie développée dans ce travail de thèse consiste à déterminer ces potentiels thermodynamiques non pas de manière axiomatique avec des fonctions paramétriques et une nécessaire calibration expérimentale, mais de manière plus physique et statistique en s'appuyant sur la construction d'une importante base de données constituée de calculs à l'échelle mésoscopique. Contrairement aux approches en champ moyen qui représentent le polycristal de manière simplifiée au moyen de classe de grains, on s'appuie ici sur une description détaillée des polycristaux. Ainsi, l'idée majeure qui sous-tend ce travail est que le modèle à l'échelle macroscopique émerge d'une description aux plus fines échelles.

Notre approche diffère de certaines stratégies multiéchelles pour lesquelles des simulations à l'échelle mésoscopique sont appelées pendant un calcul macroscopique. Au contraire, dans ce travail, tous les calculs à l'échelle mésoscopique sont réalisés en avance et stockés dans la base de données qui a vocation à sonder l'espace des structures polycristallines. Sur cette base, nous pouvons identifier une énergie libre et un potentiel de dissipation macroscopiques en fonction de variables d'état que nous définirons, pour obtenir une loi d'évolution macroscopique qui porte sur les descripteurs statistiques de la microstructure.

La base données joue donc un rôle déterminant et nécessite pour être suffisamment riche d'utiliser intensivement un modèle de croissance de grain à l'échelle mésoscopique. Le temps de calcul de ce modèle est donc critique. Bon nombre d'approches existent : les automates cellulaires et les méthodes de Monte Carlo, les éléments finis mobiles, les méthodes par fonction de niveau, les méthodes en champs de phase ou encore la dynamique moléculaire. Ces approches permettent d'étudier en détails les phénomènes de croissance de grain et d'y inclure une physique détaillée qui permet éventuellement de capturer d'autres phénomènes (recristallisation, transitions de phase etc.). Cependant, le poids calculatoire est trop important pour que l'une de ces approches puisse être raisonnablement utilisée dans le cadre théorique que nous avons décrit.

Ainsi le premier axe de travail, guidant ce mémoire de thèse, tient au développement d'un modèle mésoscopique simple et suffisamment rapide pour créer la base de données qui sous-tend notre stratégie de changement d'échelle. Ce modèle est formulé en deux dimensions dans ce travail pour ne pas compliquer les aspects techniques, l'enjeu étant principalement de valider notre approche. Nous nous appuyons sur les techniques de tessellations de Voronoi-Laguerre qui sont habituellement utilisées pour approcher la morphologie des polycristaux. Des algorithmes très efficaces ont été développés et permettent de générer très rapidement des tessellations. De plus, on peut assigner à chaque grain une orientation cristalline pour obtenir une tessellation orientée. L'idée de notre modèle mésoscopique rapide est donc d'approximer l'évolution d'un polycristal par une succession des tessellations orientées, que l'on met à jour à chaque pas de temps. Ainsi, la méthode repose sur une formulation d'une loi d'évolution formulée directement sur les paramètres qui pilotent la tessellation orientée. Cette loi d'évolution est obtenue dans un cadre ther-

modynamique rigoureux en sommant les énergies anisotropes des joints de grain dans le polycristal (force motrice) et les puissances dissipées dans n'importe quel mouvement virtuel des joints (force résistive). Ainsi, un lien substantiel est fait entre les échelles atomique, microscopique et mésoscopique.

Le second axe de travail tient quant à lui à l'exploitation de la base de données de calculs à l'échelle mésoscopique pour identifier des variables d'état macroscopiques pertinentes ainsi que l'énergie libre et le potentiel de dissipation macroscopique dans le cadre théorique que nous avons décrit. Un aspect important est que la perte d'information entre l'échelle mésoscopique (détaillée) et l'échelle macroscopique (statistique) introduit un aléa épistémique dans le modèle, car à un unique état macroscopique statistique, correspond une multitude d'états mésoscopiques différents. Donc, à partir d'un modèle mésoscopique entièrement déterministe, nous construisons un modèle macroscopique probabiliste, qui peut être utilisé pour des structures de grande échelle subissant des traitements thermiques.

Chapter 1

General introduction

« *We keep moving forward, opening new doors, and doing new things, because we're curious and curiosity keeps leading us down new paths.* »

Walt Disney

Contents

1.1 Recrystallization and the related annealing phenomena

In 1994, in the first edition of their book [2], John Humphreys and Max Hatherly wrote: *Recrystallization and the related annealing phenomena which occur during the thermomechanical processing of materials have long been recognized as being both of technological importance and scientific interest. These phenomena are known to occur in all types of crystalline materials; they occur during the natural geological deformation of rocks and minerals, and during the processing of technical ceramics.* More than 25 years later, these lines remain accurate. Indeed, in spite of significant advances in the field of *recrystallization and related annealing phenomena*, continuously renewed technological issues and scientific questions arise.

One can summarize schematically the annealing processes as follows. After significant deformation, materials are characterized by a high dislocation density, each of which stores elastic energy. Thus, the bulk energy is significant, which acts as a driving force for the polycrystalline structure to rearrange and annihilate dislocations. However, at room temperature the dissipation cost for dislocations to move acts as a resistive force that hinders annihilation and rearrangement of dislocations. On the contrary, when temperature is maintained at an elevated value, the dissipation cost decreases and dislocations can move, rearrange and annihilate. This process is called recovery as materials properties are partially restored with respect to the deformed materials (hardening etc.). The changes occurring during recovery are homogeneous and do not affect the already existing grain boundaries. The dislocation structure is not completely removed and a sub-grain structure takes place, as shown in figure 1.1a. Then, new dislocation-free grains nucleate and grow within this recovered structure (see. figure 1.1a). This phase is called recrystallization as the a new grain structure is formed. It should be noted that in this new grain structure the dislocation density is very low and therefore the bulk energy is negligible. The energy stored in the structure is mainly carried by the grain boundaries. This energy acts as a driving force for grains to grow in order to decrease the total grain boundary length in the structure. Thus, grain growth is a thermally activated mechanism that usually occurs after recrystallization during annealing. During grain growth some grains grow at the expense of other grains depending of their respective sizes and crystallographic orientations, which leads to grain coarsening (see. figure 1.1a).

Among countless interesting problems related to this field, we focus in this PhD thesis on modeling strategies to simulate grain growth at different scales, which is relevant to various class of materials such as sintered, cast, vapor deposited materials or additively manufactured. Thus, we do not deal with recovery and recrystallization mechanisms (static or dynamic) and we limit our investigation to grain growth. Both normal and abnormal grain growth[1], are considered as a single phenomenon that mainly differ by local grain structure and crystal orientation field. In addition, we consider in this PhD thesis fairly complex polycrystalline structures as obtained by several fabrication processes as additive manufacturing processes. Indeed, the deposition of liquid metal on a recrystallized substrate leads to a solidification process that favor columnar grains with specific crystal orientations, as shown in figure 1.1b. The fully crystallized structure often presents high morphological and crystallographic textures with very elongated grains and very small equiaxed grains (see. 1.1b). Thus, the ideas presented in this work have been developed also with

[1] which corresponds to homogeneous growth, and selective growth of a few large grains respectively

such processes in mind, which explains the large variety of polycrystalline structures that have been considered.

In addition, even though the theoretical developments proposed in this work are not limited to metals and may apply to grain growth in general, we refer in the text to metals, and especially to pure iron for numerical results. This choice is consistent with current researches on metallic additive manufacturing processes in Solid Mechanics Laboratory (LMS) and enables the reader to follow the proposed strategy with a specific class of material in mind and potential applications.

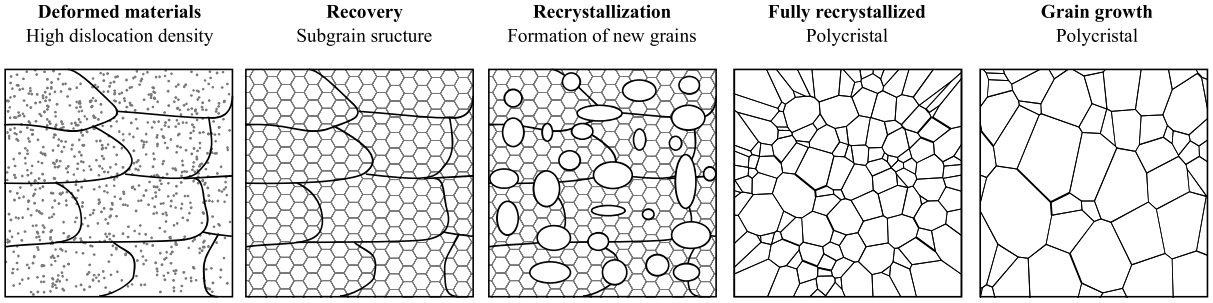

(a) Recovery, recrystallization and grain growth during annealing

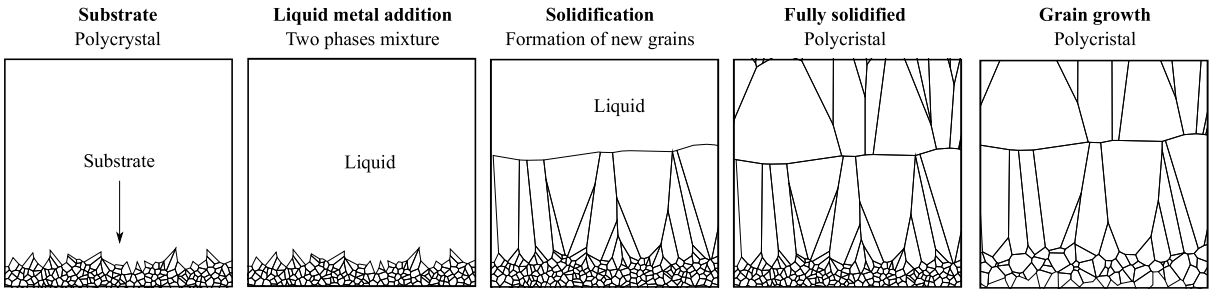

(b) Solidification and grain growth during additive manufacturing process.

Figure 1.1: Schematic processes of annealing phenomena.

1.2 Scientific program

Classical statistical descriptors of the polycrystalline structure such as morphological and crystallographic textures (e.g., grain size, shape and crystal orientation distributions) evolve during the process. Thus, for different fabrication or forming processes, temperature conditions could be optimized to obtain targeted microstructures, especially for large heterogeneous parts. For instance one can think of additive manufacturing processes for which the formation and evolution of polycrystalline structure is a significant issue to target specific material properties, and whose control during the process would be a major advance. However, mechanisms involved during grain growth arise at the scale of grain boundaries (GB). Thus, numerical simulations of the evolution of morphological and crystallographic textures may be difficult to perform for macroscopic parts, which hinders the development of optimization loops to adjust process parameters.

Thus, this PhD thesis aims at developing an upscaling strategy to establish a macroscopic model of grain growth that fully relies on finer scales and whose state variables

contain statistical descriptors of the grain structure. The proposed upscaling strategy involves considering grain growth at various scales. As shown in figure 1.2, four typical scales are distinguished in this work: (i) the atomic scale (e.g., crystal lattice and interatomic potential), (ii) the microscopic scale (e.g., grain boundaries), (iii) the mesoscopic scale (e.g., polycrystalline structure) and (iv) the macroscopic scale (statistical descriptors of the grain structure). As energetic concepts are valid at all scales, the upscaling strategy fundamentally relies on various energetic contributions arising at different scales. This energetic upscaling strategy is developed within the framework of standard generalized media [4] that are characterized by their free energy and dissipated power. These two potentials arise in the energy balance equation combining the first and second laws of thermodynamics, and they depend on macroscopic state variables that should be defined so that the macroscopic state statistically represents the grain structure. The determination of the macroscopic free energy and dissipation potentials as a function of the state variables enables to establish the evolution law of the system at the macroscopic scale. The proposed upscaling strategy consists in determining these two potentials not axiomatically (with parametric functions and calibration with experiments), but on a more physical basis by using a large database of computations carried out at the mesoscopic scale. Thus, the macroscopic model emerges from finer scales and is compatible with thermodynamics.

It should be noted that we do not propose a multiscale approach, for which simulations at the mesoscopic scale are performed online during the macroscopic computation. On the contrary, all the computations at the mesoscopic scale are performed in advance and stored in the database probing the space of polycrystalline structures. On this basis, we can identify the macroscopic free energy and dissipated power as a function of the macroscopic state variables in order to obtain an evolution law that accounts for statistical descriptors of the grain structure.

Therefore, the database requires to use intensively a mesoscopic model of grain growth. As a consequence, a sufficiently fast mesoscopic model should be established. In chapter 3 we will specifically focus on this aspect, whereas the identification of the macroscopic model will be broached in chapter 4. Many different approaches have been proposed to model grain growth at the mesoscopic scale (e.g., see [2, 5] for reviews). Most of them rely on the classical curvature driven GB motion evolution law:

$$v_{CD} = m_{CD}\,\gamma\,\kappa \tag{1.1}$$

where v_{CD} is the inward speed of the GB (where CD stands for *curvature driven*), m_{CD} is the mobility ($\mathrm{m}^4.\mathrm{J}^{-1}.\mathrm{s}^{-1}$), γ is the surface energy ($\mathrm{J.m}^{-2}$) and κ is the grain curvature. Since this evolution law holds at the scale of the GB, many numerical approaches enable to refine the geometrical description of GBs in order to capture accurately GB motion. For instance, models based on cellular automaton and Monte Carlo method [6–10], mobile finite element modeling [11, 12], level set functions [13–15], phase field [16–21] or molecular dynamics [22–24] have been proposed. All these approaches produce very interesting results. However, the computational cost is usually incompatible with an intensive use as suggested within the proposed framework.

Other approaches reaching shorter computation time have also been proposed. For instance, vertex methods [25–28] consist in establishing the evolution law directly at the triple junctions and are relatively simple in two dimensions. However, the extension in three dimensions is difficult [2]. In this work (see. chapter 3), a fast mesoscopic model

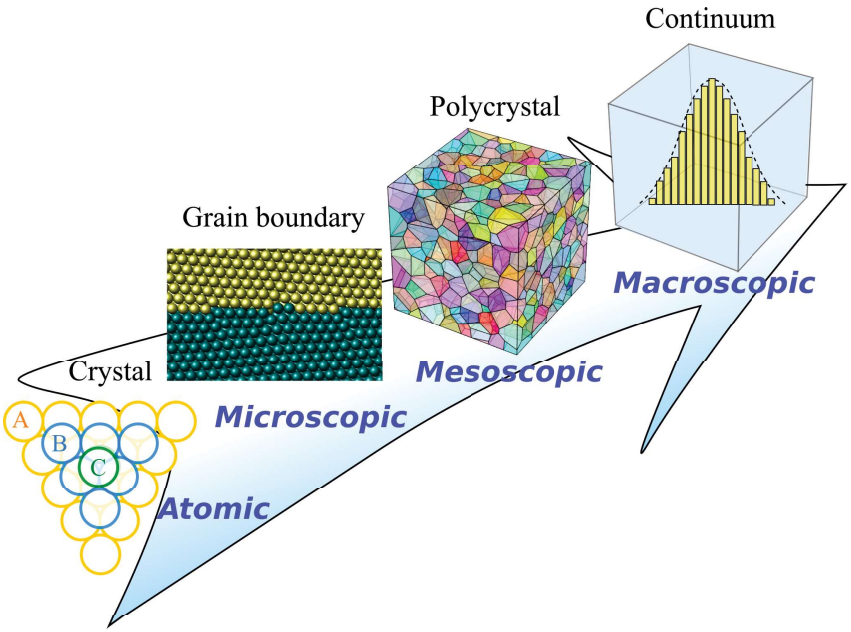

Figure 1.2: Different scales involved in the upscaling strategy

called *Orientated Tessellation Updating Method* (OTUM) has been proposed, and fully relies on Voronoi-Laguerre tessellation techniques that are usually used to approximate polycrystals at the mesoscopic scale. Very efficient algorithms have been developed with the possibility of controlling statistical distributions of grain size and shape (e.g., using the free software NEPER [29]). Crystal lattice orientation can also be specified for each grain, and the tessellation equipped with such an orientation field is called an *Orientated Tessellation* (OT). One can approximate the real evolution of the mesoscopic structure as a succession of OT approximations. OTUM relies on the idea that the evolution law of the mesoscopic structure can be formulated directly by modifying the parameters defining the OT.

To the best of our knowledge this idea of updating Voronoi-Laguerre tessellation parameters to model grain growth has been proposed for the first times in [30, 31]. However, the evolution laws proposed in [30, 31] are questionable. Indeed, they are postulated to directly mimic the curvature driven evolution law (1.1) despite the fact that GBs have no curvature in a Voronoi-Laguerre tessellation. More importantly, the modification of a single parameter of the OT affects several GBs according to the Voronoi-Laguerre definition, which plays the role of a geometrical constraint on possible GB motions. Thus, the curvature driven evolution law (1.1) is not appropriate within the framework of OTUM, as it would necessitate to control GBs independently.

That is why in chapter 3, the evolution law is formulated at the mesoscopic scale (i.e., for the entire tessellation instead of each GB taken individually). Different energetic contributions are considered so that the evolution law relies on a physically consistent basis. More precisely, the evolution law is obtained through the energy balance equation at the mesoscopic scale, by specifying mechanisms at the microscopic scale: (i) the anisotropic GB energy and (ii) the dissipated power through any GB virtual motion. The proposed energetic framework enables to consider not only the driving force (associated to the GB energy) but also the dissipated power as a resistive mechanism. The GB energy is estimated as a function of misorientation by molecular dynamics computations at the atomic scale.

In addition, the dissipated power associated to GB motion is estimated by crystal plasticity for very low angle boundaries and atomic jumps and atomic diffusion are considered for high and intermediate angle boundaries respectively. Thus, a substantial link is made in this work between atomic, microscopic and mesoscopic scales to derive the model.

From the macroscopic point of view, all the mesoscopic structures play the role of representative volume elements (RVE). This implies that each mesoscopic structure is supposed to be extracted from a much larger polycrystalline structure. As a result, boundary conditions should be applied to the RVE to take into account interactions between the RVE and the rest of the polycrystal. This is achieved by defining the RVE as a subset of grains extracted from a larger OT, so that misorientations are affected to GBs at the edges of the RVE.

In addition, the set of possible OTs is a high dimensional vector space. Thus, the database should contain various RVEs sufficiently different from each other to probe efficiently the space of possible OTs. However, as detailed in chapter 3, if crystal orientations are assigned purely randomly, then boundary misorientation distributions (BMD) are likely to be very similar to each other instead of spreading in the entire space of possible distributions. To overcome this difficulty, crystal orientations are assigned according to a specific procedure in order to match prescribed BMDs.

For the sake of simplicity, the proposed upscaling methodology is derived for plane hexagonal polycrystals. In 3D, this would correspond to face-centered cubic (fcc) crystals, and for each grain the direction [111] is assumed to be aligned with the out of plane direction. Thus, there are three plastic slip systems in 2D, as shown in figure 1.3. Misorientation between two neighboring grains (characterized by five parameters in 3D) is characterized only by two parameters in 2D: the misorientation angle (denoted by $\Delta\theta$) and the orientation of the grain boundary plane (denoted by φ). Thus, the grain boundary energy considered in this PhD thesis is computed from fcc crystals sharing the same orientation $\langle 111 \rangle$ (tilt boundaries). The plane assumption enables to deal with thin structures such as thin films. In addition, since there are 3 plastic slip systems in the plane, the proposed approach also enables to reasonably approximate 3D structures.

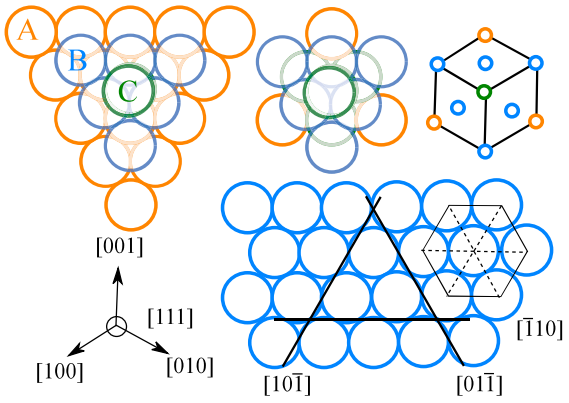

Figure 1.3: FCC crystal and (111) plane with plastic slip directions

The final step enabling to extend this energetic upscaling to the macroscopic scale will be broached in chapter 4. This step requires to reduce the amount of data to be processed at each material point of the macroscopic domain. This is performed by considering sta-

tistical estimators of the polycrystalline structure. In practice the successive statistical moments of the misorientations weighted by the GB lengths are introduced. Macroscopic state variables are defined as the macroscopic counterparts of such a reduced mesoscopic state. The key ingredient to obtain purely macroscopic state variables (i.e., that do not rely on the mesoscopic state) is to determine macroscopic evolution laws, which enable to determine the evolution of the macroscopic state variables considering only their initial values. These evolution laws are rigorously determined in chapter 4 by using the using the very definition of the reduced mesoscopic state and the mesoscopic evolution law identified in chapter 3. Several quantities arise in the obtained macroscopic evolution laws, namely the total energy at the macroscopic scale and a macroscopic mobility tensor. These quantities are identified based on the large database of mesoscopic computations. The identification of the total energy is fairly simple, as an analytic computation provides (for a simplified situation) an analytic interpolation function, which revealed to lead to an almost perfect fit between the interpolation model and the data. On the contrary, most of the modeling efforts in chapter 4 are dedicated to the identification of the macroscopic mobility tensor. Indeed, since most of the information carried by the comprehensive mesoscopic state is lost in the macroscopic state, a single macroscopic state may correspond to various different mesoscopic states. Thus, an epistemic uncertainty arises, which corresponds to the loss of information in the process of reducing the amount of data. This epistemic uncertainty has been modeled with random variables, leading to a probabilistic macroscopic model. Technically, the probabilistic identification of the macroscopic mobility tensor involved in the macroscopic evolution law has been carried out by using classical Bayesian inference. Thus, the main output of the proposed macroscopic model is the mean and point-wise standard deviation of the macroscopic variables. Somme comparisons with mesoscopic evolutions show that the macroscopic model is satisfying and can be used for various applications such as forming and fabrication processes.

1.3 Outline of the thesis

A brief literature review is provided in chapter 2. The mesoscopic model (OTUM) is detailed in chapter 3, and the probabilistic macroscopic model is developed in chapter 4. A general conclusion is given in chapter 5. Appendices are also provided in Appendix A.

Chapter 2

Literature review

« *Change is the law of life. And those who look only to the past or present are certain to miss the future.* »

J. F. Kennedy

Contents

In this chapter, a concise literature review is presented. The literature related to annealing process and related phenomena is particularly rich and cannot be exhaustively presented in this PhD thesis. The subject tackled in this brief review concerns grain growth, more precisely the modeling aspects and the different numerical approaches used to produce realistic simulations. Phenomenological and experimental aspects of grain growth are not covered in this chapter, as well as the complexity of multiphase materials. Nevertheless, the proposed review enables to contextualize our research project in the already existing scientific field, and to enlighten our motivations as well as the advantages and the limitations of the proposed work.

This review mostly relies on the book [2]. Therefore, this chapter does not contain original results or concepts and can easily be skipped by a reader that is familiar with grain growth and the associated numerical methods and the related challenges. Our aim is purely educational so that the reader can compare the well known models and numerical methods with the work developed in this PhD thesis.

2.1 Grain boundary energy

Since the framework of this PhD thesis is grain growth in polycrystals after recrystallization, we do not consider the energy per unit volume carried by dislocations, whose density is a driving force for recrystallization phenomena. Hence, we mainly focus on the grain boundary energy, which leads to the main driving force during grain growth. In this section, we present a description of GB energy, and models or numerical methods to compute it.

In figure 2.1 a grain boundary between two crystals is presented. This GB is characterized by: (i) the GB plane characterized by a normal vector $\underline{n}$ with two degrees of freedom (the normal unit vector is considered) and (ii) the misorientation between the two crystal lattices (the minimal rotation to make correspond the two lattices) characterized by three degrees of freedom: a unit vector for the rotation axis (2 degrees of freedom) and the rotation angle $\Delta\theta$ (1 degree of freedom). Therefore, GBs can be geometrically described using five parameters. Different and equally valid conventions (e.g., Euler angles, Rodrigues, quaternions) can be used to describe a three-dimensional GBs depending on the application. Since this PhD thesis deals with two-dimensional problems, the description of GBs is fairly simple, and reduces to only two degrees of freedom. Indeed, in 2D since the rotation axis is perpendicular to the plane, two angles are sufficient to describe the GB: (i) one angle for the GB plane and (ii) the misorientation angle.

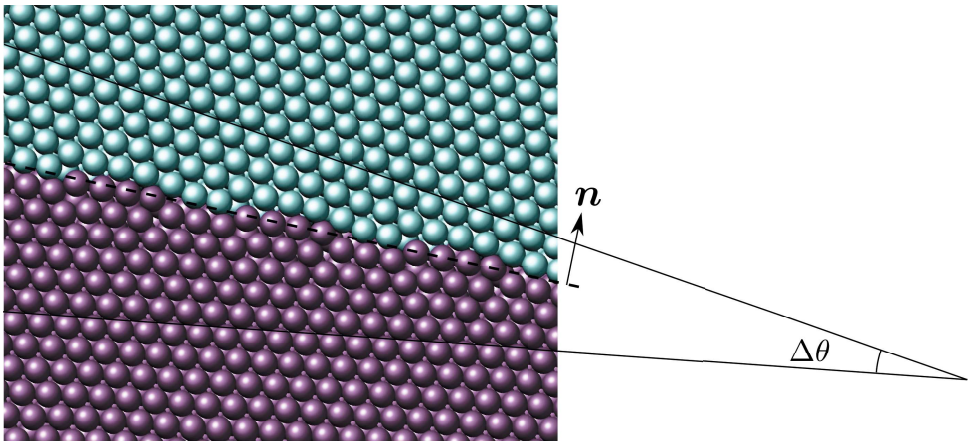

Figure 2.1: Grain boundary

It is clear from figure 2.1 that the energetic content of a bicrystal with different orientations is higher than the energetic content of a monocrystal. Indeed, the atomic arrangement at the GB is disrupted on a few atomic planes in order to accommodate the fact that the two disoriented lattices do not coincide. Thus, interatomic distances in this area are different from the equilibrium positions of the monocrystal (corresponding to the minimum of the interatomic potential) and therefore the bicrystal carries more energy. This energy excess is interpreted at the scale of the polycrystal as an energy per unit area carried by the GB. This GB energy is denoted by γ, and is essential to understand the driving force exerted in the GBs. Different methods were developed to measure this energy [32]. Not only does it depend on the atomic nature of the crystal but also on the temperature and the geometric nature of the GB (i.e., the GB plane and the crystal misorientation). For the sake of simplicity, some dependencies are often neglected, especially the dependency associated to the GB plane even though it is not always legitimate. Sometimes, the dependency of the GB energy γ on the misorientation between the two crystals is neglected, which is called isotropic energy. In this work, the effect of the misorientation on the GB energy is considered, which is usually refereed as anisotropic energy.

Numerical simulations of grain growth essentially rely on the knowledge of GB energy. That is why different methods enabling to compute numerical approximations of the GB energy have been developed. The main results of some of those approaches are presented in the following, and will be used in this work (see chapter 3).

2.1.1 Analytic model based on dislocation theory

The most ancient approach, but also the most used is the one proposed by Read&Shockley [1]. It consists of an analytical calculation based on a dislocation model of the grain boundary as shown in figure 2.2. The misorientation of the grain boundary is considered to be composed of two sets of equidistant edge dislocations ((010) and (100) planes edge dislocation) located on the grain boundary.

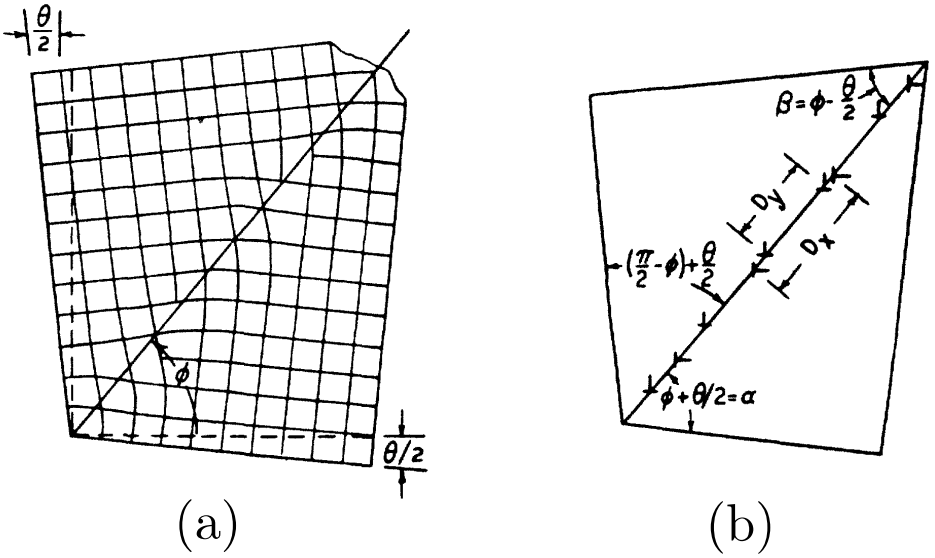

Figure 2.2: Dislocation model of a simple grain boundary [1]:(a) A symmetric tilt grain boundary between two crystals with a misorientation angle θ ($\Delta\theta$ in this document) and an inclination angle ϕ. (b) dislocation model.

The spacing between dislocations for the two sets is calculated from the dislocation densities that can be deduced from a simple geometrical calculation (see figure 2.2). D_x (respectively D_y) represents the spacing between two (010) (respectively (100)) dislocation planes:

$$\begin{cases} D_x = \dfrac{a}{\theta \cos\phi} \\ D_y = \dfrac{a}{\theta \sin\phi} \end{cases} \tag{2.1}$$

where a is the lattice constant, $\Delta\theta$ the misorientation angle and ϕ the inclination angle fixing the orientation of the GB plane.

The elasticity theory within the framework of isotropic solids is then used to compute the GB energy of the two arrays of dislocations. More specifically, the work done on the slip plane of each dislocation is calculated. This work is due to the stress system caused by each array of dislocations. The energy of the GB energy per unit area is simply the energy per slip plane times the density of slip planes summed for the two types of dislocations. The final form of this energy is as follows:

$$\gamma = E_0 \Delta\theta \, [A - \ln \Delta\theta] \tag{2.2}$$

where E_0 only depends on the inclination angle ϕ and the macroscopic elastic constants of the material.

$$E_0 = \frac{G\,a\,(\cos\phi + \sin\phi)}{A\pi(1-\nu)} \tag{2.3}$$

where G is the shear modulus and ν the Poisson's ratio and a the lattice constant.

A on the other hand is more difficult to grasp, since it depends on the energy of the atoms at the dislocation (energy of atomic misfit) and where Hooke's law is no longer valid.

A also depends on the inclination angle ϕ. However, for small values of ϕ, A can be approximated by 0.23.

2.1.2 Molecular dynamics

The range of validity of the Read & Shockley formula is limited to small misorientation angles and do not account for the energy cusps at certain misorientation angles. To overcome this difficulty, molecular dynamic computations have been proposed to compute GB energies as a function of the five parameters characterizing GBs. The principle of the method is to consider that atoms behave as point objects, whose motion is dictated by forces and the Newton's law (i.e., $F = m\,a$ with F the force, m the mass of the atom and a its acceleration). The forces are derived from an interatomic potential (or pair potential), which determines the potential energy as a function of the distance between a pair of atoms. Molecular dynamic computations basically consists in numerically solving the system composed of forces, masses according to the Newton's law to infer the atoms motion. It is clear then that molecular dynamics do not involve solving the Schrödinger equation or any aspects of quantum physics. The behavior of atoms is fully determined by the interatomic potential, which enables to upscale the fundamental behavior of matter. The main advantage is that relatively large simulations involving thousands of atoms can be performed although simulations of the Shrödinger equation are limited to a few tens.

Within the context of GB energy, molecular dynamic computations consist in directly minimizing the total energy composed of the interaction energy between atoms due to the interatomic potential. Usually the numerical scheme is based on the conjugate-gradient method as in the LAMMPS code [33] for instance. This minimization process gives only access to the equilibrium configuration and not to the motion of atoms by integrating the Newton's law with respect to time as for usual molecular dynamics computations. This methodology enables to save computation time and therefore to investigate a large number of different configurations. The GB energy is defined as the difference between the total energy after minimization of a bicrystal with a certain misorientation and the default stack energy of the corresponding monocrystal. The difficulty is that the total energy of the bicrystal is very similar to the default stack energy, which implies high accuracy for the subtraction to obtain reliable GB energy.

Among early works, Wolf [34–37] provided a systematic investigation of GB energy in fcc metals. Many other molecular dynamic computations have been carried out to determine GB energy (e.g., [38–40]). However, using molecular dynamics online during a simulation of grain growth would be computationally costly. Thus, some approaches attempt to establish simple models of GB energy based on multiscale strategies relying on molecular dynamic computations (e.g., [41]), whereas other approaches simply rely on interpolations of molecular dynamic computations (e.g., [42]). In this work such a strategy is adopted, molecular dynamic computations are performed and then interpolated as a function of misorientation.

There is a large variety of interatomic potentials. The simplest is the Lennard-Jones pair potential but it is common to use more sophisticated potentials such as the embedded-atom method (EAM) [43]. In this work, molecular dynamic computations to obtain GB energy have been derived for pure iron by using the interatomic potential proposed in [44], which presents the advantage to be stable at low temperature for fcc (although Fe presents

a bcc structure at low temperature). The approach is similar to [38, 39], using computation cell with periodic boundary conditions.

2.2 Curvature driven evolution

In this section, we detail the curvature driven evolution law of GBs. Such a law is widely used for grain growth models, and will be very useful in the scope of this work. In order to establish this classic law, we will consider a simple approach.

The idea is to consider a spherical grain of radius R in an homogenous matrix. The orientation of the two crystals (grain and matrix) creates a GB with a misorientation $\Delta\theta$. The GB energy per unit area is denoted by γ and the mobility of the grain boundary is denoted by m_{CD}. If the main mechanism of thois system if the migration of the GB, the total energetic state of the system can be can be written in the form of the GB energy per unit area γ multiplied by the sphere area $S = 4\pi R^2$:

$$\mathscr{E} = 4\pi R^2 \gamma \tag{2.4}$$

Thus, R is the only state variable of the system and the driving force F can be computed as follows:

$$F = \frac{\partial \mathscr{E}}{\partial R} = 8\pi R \gamma \tag{2.5}$$

The pressure P can also be defined by dividing the driving force by the GB area S:

$$P = \frac{F}{S} = \frac{2\pi\gamma}{R} \tag{2.6}$$

The grain growth is a viscous process that dissipates energy. In order to establish the evolution law, the dissipated power is postulated for a given virtual velocity v^* of the GB as follows:

$$\mathscr{D}(v^*) = \frac{S}{m_{CD}} (v^*)^2 \tag{2.7}$$

where m_{CD} is a coefficient representing the grain boundary mobility ($\mathrm{J}^{-1}.\mathrm{m}^4.\mathrm{s}^{-1}$). The dissipated power per unit area is $(v^*)^2/m_{CD}$. The real velocity of the grain boundary in this system is obtained by maximizing the dissipated power [45] under the constraint of the energetic balance equation, which reads:

$$\mathscr{D} + \dot{\mathscr{E}} = 0 \tag{2.8}$$

Thus, we need to solve:

$$-\dot{R} = v = \begin{cases} \underset{v^*}{\operatorname{argmax}} \left[\dfrac{S}{m_{CD}} (v^*)^2 \right] \\ \text{subjected to. } \dfrac{4\pi R^2}{m_{CD}} (v^*)^2 - 8\pi R\, v^* \gamma = 0 \end{cases} \tag{2.9}$$

The solution to this problem is elementary and reads:

$$v_{CD} = \frac{2\, m_{CD}\, \gamma}{R} \tag{2.10}$$

Where we defined $v = -\dot{R}$ the inward velocity corresponding to the reduction of the grain, hence the change of sign in the previous equations. The equation (2.10) can be interpreted as the local velocity of a portion of the GB, where R represents the local radius of curvature. In general, this equation is generalized [46, 47] in the case of double-curved GBs, that have in contrast with a sphere two principal radii of curvature R_I and R_{II}:

$$v_{CD} = m_{CD}\gamma\left(\frac{1}{R_I} + \frac{1}{R_{II}}\right) \tag{2.11}$$

Within the two-dimensional framework considered in this work, the principal radii of curvature of the GB are $R_I = R$ and $R_{II} = +\infty$. Thus the evolution law (2.11) reads:

$$v_{CD} = m_{CD}\gamma\kappa \tag{2.12}$$

where $\kappa = 1/R$ is the GB curvature. The evolution law (2.11) that depends on the GB curvature was experimentally validated on several occasions [48–51], and is used as the foundation of most grain growth numerical simulations. The curvature driven evolution law (2.11) is either used directly where the numerical simulation is developed as an approximation of (2.11), or it is used a posteriori to check the soundness of the model. In this work, the adopted approach does not relies on (2.11) directly. Indeed, there is no GB curvature in Voronoi-Laguerre tessellations that are the basis of the proposed mesoscopic model detailed in chapter 3.

2.3 Mobility

The main mechanism of grain growth comes from GB migration. GB mobility refers to the ability boundaries to migrate under the effect of a driving force. The mobility is denoted m_{CD} and arises in equation (2.11). The evolution rate is then very dependent on the mobility. This entity characterizes the power dissipated by a GB for every virtual velocity of the latter, as shown in equation (2.7). This dissipation represents the resistive part of the model, while the GB energy derived by the state variables represents the driving part.

At the scale of the polycrystal, the GB mobility mainly depends on temperature and on the misorientation. In fact, the mobility is very likely depends on numerous other parameters arising at lower scales. However, these dependencies are usually not taken into account in numerical simulations, because the detailed mechanisms responsible for grain mobility at the scale of dislocations or the atomic scale are not perfectly known. In this work, we limit ourselves to a simplified situation where the GB mobility only depends on temperature and misorientation, which is in good agreement with experimental data.

Grain growth is a thermally activated process, and experimental results show that the temperature dependance can be considered to follow an Arrhenius law :

$$m_{CD} = m_0 \exp\left(-\frac{Q}{\mathrm{R}T}\right) \tag{2.13}$$

where R is the ideal gas constant, Q is the activation energy that can depend on misorientation and m_0 a mobility independent on temperature but dependent on misorientation. The activation energy Q can be linked to atomic scale by considering the local thermally activated mechanisms that control GB migration. In the case of grain growth, the mobility

was successfully measured experimentally [50–53]. In figure 2.3 two examples extracted from the literature are presented, and highlight the link between the activation energy and the misorientation.

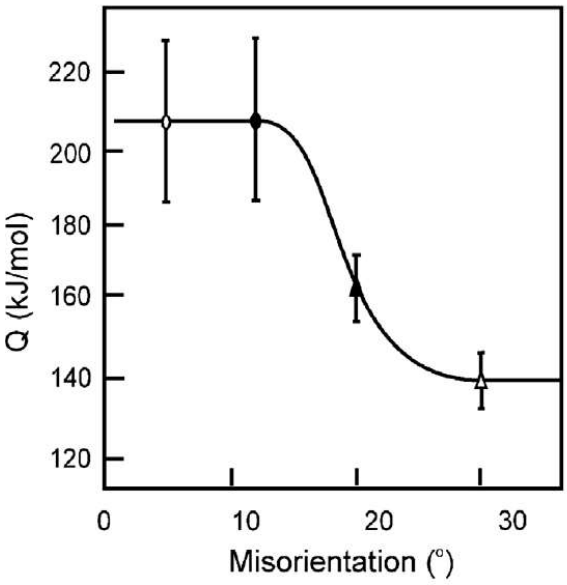

(a) Activation energy of sodium chloride as a function of misorientation after [53].

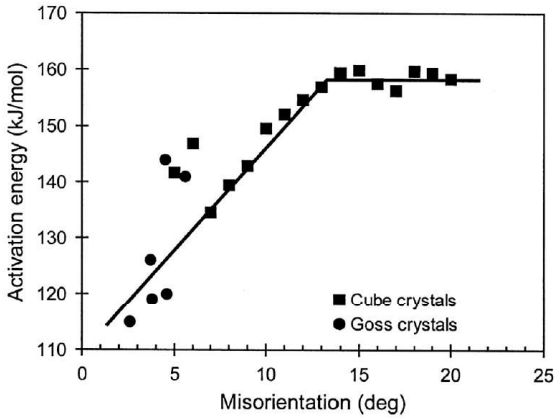

(b) The effect of misorientation on the activation energies for low angle boundary migration in Al-0.05%Si, measured from subgrain growth in single crystals after [54].

Figure 2.3: Experimental evidence that activation energy depends on misorientation.

It should be mentioned that other models with a temperature dependance in $1/T$ were proposed for instance in [55, 56] :

$$m_{CD} = \frac{C\,D_S\,b}{k_B\,T} \tag{2.14}$$

where C is a dimensionless constant, D_S the self-diffusion coefficient, b the Burger vector norm and k_B the Boltzmann constant. However, this model does not take into account the misorientation dependance.

In addition, experimental results show a clear dependance of the mobility on the misorientation. Historically, a distinction is made between low angle boundaries (<15°) and high angle boundaries (<15°). The mobility values are very different for these two classes of angles, as can be observed in figure 2.4 where experimental data are extracted from the literature.

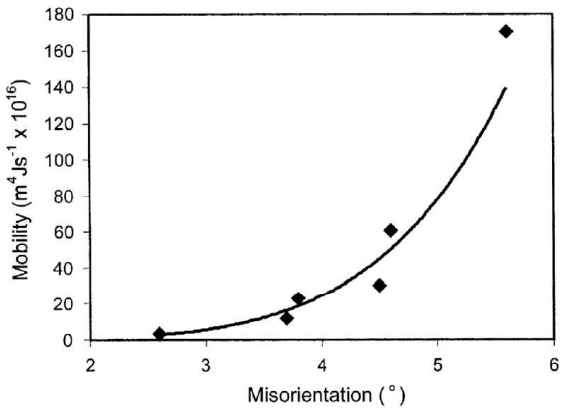

(a) The effect of misorientation on the mobility of low angle boundaries in Al-0.05%Si at 300 °C, measured from subgrain growth in single crystals, after [57].

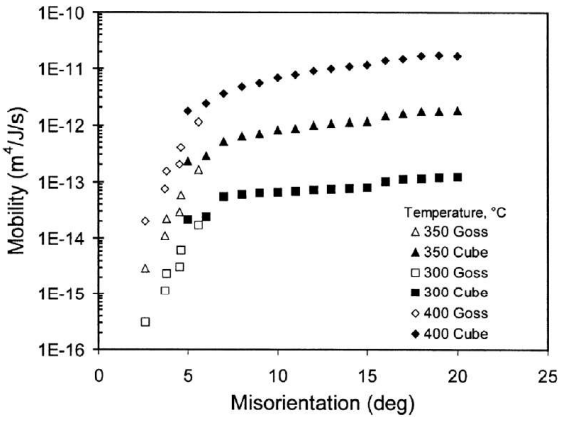

(b) The effect of misorientation and temperature on boundary mobility in Al-0.05%Si as a function of misorientation, measured from subgrain growth in crystals of Goss and Cube orientation, after [58].

Figure 2.4: Experimental measurements of mobility as a function of misorientation.

2.3.1 Very low angle boundaries

The detailed mechanisms leading to these results are not fully understood as explained in [2]. However, some models are proposed to compute the mobility in the case of low angle boundaries. Modeling mobility in the case of low angle boundaries mainly relies on dislocation dynamics, and especially the fact that the motion of GBs implies the motion of climb edge dislocations [2].

For very low angle boundaries, where $\Delta\theta < 1°$, dislocations involved at the GB are assumed to be independent of each other that is to say that they do not interact. It is therefore legitimate to consider that the motion of the GB is fully controlled by the mechanisms governing dislocation dynamics. In this limiting case, by writing the force per unit length applied to a curved dislocation, and by calculating the climb velocity of the latter, it is shown in [2] that the mobility is proportional to the inverse of the misorientation angle (2.15):

$$m_{CD} \propto \frac{1}{\Delta\theta} \tag{2.15}$$

Thus, when $\Delta\theta \to 0$, $m_{CD} \to +\infty$. Hence, according to (2.7) the dissipated power $\mathscr{D} \to 0$, which corresponds to the intuitive idea that the lower a bicrystal misorientation is (i.e., close to a monocrystal) and the lower the dissipation cost (i.e., resistance to GB motion) is.

A similar result was obtained within the framework of crystal plasticity [59, 60]. In [59], the dissipated power associated to the motion of a GB was estimated analytically for a simple configuration, nammely: two-dimensional ideal bicrystal with a hexagonal atomic structure. There are three plastic slips in hexagonal structures, and it is assumed that GB motion is associated to the activation of plastic slips so that the crystal arrangement of one crystal is transformed into the crystal arrangement of the second crystal. The flow rule is assumed to follow a Schmid's law. The link between the slip rates and the velocity of the GB is given by:

$$\mathrm{grad}\,\underline{v}^* = \sum_{n}^{-1,0,1} \dot{u}_n(\theta)\underline{s}_n(\theta) \bigotimes [-\underline{\underline{e}} \cdot \underline{s}_n(\theta)] - \dot{\theta}\underline{\underline{e}} \tag{2.16}$$

where $\underline{v}^*$ is the local virtual velocity of the GB, $\dot{u}_n$ the slip rates associated with the crystallographic slip directions $\underline{s}_n$, θ is the crystal orientation field and $\underline{\underline{e}}$ the permutation tensor. The dissipated power per unit area associated to any combination of slip rates reads:

$$D_m(\dot{u}_n(\theta),\dot{\theta}) = \tau_c \int_{s-\delta}^{s+\delta} \sum_{n}^{-1,0,1} |\dot{u}_n(\theta(x))| dx \tag{2.17}$$

where τ_c (MPa) is the critical shear stress, s the position of the GB and δ the half thickness of the GB where plastic slips are activated to transform one crystal arrangement into the other. This dissipation is calculated over the GB and for all the slip directions. The right combination of slip rates is determined by minimizing the dissipation (2.17) over the set of slip rates, and by using (2.16). Indeed, since crystal plasticity is a rate independent process, slip rates may be obtained by minimizing the total energy (stored elastic energy and dissipated energy). The considered problem being purely dissipative (there is no variation of stored energy) it is sufficient to minimize the dissipated power. The obtained dissipation, which is characteristic of the bicrystal, can be reduced to:

$$D(\Delta\theta, v^*) = \tau_c X(\Delta\theta) \left| v^* \right| \tag{2.18}$$

where $\Delta\theta$ is the misorientation angle and X is the following function:

$$X(\Delta\theta) = \frac{6}{\pi}\left(\frac{\pi}{3} + 2\sqrt{3}\ln\left(\frac{\sqrt{3}}{2}\right)\right)\min\left\{\Delta\theta, \frac{\pi}{3} - \Delta\theta\right\} \tag{2.19}$$

Since grain growth is viscous, the analytic computation proposed in [59, 60] can be simply adapted for crystal visco-plasticity by considering that the critical shear stress τ_c linearly depends on $\left|v^*_{ij}\right|$, which reads:

$$\tau_c = \frac{1}{m(T)} \left| v^*_{ij} \right| \tag{2.20}$$

where $m(T)$ is homogenous to a grain mobility ($\mathrm{m}^4.\mathrm{J}^{-1}.\mathrm{s}^{-1}$) that can be related to the curvature driven mobility m_{CD}. The mobility $m(T)$ is calibrated so that the shrinkage of an hexagonal grain evolves at the same speed as the shrinkage of a circular grain according to the curvature driven evolution law. More precisely, it is shown in A.2 that:

$$m_{CD}(T,\Delta\theta) = \frac{m(T)}{X(\Delta\theta)} \tag{2.21}$$

Thus, as for the analysis with independent dislocations the mobility depends for very low angle boundaries on misorientation in $1/\Delta\theta$. It should be mentioned that crystal plasticity is a valid mechanism to explain GB mobility only for very low angle boundaries.

2.3.2 High angle boundaries

For high angle boundaries ($\Delta\theta > 15°$), dislocations are closer to each other and may interact. The mechanisms associated to mobility can no longer be attributed to the motion of dislocations. In that case, atomic jumps over the grain boundary are more suited to explain the GB motion as explained in [2]. For high angle boundaries, experiments provide evidences that the mobility is independent on the misorientation angle as shown in figure 2.4b.

2.3.3 Low angle boundaries

For low angle boundaries ($1° < \Delta\theta < 15°$), the mechanism that is usually considered is similar to the diffusion of atoms across a membrane with a given thickness [2], leading to a mobility of the form:

$$m_{CD} \propto \Delta\theta \tag{2.22}$$

which is approximately verified in figures 2.4a and 2.4b.

By associating considerations for low angle boundaries ($1° < \Delta\theta < 15°$) and high angle boundaries ($\Delta\theta > 15°$), a mobility function depending on the misorientation angle is proposed in [61, 62]:

$$m_{CD}(T, \Delta\theta) = m_{\max}(T)\left(1 - \exp\left[-K\left(\frac{\Delta\theta}{\Delta\theta_1}\right)^p\right]\right) \tag{2.23}$$

where a sigmoid function is introduced in (2.23) to make a smooth transition from one regime to the other.

However, this function tends to 0 when $\Delta\theta \to 0$. Thus, equation (2.7) leads to a diverging dissipated power $\mathscr{D} \to +\infty$, which is inconsistent with the analysis presented in section 2.3.1 for very low angle boundaries. In order to overcome this issue, we propose in section 3.1 an improved version of the mobility function (2.23), which takes into account considerations for very low angle boundaries $\Delta\theta < 1°$ (i.e., a mobility function that leads to a zero dissipated power when $\Delta\theta \to 0$).

Many other factors affect mobility. However, such factors will not be discussed in this dissertation. Indeed, a modeling choice is made throughout this work to neglect the other aspects besides misorientation and temperature. The reader can be referred to the chapter 5 of the book [2] for a thorough literature review of the different factors affecting the grain boundary mobility.

2.4 Numerical approaches at mesoscopic scale

In this section, the main approaches underlying numerical simulations of grain growth are reviewed, with brief discussion on their advantages and limitations. The contribution of the present work is positioned within the scope of this vast and rich field of study. Different literature reviews are available on this subject [2, 25].

2.4.1 Mean field approaches

In the context of grain growth, mean field approaches consist in using idealized structures usually with spherical grains representing different grain families in the polycrystalline structure sharing the same properties such as size and crystal orientation. However, in real polycrystalline structures, fundamental properties such as misorientation depend not only on the intrinsic characteristics of the grains but also on their connection, that is to say their relative positions. This aspect is neglected in mean field approaches, which are based on simplified relationships between the different grain families, as the detailed grain structure is not considered.

The early works [46, 47] deriving a growth law for the mean grain radius $\langle R \rangle$ can be considered as one of the first mean field approaches. This model relies on the curvature

driven evolution law (2.10). In addition, the GB energy per unit area γ is assumed to be a constant (i.e., independent on misorientation and GB plane), which simplifies the analysis as the connectivity between grains is not taken into account. The radius R of each grain family is proportional to the mean radius of the entire structure $\langle R \rangle$. Thus, by using (2.10) one obtains:

$$\frac{\mathrm{d}\langle R \rangle}{\mathrm{d}t} = \frac{C_0 \gamma}{\langle R \rangle} \tag{2.24}$$

where C_0 is a constant. Hence by integrating one obtains:

$$\langle R \rangle^2 = C_1 + 2 C_0 \gamma t \tag{2.25}$$

where $C_1 = \langle R(t=0) \rangle^2$, which is often written as follows:

$$\langle R \rangle \propto C\, t^{\frac{1}{n}} \tag{2.26}$$

Where C is a constant, and $n = 2$ is called the growth exponent. In practice experiments give evidences that the growth exponent may lie in the following interval $[2,4]$ [63].

An other famous model called the von Neumann-Mullins (vNM) law [64, 65] relates the number of sides and the area change rate of each grain family. The classical vNM law is formulated within a fully isotropic framework (i.e., isotropic GB energy and isotropic mobility), and relies on the curvature driven evolution law (2.12) and the assumption that angles at triple junctions are 120°. The vNM reads:

$$\frac{\mathrm{d}}{\mathrm{d}t} S_n = \frac{\pi m^*}{3}(n-6) \tag{2.27}$$

where n is the number of sides of the grain family, $\mathrm{d}S_n/\mathrm{d}t$ is the area change rate of n sided grains, and $m^* = \gamma\, m_{CD}$ ($\mathrm{m}^2.\mathrm{s}^{-1}$) is the constant reduced mobility. Since $S_n \propto R_n^2$ where R_n is the radius of the n sided grain family, (2.27) reads:

$$\frac{\mathrm{d}}{\mathrm{d}t} R_n = \frac{D}{R_n}(n-6) \tag{2.28}$$

where D is a constant. In addition, an extended vNM law (3.55) has also been proposed for anisotropic grain growth and tested with a mesoscopic stochastic Monte-Carlo simulations [66].

$$\frac{\mathrm{d}}{\mathrm{d}t} \langle S_n \rangle = \langle m_n^* \rangle \left(\pi - \langle \beta_n \rangle\right) \left(n - \frac{2\pi}{\pi - \langle \beta_n \rangle}\right) \tag{2.29}$$

where $\langle m_n^* \rangle$ is the average reduced mobility, $\langle \beta_n \rangle$ is the average triple junction angle, and where averages are taken over the family of the n sided grains.

Among the early mean field theories, the statistical approaches are well known [67]. Considering a grain family of radius R the following relationship is found in [67]:

$$\frac{\mathrm{d}R}{\mathrm{d}t} = m\gamma \left(\frac{1}{\langle R \rangle} - \frac{1}{R}\right) \tag{2.30}$$

where m and γ are respectively the constant mobility and GB energy per unit area of the considered grain family, and $\langle R \rangle$ is the overall average grain radius, which is estimated from (2.24). This relationship (2.30) has been obtained within the framework of a more general

mean field approach in [61, 68]. The derivation of (2.30) is based on energetic considerations during the growth of the grain family of radius R. Consider the GB boundary energy $\mathscr{E}_{GB} = S\gamma$, where $S = 4\pi R^2$ is the area of the spherical GB. In addition, when a grain family of radius R grows, some GBs in the rest of the structure are annihilated and the energy decreases. The energy carried by the GBs in the rest of the structure is modeled by an energy per unit volume E_V. Thus, the energy carried by the GBs in the rest of the structure reads $\mathscr{E}_{\text{bulk}} = (V_0 - V)\, E_V$ where V_0 is the volume of the rest of the structure and $V = 4/3\pi R^3$ is the volume of the sphere of radius R. Thus, the total energy reads:

$$\mathscr{E} = 4\pi R^2 \alpha\gamma - \left(V_0 - \frac{4}{3}\pi R^3\right)\beta E_V \tag{2.31}$$

where coefficients α, β are introduced to take into account the fact that an idealized structure is considered, and therefore approximate formulas are obtained. The driving force F reads:

$$F = \frac{\partial \mathscr{E}}{\partial R} = 8\pi R\alpha\gamma - 4\pi R^2 \beta E_V \tag{2.32}$$

The pressure P reads (where $S = 4\pi R^2$):

$$P = \frac{F}{S} = \frac{2\alpha\gamma}{R} - \beta E_V \tag{2.33}$$

Since E_V represents the energy per unit volume carried by the GBs in the rest of the structure, one can relate E_V and the average GB energy $\langle\gamma\rangle$ and the average grain radius $\langle R\rangle$:

$$E_V = \frac{3\langle\gamma\rangle}{2\langle R\rangle} \tag{2.34}$$

Hence:

$$\frac{\mathrm{d}R}{\mathrm{d}t} = -mP = m\left(\beta\frac{3\langle\gamma\rangle}{2\langle R\rangle} - \frac{2\alpha\gamma}{R}\right) \tag{2.35}$$

The classical relationship derived in [67] is obtained with $\beta = 2/3$ and $\alpha = 1/2$ and a constant GB energy (i.e., $\langle\gamma\rangle = \gamma$.

By solving the coupled system (2.30) and (2.24) Hillert [67] found a steady state statistical distribution of $R/\langle R\rangle$:

$$p\left(\frac{R}{\langle R\rangle}\right) = 2^3 \exp(2)\frac{R}{\langle R\rangle}\left(2 - \frac{R}{\langle R\rangle}\right)^{-4} \exp\left(-\frac{4}{2 - \frac{R}{\langle R\rangle}}\right) \tag{2.36}$$

Other well known distributions have been obtained in [69, 70], for instance the Rayleigh distribution reads:

$$p\left(\frac{R}{\langle R\rangle}\right) = \frac{\pi}{2}\frac{R}{\langle R\rangle}\exp\left(-\frac{\pi}{4}\left(\frac{R}{\langle R\rangle}\right)^2\right) \tag{2.37}$$

Of course more advanced mean field approaches have been developed to model grain growth and static or dynamic recrystallization. In particular semi-topological approaches have been developed [71]. In addition mean field approaches are usually used to reproduce full field computations (e.g., using level set method as detailed in section 2.4.5) to save computation time for industrial processes such as rolling process for instance. A commercial code DIGIMU [72] has been developed, and can perform both full field computations and calibrated mean field estimations. Of course, since mean field approaches are

mostly based on mean grain size or grain size statistics, the information that is upscaled at the macroscopic scale is not particularly rich. One of the main ambition of this PhD thesis is to present an upscaling method, which enables (in the limited context of two-dimensional grain growth) to deal with additional grain statistics at the macroscopic scale, such as mean and standard deviation of misorientations or the GB lengths per unit area.

2.4.2 Vertex models

The vertex method consists in considering a network of grains, often constructed as a Voronoi network. The idea is to control the motion of the boundaries by computing an evolution of the vertices positions. The code should also take into account the limit cases where two vertices are driven to meet or when a grain tends to shrink and disappears.

Two main vertex model can be identified depending on the dynamics used to govern the motion: (i) boundary dynamics models and (ii) vertex dynamics models. On the one hand, boundary dynamics models are based on equations governing the motion of the grain boundaries, usually based on the curvature driven evolution law (2.12). These models necessitate to introduce a local GB curvature that does not explicitly exists in a vertex network, thus a GB curvature is estimated by comparing positions of neighboring vertices. Positions of the triple junctions (i.e., vertices) can therefore be updated so that the curvature driven evolution law is satisfied. The aim of this approach is to mimic physical mechanisms of boundary migration described in section 2.3. On the other hand, vertex dynamics models rely on evolution laws applied to the vertices positions, leading to a much cost-friendly model. The difficulty of such approaches is to determine the right evolution law to affect to vertices so that the behavior of the system is satisfying. Indeed, the motion of each vertex is dependent on both position and motion of the neighboring vertices, which makes fairly complicated the search for a suitable evolution law. In [27], three-dimensional vertex model is adopted and based on the minimization of the grain boundary energy. In [28], a vertex model based on Read&Shockley GB energy is implemented and compared phase-field simulation results.

2.4.3 Tessellation updating methods

In this PhD thesis, a mesoscopic model of grain growth is proposed and relies on orientated tessellation updating method (OTUM), which consists in modeling the evolution of the polycrystalline structures as a succession of orientated tessellations (OT) (Voronoi-Laguerre tessellations equipped with an crystal orientation field). This approach presents the advantage to rely on very efficient algorithm to produce Voronoi-Laguerre tessellations in 2D or 3D such as NEPER [29]. The details of the methods are exposed in chapter 3. As already mentioned, to the best of our knowledge this idea of updating Voronoi-Laguerre tessellation parameters to model grain growth has been proposed for the first times in [30, 31]. A Voronoi-Laguerre tessellation is composed of seeds and weights. Seeds are assumed not to evolve and the weights (where $1 \leq j \leq N$ with N the number of grains) are determined by the following evolution law in [31]:

$$\dot{w}_j = 4\, m\, \langle R \rangle\, P_j \tag{2.38}$$

where w_j is the weight of grain j, m is the mobility, $\langle R \rangle$ the average grain size and P_j the pressure applied to grain j. Various models for P_j are postulated in [31] such as:

$$P_j = \begin{cases} P_j = -\dfrac{1}{R_j} \\ P_j = -\dfrac{S_j}{V_j} \end{cases} \tag{2.39}$$

where R_j, S_j, V_j are respectively the radius, area and volume of the grain j. However, the evolution law (2.38) is questionable. Indeed, it is postulated to directly mimic the curvature driven evolution law despite the fact that GBs have no curvature in a Voronoi-Laguerre tessellation. More importantly, the weights are controlled independently, however the modification of a single weight affects several GBs according to the Voronoi-Laguerre definition, which plays the role of a geometrical constraint on possible GB motions. Thus, the curvature driven evolution law is not appropriate within the framework of OTUM, as it would necessitate to control GBs independently. In contrast, we present in chapter 3 a tensorial evolution law, which enables to update all the weights at the same time accounting for the relationship between the grains as imposed by the Voronoi-Laguerre tessellation definition.

2.4.4 Monte Carlo simulations

The Monte Carlo method is widely used to simulate grain growth in both two and three dimensions [6–10], also called the Potts models or Q-state Ising models. The method consists in discretizing the polycrystalline structure using pixels (in 2D) or voxels (in 3D). The mesoscopic structure is then represented by a discrete grid of blocks. To each block are assigned different attributes like the crystal orientation. A grain is then an assembly of blocks with the same orientation. To the blocks of the same grain are also attributed the same ID number (see figure 2.5). A grain boundary is then defined implicitly between neighboring blocks with different IDs (i.e., jumps in the ID field).

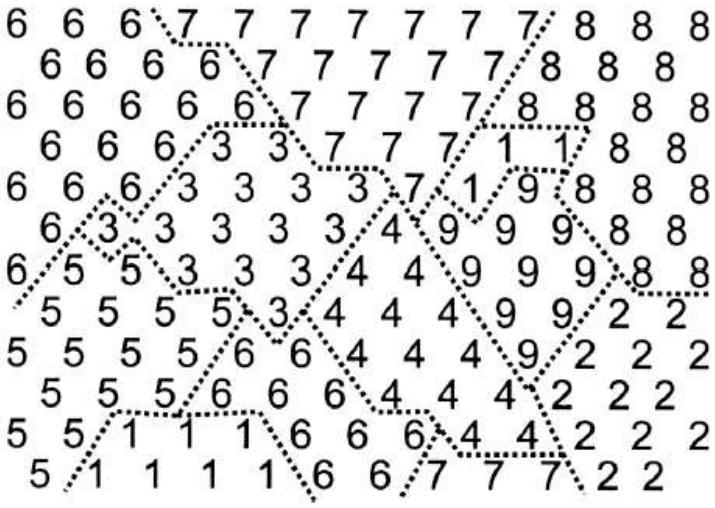

Figure 2.5: The basis of the Monte Carlo simulation method [2].

The main idea of Monte Carlo simulations is make random attempts to replace the ID of a voxel at a grain boundary by the ID of the neighboring grain as shown in figure 2.6. This change is accepted according to a probability that depends on the energy change due to the ID replacement. Of course this probability is designed so that the global behavior of the system is satisfying with respect to the curvature driven evolution law. Thus, the evolution of the system is governed by two key quantities: (i) the total energy of the system $\mathscr{E}$ and (ii) the transition probability matrix $\underline{\underline{P}}$ composed of the probability P_{ij} of accepting the ID change of the block i into the ID of the block j. The total energy of the system is basically the sum of GB energies, as well as bulk energies. The transition probability P_{ij} reads:

$$P_{ij} = \begin{cases} \dfrac{\gamma_{ij}}{\gamma_{\max}} \dfrac{m_{ij}}{m_{\max}} & \Delta\mathscr{E} \leq 0 \\ \dfrac{\gamma_{ij}}{\gamma_{\max}} \dfrac{m_{ij}}{m_{\max}} \exp\left(-\dfrac{\Delta\mathscr{E}}{\gamma_{\max} kT}\right) & \Delta\mathscr{E} > 0 \end{cases} \tag{2.40}$$

where γ_{ij} and m_{ij} are respectively the energy and the mobility of the grain boundary between two blocks i and j (if the blocks i and j belong to the same grain, $\gamma_{ij} = 0$), $\gamma_{\max}, m_{\max}$ are the maximal values of γ_{ij}, m_{ij}, and $\Delta\mathscr{E}$ corresponds to the change of energy due to the transition.

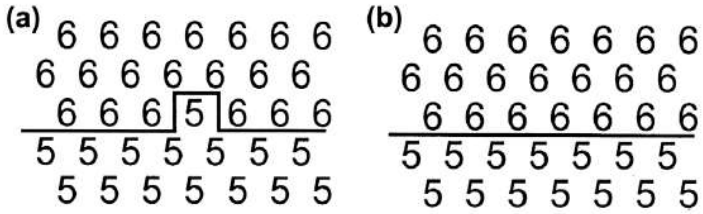

Figure 2.6: Grain boundary migration in the Monte Carlo model [2].

Thus, in practice, blocks are selected at random and the ID change is attempted. The new energy state is computed and compared to energy at the previous time step (i.e., $\Delta\mathscr{E}$ is computed). This change is accepted according to the transition probability P_{ij} defined in (2.40). Is clear that ID changes, which lead to a decrease of the total energy (i.e., $\Delta\mathscr{E} < 0$) are much more likely to be accepted than changes which lead to an increase of the energy (i.e., $\Delta\mathscr{E} > 0$). The probability of accepting the ID change decreases exponentially with $\Delta\mathscr{E} > 0$, which indicates that the system statistically decrease in energy. In addition, for ID changes such as $\Delta\mathscr{E} < 0$, the probability (2.40) tends to favor the changes corresponding to the highest GB energy and mobility, which captures intuitively grain growth thermodynamics.

The kinetics of the Potts model proves to be conform to the curvature driven grain migration [2]. Potts model is quite easy to understand and to code. However, the computational cost can be very high for large mesoscopic structures.

2.4.5 Level set methods

The level set method is a general implicit description of boundaries by means of fields defined on the entire body instead of a local description of the surface. Usually a level

set function is defined as the signed distance between the surface to be described and a point of the space, which implies that the surface corresponds to the points where the level set function vanishes. This technique is suitable to numerically describe complex surface topology with fast algorithms to update the level set function (i.e., a field defined in the entire body), which lead to numerous applications (e.g., X-FEM within the context of fracture mechanics). Level set functions were first used for grain growth in [73] and adopted ever since [13–15, 74, 75]. The basic idea is to consider a continuous scalar field (i.e., the level set function) defined on the domain of the mesoscopic structure. The grain boundary location is given as the zero level set. The migration of the grain boundary can then be captured through the evolution of the level set function via the transport equation:

$$\frac{\partial \Phi}{\partial t} + \underline{v} \cdot \nabla \Phi = 0 \tag{2.41}$$

where Φ s the level set function and $\underline{v}$ the velocity field.

For a polycrystal, a several level set functions are defined to account for all the grain boundaries. The model relies the choice of the velocity field expression and the level set function. In [15], the grain boundary velocity is given by:

$$\underline{v} = m(\nabla \gamma \cdot \underline{n} - \gamma \kappa)\underline{n} \tag{2.42}$$

where m is the grain boundary mobility, γ the GB energy, κ the mean curvature of the grain boundary and $\underline{n}$ the outside normal vector to the GB. It is common to consider the level set functions as the distances from the grain boundary, where the function is positive inside the grain, negative outside the grain and zero on the grain boundary. In that case, the curvature κ and the normal $\underline{n}$ can be easily deduced from the level set function, leading to the following transport equation (see [15]):

$$\frac{\partial \Phi}{\partial t} + m \nabla \gamma \cdot \nabla \Phi - \gamma \Delta \Phi = 0 \tag{2.43}$$

Finite elements can be used in order to solve the transport equation (2.43).

2.4.6 Phase field approach

The phase-field method is also an important and versatile technique for simulating the evolution of polycrystalline structures at the mesoscopic scale [3, 16–21, 76, 77]. Phase field methods were first used for grain growth in [78]. The main idea is to represent each phase (or crystal orientation in this context) by a scalar field continuous in space and time. Different modeling approaches are possible, the most used is the diffuse-interface description where the phase field variables correspond to their values inside the grains, and vary gradually in a narrow region between two neighboring grains representing the GB. In this case, the evolution of the mesoscopic structure is implicitly given by the evolution in time of the phase field variables, as shown in figure 2.7.

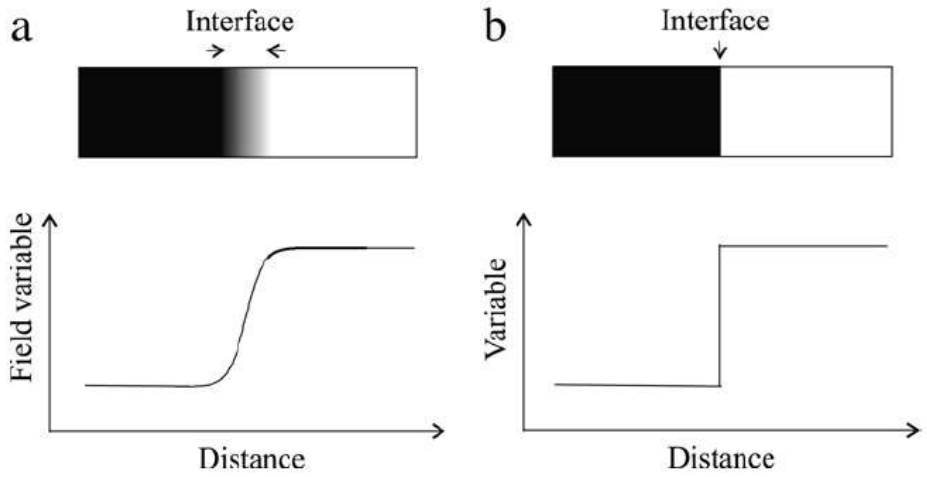

Figure 2.7: Schematic representation of an interface in a diffuse-interface phase field model [3].

The time evolution of the phase field variables is described by a set of partial differential equations (that can be solved numerically by finite element techniques or fast Fourier transform techniques if periodic configurations are studied). The main advantage of phase field methods is the possibility to consider different physical aspects of the mesostructure evolution by considering different energetic contributions. Indeed, the method is based on general thermodynamic and kinetic principles, which requires to account for the energetic state of the studied system.

The first step is the choice of the phase field variables depending on the modeled physical phenomenon (crystal orientation is typically used for grain growth). The second step consists in defining a free energy function that depends on the phase field variable. Indeed, the evolution is determined by reducing the free energy of the system. Different energy contributions can be considered in (2.44).

$$\mathscr{F} = \mathscr{F}_{int} + \mathscr{F}_{bulk} + \mathscr{F}_{el} \tag{2.44}$$

where $\mathscr{F}_{int}$ is the interface energy (e.g. grain boundary energy), $\mathscr{F}_{bulk}$ the bulk energy (e.g. energy associated to the dislocation density), and $\mathscr{F}_{el}$ the elastic strain energy. Finally, the principle of virtual power can be applied within a thermodynamic framework to derive the evolution equations of the phase field variables.

For instance, this approach has been developed in [19, 20] with two separate phase fields: the crystal orientation θ and the crystallinity η (describing the local crystalline order in the transition zone between two grains). More recently a unified formulation of grain boundary motion phase field model and mechanics has been proposed in [76, 77] within the framework of Cosserat theory to account for non-local effects such as the rotation induced by crystal plasticity.

2.4.7 Molecular dynamics

As already mentioned in section 2.1.2, molecular dynamics consists in solving the dynamic Newton's system, whose applied forces are derived from an interatomic potential. This interatomic potential determines in a simplified way all the properties of the atoms and es-

pecially their interactions. Since rather large simulations can be performed and considering the fact that the atomic scale is well suited to simulate GB motion, molecular dynamics is a very powerful tool to understand detailed mechanisms associated to the mobility of GB [22–24, 79]. For instance the reduction of a channel in a matrix has been simulated in [22] confirming that the GB velocity is associated with the curvature (i.e., no motion for the flat part of the channel). However, the main difficulty with such methods is to adequately chose the interatomic potential as a large variety of potentials have been established for various chemical species. Indeed, the interatomic potential fully determine the behavior of the simulation, and none of them fully characterize the atomic behavior (atomic potentials being oversimplified with respect to fundamental laws of quantum physics). Thus, one should consider an interatomic potential that is suited for solving the considered problem, knowing that the same potential may not be suited for a different problem. An other drawback of such a detailed method is of course the computation time, which strongly limit the applicability of molecular dynamics to significantly large problems.

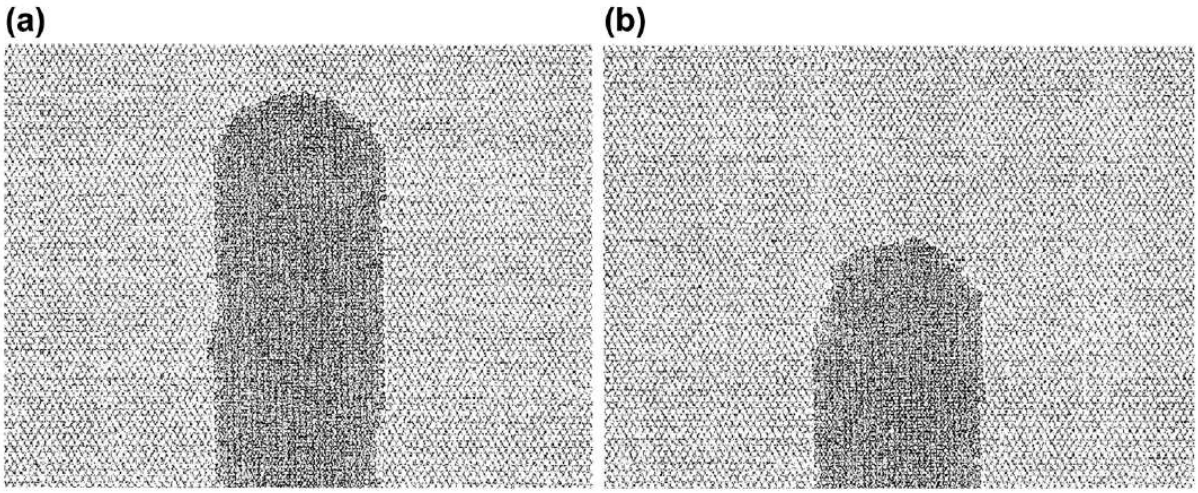

Figure 2.8: Simulation of shrinkage of a channel.

Chapter 3

Fast mesoscopic model based on dissipation

« A great deal of my work is just playing with equations and seeing what they give. »

Paul A. M. Dirac

Contents

3.1 Introduction

This chapter is adapted from a paper published in *Acta Materialia* [80], which was initiated by a paper published in *Mechanics & Industry* [81]. In this chapter the mesoscopic model of grain growth is detailed within the framework of the general energetic upscaling method proposed in this thesis. General principles of Orientated Tessellation Updating Method (OTUM) are presented in section 3.2. In section 3.3 we detail the procedure enabling to generate different Representative Volume Elements (RVE) to probe the space of possible Orientated Tessellations (OT). Mass conservation issues and the minimum number of grains that should be considered for the RVEs is discussed in section 3.4. Mechanisms at the microscopic scale are broached in section 3.5. In particular molecular dynamics computations are performed to obtain the GB energy, and the mobility is derived as function of misorientation. The mesoscopic evolution law, which constitutes the core equation of the model is derived in section 3.6. Results and discussion are provided in section 3.7. Classical models (Hillert distirbution [67, 82] and von Neumann-Mullins law [64, 66]) are compared to the model to validate basic grain statistics. A comparison with an experimental study conducted on pure iron [83] is also presented and good agreement is observed. More detailed statistics are also analyzed to determine meaningful information to be considered at the macroscopic scale. Conclusive remarks are given in section 3.8.

3.2 Orientated Tessellation Updating Method

In this section mathematical definition of the OT is provided as well as general principles of the OTUM. A Voronoi-Laguerre tessellation is defined by N *seeds* whose dimensionless Cartesian coordinates are denoted by $(x_j, y_j) \in [0,1]^2$ and N dimensionless *weights* denoted by $w_j \in \mathbb{R}_+$ (where $1 \leq j \leq N$). The tessellation is completely determined by the parameter vectors $\underline{x} = (x_1, \cdots, x_N)$, $\underline{y} = (y_1, \cdots, y_N)$, $\underline{w} = (w_1, \cdots, w_N)$. Each cell (or grain) denoted by C_j (where $1 \leq j \leq N$) is defined as follows:

$$C_j = \left\{ \begin{pmatrix} x \\ y \end{pmatrix} \in \mathbb{R}^2,\ \forall k \in \{1, \cdots, N\},\ \left\| \begin{matrix} x - x_j \\ y - y_j \end{matrix} \right\|^2 - w_j \leq \left\| \begin{matrix} x - x_k \\ y - y_k \end{matrix} \right\|^2 - w_k \right\} \tag{3.1}$$

It is clear from the definition (3.1) that weights are defined up to a constant. Thus, the following constraint is added to obtain a univocal definition:

$$\sum_{j=1}^{N} w_j = 1 \tag{3.2}$$

Thus, weights $\underline{w}$ lie in an affine hyperplane of dimension $N-1$ and denoted by $P_a^{(N-1)}$, whose support is the hyperplane denoted by $P^{(N-1)}$ and:

$$\begin{cases} P^{(N-1)} = \left\{ \underline{w} \in \mathbb{R}_+^N,\ \underline{w}.\underline{1} = 0 \right\} \\ P_a^{(N-1)} = \left\{ \underline{w} \in \mathbb{R}_+^N,\ \underline{w}.\underline{1} = 1 \right\} = P^{(N-1)} + \underline{w}_0 \end{cases} \tag{3.3}$$

where $\underline{1} = (1, \cdots, 1) \in \mathbb{R}^N$ and $\underline{w}_0 \in \mathbb{R}_+^N$ verifies $\underline{w}_0.\underline{1} = 1$. In addition, it should be noted that a cell C_j may be empty as shown in figure 3.1a. This property will be intensively used

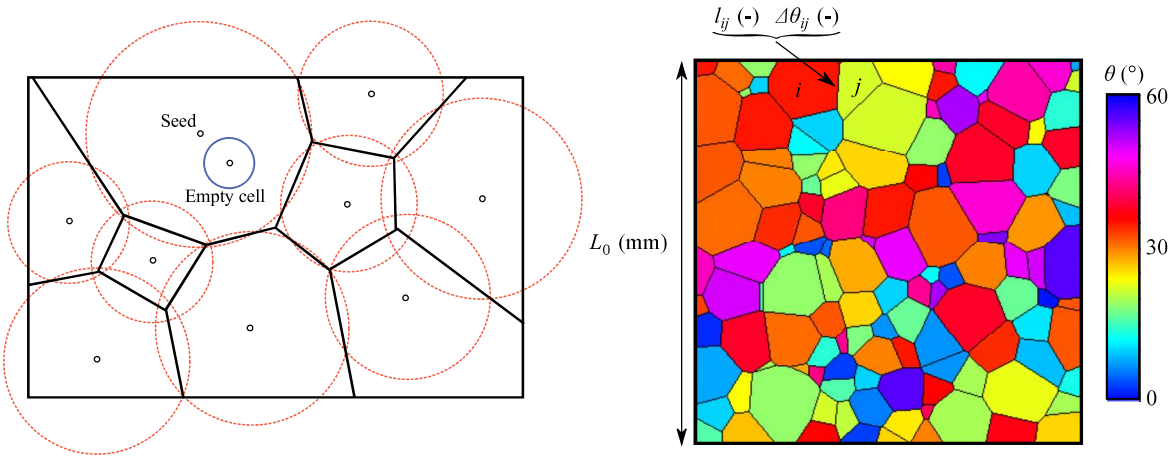

(a) Seeds and weights in Voronoi-Laguerre tessellation. Some cells can be empty.

(b) Notations and crystallographic orientations (0° and 60° are identical as crystals are plane hexagonal)

Figure 3.1: Orientated tessellation

as some grains should disappear during grain growth. In 2D, crystallographic orientations are defined as N additional *angles* denoted by θ_j (where $1 \leq j \leq N$). In this chapter, θ_j represent the $\langle 111 \rangle$ tilt angles. Thus, the OT tessellation definition necessitates the additional vector $\underline{\theta} = (\theta_1, \cdots, \theta_N)$. Since the crystal lattice is plane hexagonal $\theta_j \in [0, \pi/3]$ (where $1 \leq j \leq N$). Therefore, the parameter set $\mathscr{P}_{\text{OT}}$ defining OTs reads:

$$\mathscr{P}_{\text{OT}} = \left\{ \underline{\alpha} = (\underline{x}, \underline{y}, \underline{w}, \underline{\theta}) \in [0,1]^N \times [0,1]^N \times P_a^{(N-1)} \times \left[0, \frac{\pi}{3}\right]^N \right\} \tag{3.4}$$

Grain boundaries are indexed by pairs (i, j) where i and j denote two neighboring grains (where $1 \leq i \leq N$ and $1 \leq j \leq N$). The set of pairs of neighboring grains defining grain boundaries is denoted by I_{GB}:

$$I_{GB} = \left\{ (i,j) \in \{1, \cdots, N\}^2,\ j > i,\ C_i \cap C_j \neq \varnothing \right\} \tag{3.5}$$

The condition $j > i$ is meant to count each grain boundary only once. Since the parameters defining OTs are dimensionless, the physical size of the OT is given by L_0 representing the length of the box side in which the OT is contained, as shown in figure 3.1b. Moreover for any grain boundary $(i, j) \in I_{GB}$ (with i and j two neighboring grains) $l_{ij} \in [0, 1]$ denotes the dimensionless GB length and $\Delta\theta_{ij} = \left|\theta_j - \theta_i\right| \in [0, \pi/3]$ is the misorientation angle.

The general principle of the OTUM is to establish an evolution law directly on the parameter of the OT, that is to say that for $\underline{\alpha} \in \mathscr{P}_{\text{OT}}$:

$$\dot{\underline{\alpha}} = f(\underline{\alpha}) \tag{3.6}$$

For the sake of simplicity we assume that only weights $\underline{w}$ can evolve. In particular, $\underline{\theta}$ is fixed. This implies that we neglect crystallographic rotations (obtained by activation of plastic slips systems in the bulk), which only affects the smallest grains [24]. Thus, the general evolution law reads for $\underline{\alpha} = (\underline{x}, \underline{y}, \underline{w}, \underline{\theta}) \in \mathscr{P}_{\text{OT}}$:

$$\dot{\underline{w}} = f(\underline{\alpha}) \tag{3.7}$$

An explicit form of the evolution law (3.7) is derived in section 3.6.

3.3 Probabilistic procedure for orientation assignment

As mentioned in the introduction, the proposed energetic upscaling strategy necessitates to probe the space of possible OTs. Indeed, very different morphological and crystallographic textures may be observed [2] depending on fabrication and forming processes that impose specific temperature paths and deformation mechanisms.

The morphological texture is controlled by seeds $(\underline{x}, \underline{y})$ and weights $\underline{w}$, whereas the crystallographic texture is controlled by the orientations $\underline{\theta}$. Morphology (e.g., shape and size distributions) may be controlled by optimization techniques in the free software NEPER [29]. In addition, one can generate tessellations by choosing $\underline{x}, \underline{y}, \underline{w}$ randomly (with various probability density functions), which enables to produce a *database* of very different tessellations with respect to sphericity and size distributions.

Since GB energy significantly depends on misorientation, the boundary misorientation distribution (BMD) (i.e., misorientations between neighboring grains) is essential for predicting anisotropic grain growth. Misorientation angles are simply deduced from crystal orientations but cannot be directly prescribed as a control parameter of the OT. Moreover, one cannot probe the space of possible BMDs by assigning crystal orientations purely randomly. Indeed, misorientations not only depend on crystal orientations but also on the network connectivity formed by the grains. In other words, the way to assign an orientation to a grain should depend on the orientation of its neighbors. If crystal orientations are assigned randomly in the OT (even considering various probability density functions) a statistical effect arises: small misorientations are favored[1]. Thus, BMDs obtained with this method are very likely to be similar. That is why we need a specific procedure assigning crystal orientations in order to obtain various prescribed BMDs so that the space of possible BMDs can be explored efficiently. A Monte-Carlo optimization technique has been proposed in [85] and a rank optimization has been developed in [86]. However, optimization necessitates to re-assign several times orientations until the BMD matches the prescribed distribution, which is time consuming. As a large *database* is aimed, an alternative approach reaching very short computation time has been developed.

A stochastic step by step procedure is proposed for the orientation assignment (see figure 3.2). The target BMD is defined by a probability density function denoted by $p(\Delta\theta)$. The procedure is as follows. An initial grain is selected randomly and the orientation is arbitrarily set to θ_0 (in practice $\theta_0 = 0$). Then, one neighbor is selected, and its orientation θ_1 is assigned randomly as a draw of $p(\Delta\theta_{01})$. Indeed, θ_0 being already assigned, the probability of θ_1 is conditional to θ_0, and reads as the probability of the misorientation angle $\Delta\theta_{01} = |\theta_1 - \theta_0|$. More formally, this reads:

$$p(\theta\,|\,\theta_0) = p(\Delta\theta_{01}) \tag{3.8}$$

where $p(\theta\,|\,\theta_0)$ is the probability density for θ_1 under the condition that θ_0 has already been assigned. This procedure is repeated to another neighbor etc. At some point, the selected grain denoted by i have several already assigned neighbors denoted by $j_1, \cdots, j_k$, whose orientations are denoted by $\theta_{j_1}, \cdots, \theta_{j_k}$ (see figure 3.2). Therefore, the orientation θ_i

[1] In 3D, uniform random orientation distribution classically leads to the Mackenzie disorientation distribution [84], which is not obtained in 2D. Indeed, plane hexagonal polycrystals correspond in 3D to fcc grains with the $\langle 111 \rangle$ direction aligned with the out of plane direction, which is a strong non-random texture.

is determined as a draw of the following conditional probability density function:

$$p(\theta\,|\,\theta_{j_1},\cdots,\theta_{j_k}) = p(\Delta\theta_{ij_1},\cdots,\Delta\theta_{ij_k}) \tag{3.9}$$

where $p(\theta\,|\,\theta_{j_1},\cdots,\theta_{j_k})$ is the probability density for θ_i under the condition that $\theta_{j_1},\cdots,\theta_{j_k}$ have already been assigned, $\Delta\theta_{ij_1},\cdots,\Delta\theta_{ij_k}$ are the misorientation angles between the grain i and $j_1,\cdots,j_k$ respectively, and $p(\Delta\theta_{ij_1},\cdots,\Delta\theta_{ij_k})$ is the joint probability of misorientation. For the sake of simplicity, it is assumed that grain boundary misorientations are independent, hence:

$$p(\theta\,|\,\theta_{j_1},\cdots,\theta_{j_k}) = \prod_{m=1}^{k} p(\Delta\theta_{ij_m}) \tag{3.10}$$

This process is repeated until all grain orientations have been assigned, as shown in figure 3.2. This probabilistic procedure is very fast but not exact. However, the obtained

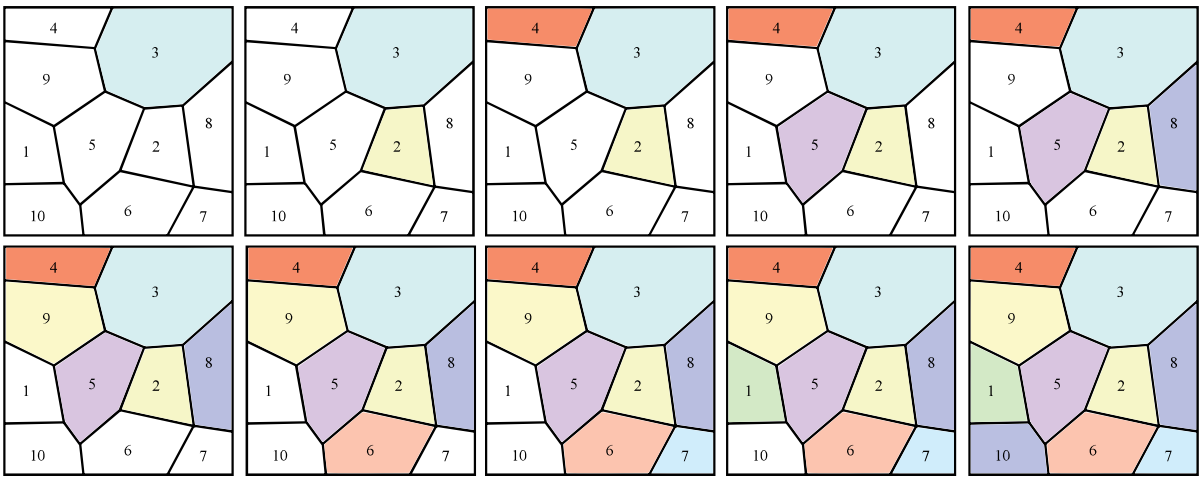

Figure 3.2: Principle of probabilistic orientation assignment

BMD is sufficiently close to the target BMD to enable an efficient exploration of possible BMDs. For instance several orientations are assigned to the same Voronoi-Laguerre tessellation in figure 3.3. The obtained BMD is presented with histograms and the targeted BMD is presented in solid line. These examples have been generated with beta probability density $\mathscr{B}(\alpha,\beta)$ for the targeted BMD with parameters $\alpha = 1,2$ and $\beta = 2,3,4$.

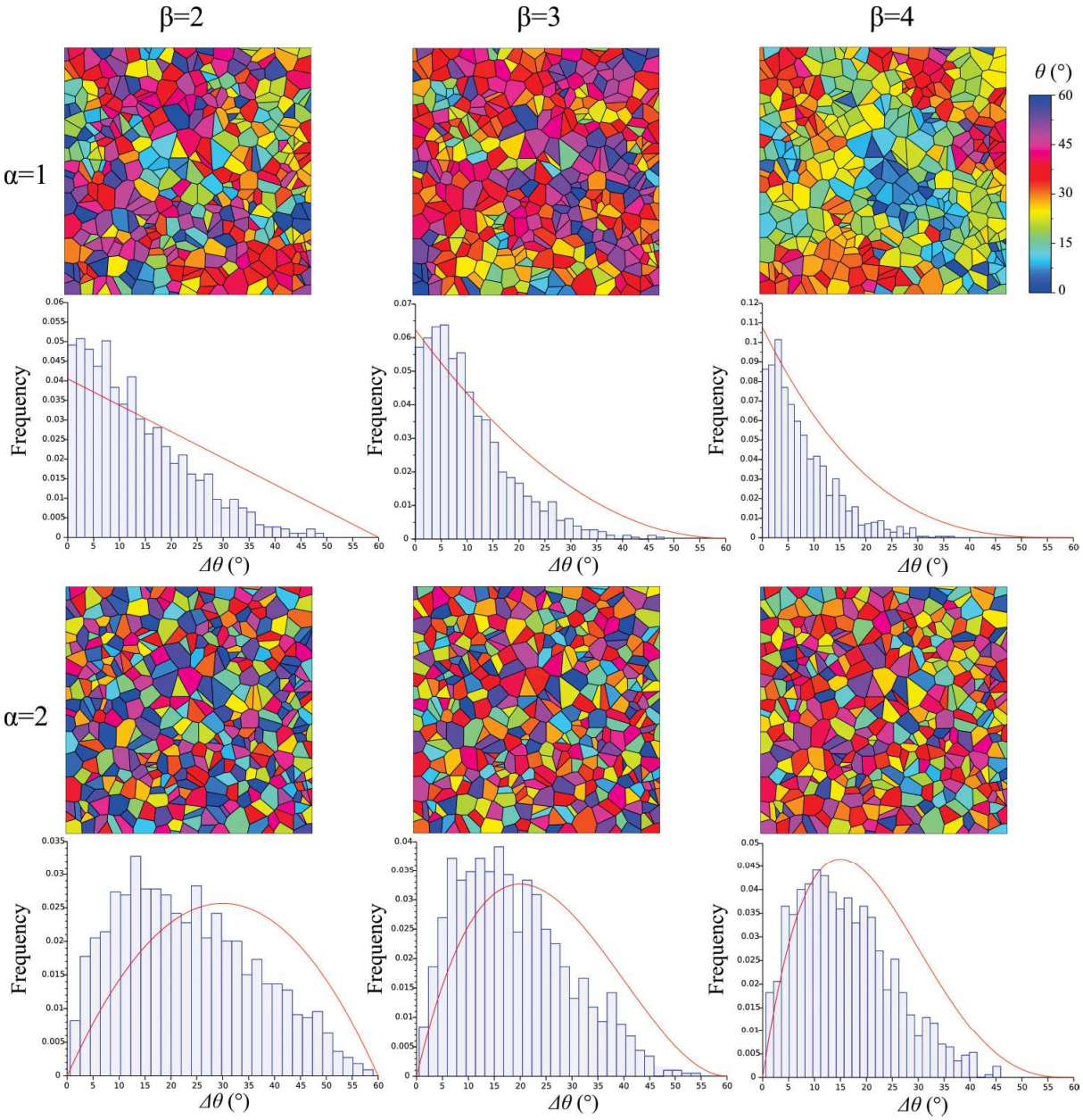

Figure 3.3: Examples of probabilistic orientation assignment. OTs with BMD histograms and targeted probability density function (red line)

3.4 Representative volume element and mass conservation

The proposed mesoscopic model is meant to be used in an upscaling strategy. Thus, the mesoscopic evolution law should not be derived for an entire polycrystalline structure containing all the grains of the macroscopic object. Instead, the mesoscopic model should be derived for RVEs supposed to be embedded in a much larger polycrystalline structure. As a result, boundary conditions should be applied to the RVE to take into account interactions with the rest of the polycrystal. Boundary conditions consist of misorientations at the boundaries of the RVE. This section deals with the definition of RVEs and difficulties related to mass conservation.

3.4.1 Boundary conditions

A simple way to define the RVE is to generate an OT containing N grains and to consider a subset of n connected grains (with $n < N$) among the N grains and not belonging to the edges of the OT. Thus, all GBs in the RVE, including boundaries of the RVE, have a misorientation angle (see figure 3.4). Hence, boundary conditions are naturally defined. The evolution of the RVE is obtained by updating only the parameters of the n connected grains, while the parameters of the other grains are fixed. Therefore, the set of parameters describing the RVE is denoted by $\mathscr{P}_{\text{RVE}}$ and reads:

$$\mathscr{P}_{\text{RVE}} = \left\{ \underline{\alpha} = (\underline{x}, \underline{y}, \underline{w}, \underline{\theta}) \in [0,1]^n \times [0,1]^n \times \mathbb{R}^n \times \left[0, \frac{\pi}{3}\right]^n \right\} \tag{3.11}$$

It should be mentioned that the constraint (3.2) that applies to the entire OT, does not apply to the RVE. Indeed, the constraint implies that there are $N-1$ independent weights. The n weights of the RVE are therefore independent. The set $\mathscr{P}_{\text{RVE}}$ is a $4n$ dimensional vector space. The evolution law for the RVE is similar to (3.7) and reads for $\underline{\alpha} = (\underline{x}, \underline{y}, \underline{w}, \underline{\theta}) \in \mathscr{P}_{\text{RVE}}$: $\dot{\underline{w}} = f(\underline{\alpha})$.

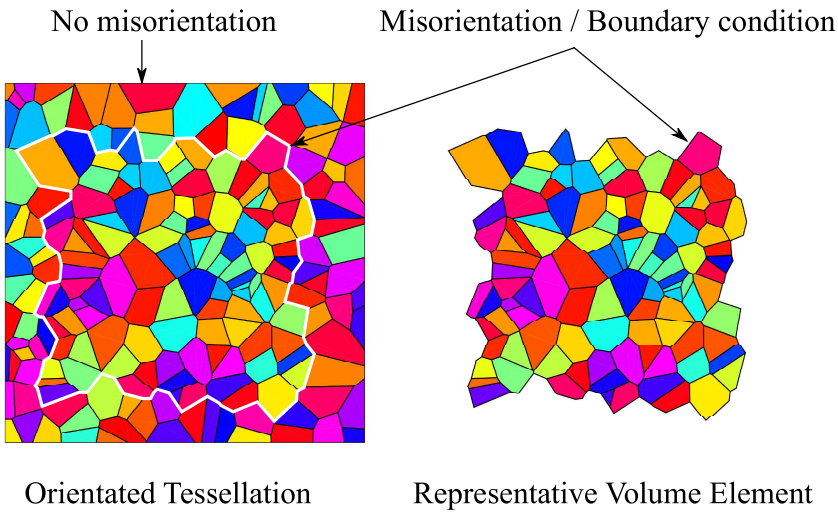

Figure 3.4: Definition of the RVE with boundary condition

As the weights of grains surrounding the RVE are fixed, if the evolution law is not constrained, then the RVE tends to shrink to minimize the GB energy similarly to a spherical grain in an infinite matrix. This issue is overcome by imposing mass conservation for the RVE as a constraint. This anomalous shrinkage is demonstrated as follows. A RVE is defined from an OT. A reference computation is performed for the entire OT (all weights are updated at each time step). In this case there is no constraint, as mass conservation is automatically verified. Then, two computations (with and without mass conservation) are performed for the RVE, and compared to the reference computation. The evolution law is derived in section 3.6, the purpose in this section being only to present the effect of mass conservation of the RVE. Results are presented in figure 3.5 (to facilitate the interpretation, grains not belonging to the RVE are distinguished by a white solid line). The OT physical size is $L_0 = 1$ mm, and initially consists of 200 grains. The figure 3.5 clearly shows that

ensuring mass conservation in the mesoscopic evolution law enables to overcome the difficulty, even though it does not enable to obtain exactly the same evolution as the entire OT.

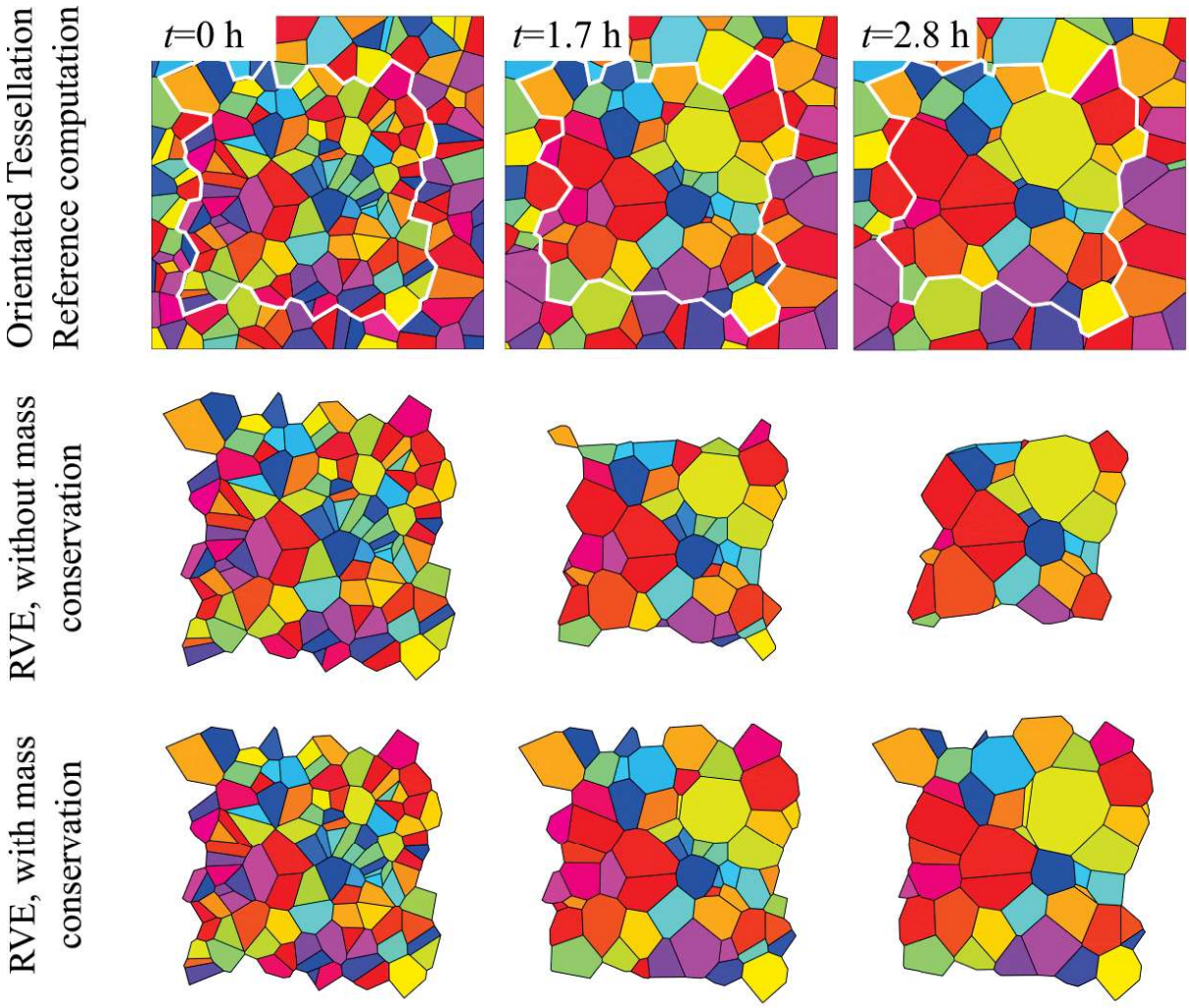

Figure 3.5: Comparison between OT and RVE respective evolutions (with or without mass conservation)

3.4.2 Mass conservation

Mass conservation has been introduced as an ad hoc principle in order to avoid anomalous shrinkage of RVEs. Mass is automatically conserved in OTs as they represent the entire object (no surrounding grains). However, the RVE exchanges matter with the rest of the OT (some grains grow at the expense of grains not belonging to the RVE) and mass conservation is not guaranteed. Ultimately, if the RVE were constituted of a single grain, then mass conservation principle would be obviously violated. Nevertheless, if a sufficient number of grains are considered in the RVE, the growth of some grains compensates the shrinkage of the others, and mass is statistically conserved (even though there are slight

variations). This idea is demonstrated as follows. The evolution of an OT containing initially 5000 grains is computed (see figure 3.6). This OT represents a square sample with a side $L_0 \approx 7$ mm. The average grain size is around 100 µm. The total mass is conserved as the OT does not exchange mass with the exterior. In contrast, several groups of connected grains are randomly selected in the OT and their mass is computed as a function of time. (In practice the surface is computed as the density is constant). For instance, the evolution of 9 groups is presented in figure 3.7. The positive relative mass variation is denoted by $\Delta\varepsilon(t)$ and reads:

$$\Delta\varepsilon(t) = \frac{|M_{\mathrm{RVE}}(t) - M_{\mathrm{RVE}}(0)|}{M_{\mathrm{RVE}}(0)} \tag{3.12}$$

where $M_{\mathrm{RVE}}(t)$ is the mass of the group at time t. For each group, $t_{\mathrm{RVE}}^{x\%}$ denotes the time needed to decrease the initial number of grains n_{RVE} by $x\%$. The maximum relative mass variation until $t_{\mathrm{RVE}}^{x\%}$ is denoted by $\Delta\varepsilon_m^{x\%}$ and reads:

$$\Delta\varepsilon_m^{x\%} = \max_{t\in[0,t_{\mathrm{RVE}}^{x\%}]} \Delta\varepsilon(t) \tag{3.13}$$

For each group, the maximum relative mass variation until the initial number of grains decreases by 33% is presented in figure 3.8. For groups with more than 110 grains $\Delta\varepsilon_m^{33\%}$ is below 4%. Thus, even for significant evolution, mass conservation is approximately verified for sufficiently large groups of connected grains. For smaller groups $\Delta\varepsilon_m^{33\%}$ may reach higher values, and the statistical mass conservation is not guaranteed. This analysis enables to determine the minimal number of grains to obtain an approximate statistical mass conservation.

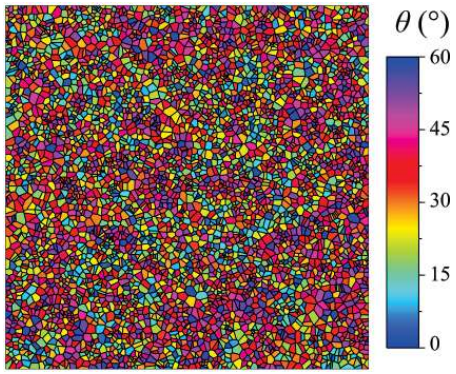

Figure 3.6: Initial 5000 grains polycrystal

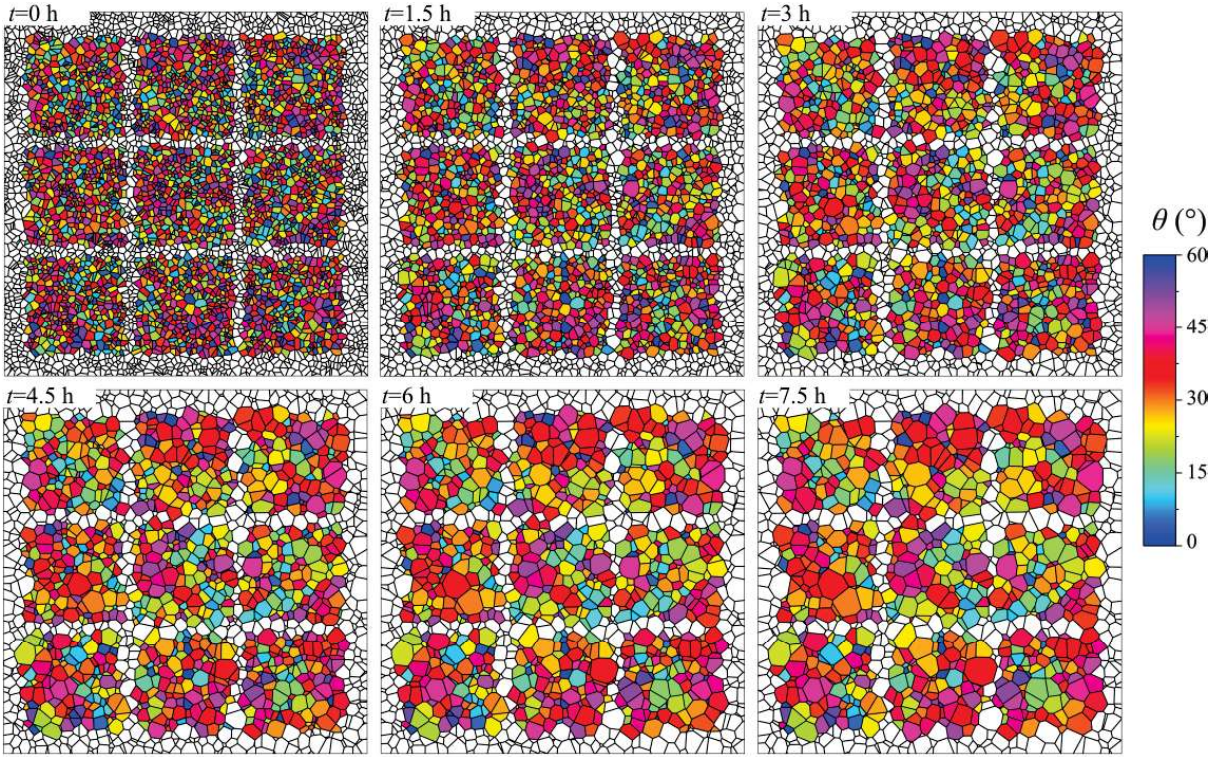

Figure 3.7: Evolution of 9 groups of connected grains in a 5000 grains polycrystal

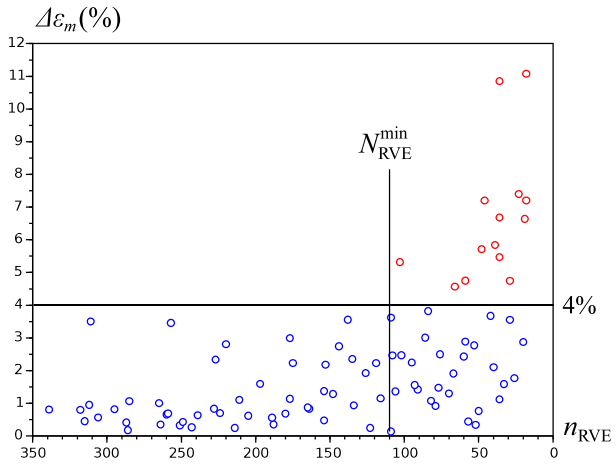

Figure 3.8: Determination of the minimum size of the RVE

3.5 Microscale mechanisms

Before establishing the mesoscopic evolution law taking into account mass conservation (see section 3.6), energetic mechanisms at the microscopic scale are introduced so that the mesoscopic evolution law relies on a physically consistent basis. Indeed, different energetic contributions are considered at the microscopic scale, namely: (i) the anisotropic GB energy (due to crystallographic misorientation) and (ii) the dissipated power due to crystal plasticity for very low angle boundaries and atomic jumps and atomic diffusion for high and intermediate angle boundaries respectively.

3.5.1 Grain boundary energy

GBs are defects that have an excess free energy per unit area with respect to the default stack energy. Indeed, the GB thickness is of a few atomic planes, where crystal lattices are disturbed to accommodate geometrical incompatibilities due to misorientation. In addition to temperature, five independent parameters enables to classify GBs (three describe the misorientation and two describe the orientation of the GB plane). In 2D, only two independent parameters are necessary (one describes the misorientation and one the GB plane). Various methods have been developed to compute and measure GB energy as a function of these five parameters (see [32] for a review of the literature). Thus, considering two-dimensional setting, the energy per unit area γ_{ij} of the GB between grains i and j (i.e., $(i,j) \in I_{\text{RVE}}$) reads:

$$\gamma_{ij} = \gamma(T, \Delta\theta_{ij}, \varphi_{ij}) \tag{3.14}$$

where γ is a function to be determined, T is the temperature, $\Delta\theta_{ij}$ is the crystal lattice misorientation between grains i and j defined by:

$$\Delta\theta_{ij} = \left|\theta_j - \theta_i\right| \in \left[0, \frac{\pi}{3}\right] \tag{3.15}$$

and where φ_{ij} is the angle of the GB plane. In 2D, one of the most popular approach is the Read & Shockley [1] model relying on dislocation calculation within the framework of continuum mechanics. An explicit analytic GB energy as a function of misorientation and GB plane orientation has been obtained. However, the range of validity of the Read & Shockley formula is limited to small misorientation angles and do not account for the energy cusps at certain misorientation angles. To overcome this difficulty, molecular dynamic computations have been proposed to compute GB energies as a function of the five parameters characterizing GBs. Among early works, Wolf [34–37] provided a systematic investigation of GB energy in fcc metals. Many other molecular dynamic computations have been carried out to determine GB energy (e.g., [38–40]). However, using molecular dynamics online during a simulation of grain growth would be computationally costly. Thus, some approaches attempt to establish simple models of GB energy based on multiscale strategies relying on molecular dynamic computations (e.g., [41]), whereas other approaches simply rely on interpolations of molecular dynamic computations (e.g., [42]). In this contribution such a strategy is adopted, molecular dynamic computations are performed and then interpolated as a function of misorientation.

To reduce the number of computations, it is assumed that the dependence on φ is negligible. Thus, the function $\gamma(T, \Delta\theta, \varphi)$ is approximated by a function $\gamma(T, \Delta\theta)$. Thus, $\langle 111 \rangle$ symmetric tilt boundaries have been simulated for various misorientation angles $\Delta\theta$. GB energies were computed by minimizing system energy using the conjugate-gradient method in the LAMMPS code [33] at $T = 0$ K with embedded-atom method (EAM) interatomic potentials. The chosen interatomic potential [44] is adapted for Fe (pure iron) and presents the advantage to be stable at low temperature for fcc (although Fe presents a bcc structure at low temperature). The interatomic distance for the fcc structure is $a \approx 3.6057$ Å, and the default stack energy is $E_{ds} \approx 4.18127$ eV (exact values can be found on the OpenKIM project `https://openkim.org` [87]). The approach is similar to [38, 39], using computation cell with periodic boundary conditions. The misorientation angle is defined by two integers n_x and n_y as shown in figure 3.9. For instance, for $\langle 001 \rangle$ tilt in fcc structures, periodicity leads to consider square simulation cell with a side being a multiple of

$a\sqrt{n_x^2+n_y^2}$ (see figure 3.9 left). However, for $\langle 111\rangle$ tilt in fcc structures, periodicity leads to consider prismatic simulation cell with a $\pi/3$ skew angle as shown in figure 3.9 right, and a side being a multiple of $(a/\sqrt{2})\sqrt{n_x^2+n_y^2+n_x n_y}$.

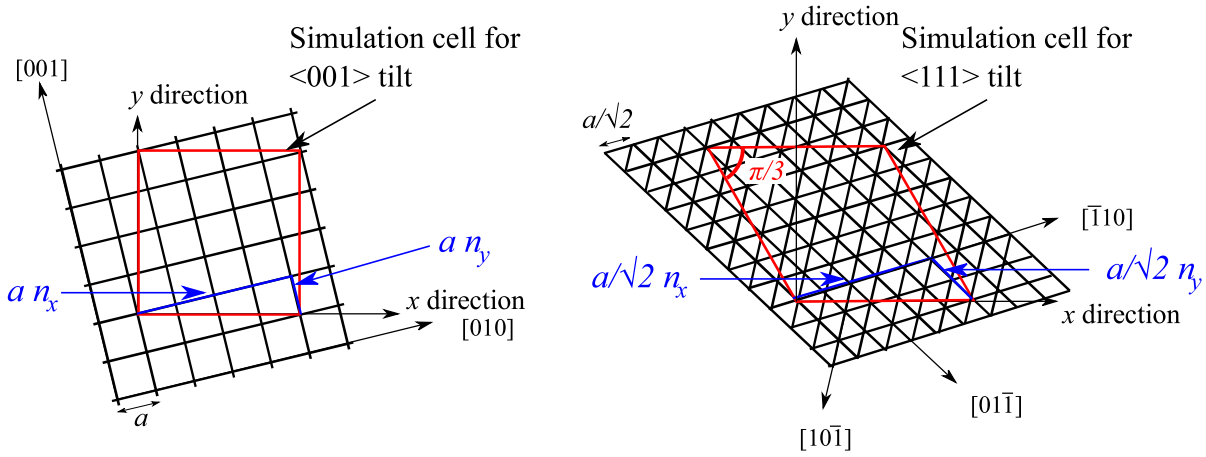

Figure 3.9: Simulation cell for molecular dynamic computations

Similarly to [39], a rigid body translation of one lattice with respect to the other is used to sample different starting configurations. In addition, since atoms in the two lattices are built up to the GB plane, an atom deletion criterion is used to remove atoms that may physically lie too close to each other. For each misorientation angle $\Delta\theta$, different rigid body translations ($0\,a$ to $0.5\,a$ with a step of $0.05\,a$) and atom deletion criteria ($0.3\,a$ to $0.7\,a$ with a step of $0.05\,a$), are tested, and only the minimum GB energy is stored for each tested misorientation angle. Results are presented in figure 3.10 with a piecewise interpolation function introduced in [88]:

$$\begin{cases} \gamma(0,\Delta\theta) = \gamma_1 \sin\left(\dfrac{\pi}{2}\dfrac{\Delta\theta}{\Delta\theta_1}\right)\left[1-a_1\ln\left(\sin\left(\dfrac{\pi}{2}\dfrac{\Delta\theta}{\Delta\theta_1}\right)\right)\right] \\ (0\le\Delta\theta\le\Delta\theta_1) \\ \gamma(0,\Delta\theta) = \gamma_2+(\gamma_1-\gamma_2)\sin\left(\dfrac{\pi}{2}\dfrac{\Delta\theta-\frac{\pi}{3}}{\Delta\theta_1-\frac{\pi}{3}}\right)\left[1-a_2\ln\left(\sin\left(\dfrac{\pi}{2}\dfrac{\Delta\theta-\frac{\pi}{3}}{\Delta\theta_1-\frac{\pi}{3}}\right)\right)\right] \\ \left(\Delta\theta_1\le\Delta\theta\le\dfrac{\pi}{3}\right) \end{cases} \tag{3.16}$$

where $\gamma_1 = 0.95$ J.m^{-2}, $\gamma_2 = 0.67$ J.m^{-2}, $a_1 = 0.5$, $a_2 = 0.1$ and $\Delta\theta_1 = \pi/6$.

The grain GB energy has been interpolated for $T = 0$ K (i.e., $\gamma(0,\Delta\theta)$). However, the temperature dependence of GB energy is needed for simulating grain growth. In this contribution, we assume that the temperature dependence is in $G(T)/G(0)$ similarly to [89], where $G(T)$ is the shear coefficient:

$$\gamma(T,\Delta\theta) = \frac{G(T)}{G(0)}\gamma(0,\Delta\theta) \tag{3.17}$$

Data for Fe extracted from [90] are used to calibrate $G(T)$:

$$G(T) = a_G\,T + b_G \tag{3.18}$$

where $b_G \approx 88134$ MPa and $a_G \approx -24$ MPa.K^{-1}.

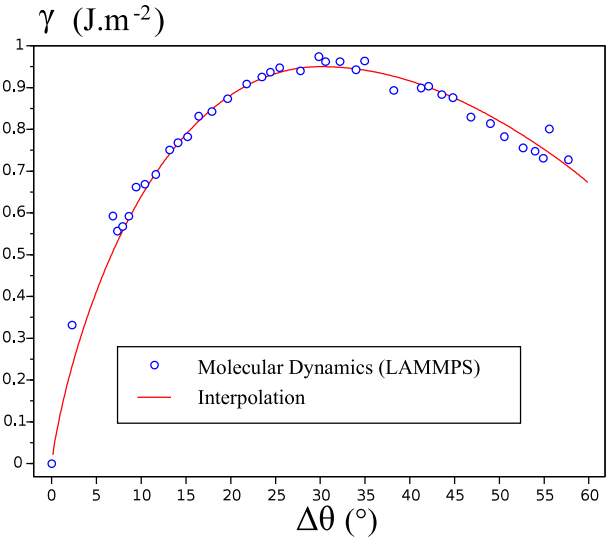

Figure 3.10: Grain boundary energy per unit area at $T = 0$ K for symmetric tilt ⟨111⟩

3.5.2 Dissipated power through grain boundary motion

Grain boundary energy enables to compute the driving force that tends to make evolve the system. Moreover, resistive mechanisms should be considered to control the speed at which the system may evolve. Thus, the dissipated power through any virtual motion of the GB is detailed in this section. For very low angle boundaries, the dissipative mechanism during GB motion can be interpreted within the framework of crystal plasticity. Indeed, slip systems are activated so that the crystal orientation of one grain can be transformed into the crystal orientation of the other grain, as shown in figure 3.11a (where v^* is a virtual normal velocity of the GB).

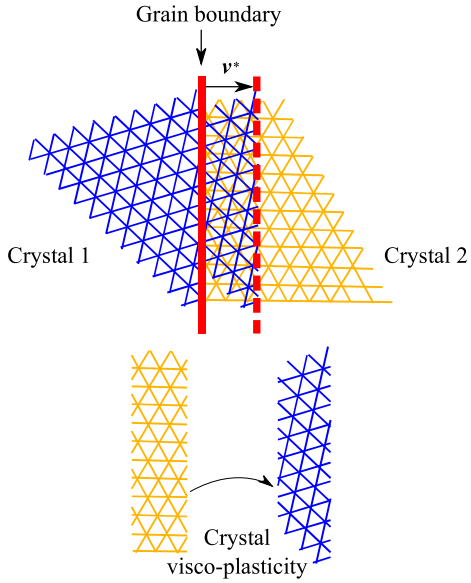

(a) Crystal visco-plasticity during grain boundary motion

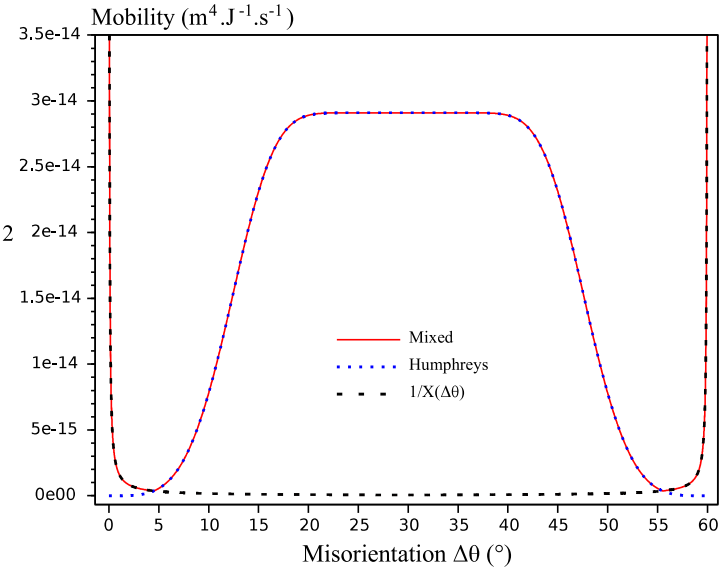

(b) Mobility as a function of misorientation

Figure 3.11: Dissipative mechanisms and mobility

Consider v_{ij}^* a virtual velocity of the grain boundary (i,j). The dissipated power per unit area reads:

$$D_{ij}^* = D(T, \Delta\theta_{ij}, v_{ij}^*) \tag{3.19}$$

where D is a function to be determined. In [59, 60], D has been determined analytically within the framework of crystal plasticity. The calculation relies on two plane hexagonal semi-infinite crystals with a moving GB. Thus, six slip systems may be activated to transform the crystal orientation in the volume covered by the GB during motion (see. figure 3.11a). For practical calculation, the plastic slip is assumed to obey Schmids law without hardening, while elasticity is neglected. The following dissipated power per unit area is obtained:

$$D(T, \Delta\theta_{ij}, v_{ij}^*) = \tau_c X(\Delta\theta_{ij}) \left| v_{ij}^* \right| \tag{3.20}$$

where τ_c is the critical shear stress and X is the following function:

$$X(\Delta\theta) = \frac{6}{\pi}\left(\frac{\pi}{3} + 2\sqrt{3}\ln\left(\frac{\sqrt{3}}{2}\right)\right)\min\left\{\Delta\theta, \frac{\pi}{3} - \Delta\theta\right\} \tag{3.21}$$

Since grain growth is viscous, the analytic computation proposed in [59, 60] is simply adapted for crystal visco-plasticity by considering that the critical shear stress τ_c linearly depends on $\left| v_{ij}^* \right|$, which reads:

$$\tau_c = \frac{1}{m(T)} \left| v_{ij}^* \right| \tag{3.22}$$

where $m(T)$ is a grain mobility ($\mathrm{m}^4.\mathrm{J}^{-1}.\mathrm{s}^{-1}$) that can be related to the curvature driven mobility $m_{CD}(T, \Delta\theta)$ introduced in (1.1). The mobility $m(T)$ is calibrated so that the shrinkage of an hexagonal grain (computed according to the present model) evolves at the same speed as the shrinkage of a circular grain according to the curvature driven evolution law (1.1). More precisely, it is shown in A.2 that:

$$m_{CD}(T, \Delta\theta) = \frac{m(T)}{X(\Delta\theta)} \tag{3.23}$$

Hence the dissipated power per unit area:

$$D(T, \Delta\theta_{ij}, v_{ij}^*) = \frac{\left[v_{ij}^* \right]^2}{m_{CD}(T, \Delta\theta)} \tag{3.24}$$

Thus, the dissipated power (3.24) corresponds to what is obtained for the curvature driven growth.

For very low angle boundaries, $m_{CD}(T, \Delta\theta)$ varies in $1/\Delta\theta$ (see (3.23)), which is consistent with the expression obtained by considering the movement of boundaries in which the dislocations are spaced far apart [2]. However, for high angle boundaries the dislocation cores overlap, and the dissipative mechanism is more likely related to atom jumps, and for intermediate angle boundaries, dissipation is attributed to diffusion of atoms over a certain distance [2]. Since the mobility completely determines the dissipated power through any virtual speed (see (3.24)), real dissipative mechanisms are indirectly taken into account in the mobility function $m_{CD}(T, \Delta\theta)$. There are significant evidences [2] that for

intermediate and high angle boundaries the mobility can be approximated by the following sigmoid function introduced in [61, 62]:

$$m_{CD}(T,\Delta\theta) = m_{\max}(T)\left(1-\exp\left[-K\left(\frac{\Delta\theta}{\Delta\theta_1}\right)^p\right]\right) \tag{3.25}$$

where K is a positive coefficient, p is positive exponent, $m_{\max}$ is the maximum mobility and $\Delta\theta_1$ is a threshold. However, (3.25) should not be used for very low angle boundaries because $m_{CD}(T,\Delta\theta)$ would tend to 0 when $\Delta\theta$ tends to zero which would lead to an infinite dissipated power (see (3.24)). This difficulty is overcome in this work by introducing a mixed mobility based on (3.23) for very low angle boundaries and (3.25) for higher angle boundaries, which reads:

$$m_{CD}(T,\Delta\theta) = \begin{cases} \dfrac{m(T)}{X(\Delta\theta)} & \text{if} \quad \min\left\{\Delta\theta, \frac{\pi}{3}-\Delta\theta\right\} \leq \Delta\theta_0 \\ m_{\max}(T)\left(1-\exp\left[-K\left(\dfrac{\Delta\theta}{\Delta\theta_1}\right)^p\right]\right) & \text{if} \quad \min\left\{\Delta\theta, \frac{\pi}{3}-\Delta\theta\right\} \geq \Delta\theta_0 \end{cases} \tag{3.26}$$

where $\Delta\theta_0$ is a threshold between very low angle boundaries and high and intermediate angle boundaries. In addition, continuity reads:

$$m(T) = m_{\max}(T)\left(1-\exp\left[-K\left(\frac{\Delta\theta_0}{\Delta\theta_1}\right)^p\right]\right)X(\Delta\theta_0) \tag{3.27}$$

In figure 3.11b the mobility (3.26) is presented with parameters listed in table 3.1.

3.6 Mesoscopic evolution law

In this section, the mesoscopic evolution law accounting for mass conservation is derived. This evolution law is adapted for RVEs with boundary conditions (see section 3.4.1). The total energy per unit depth (denoted by $\mathscr{E}$) is considered in the RVE as well as the total dissipated power per unit depth (denoted by $\mathscr{D}$). For $\alpha \in \mathscr{P}_{\text{RVE}}$:

$$\begin{cases} \mathscr{E}(T,\underline{\alpha}) = L_0 \displaystyle\sum_{(i,j)\in I_{\text{RVE}}} l_{ij}\gamma_{ij} \\ \mathscr{D}(T,\underline{\alpha},\underline{v}^*) = L_0 \displaystyle\sum_{(i,j)\in I_{\text{RVE}}} l_{ij}D^*_{ij} \end{cases} \tag{3.28}$$

where $I_{\text{RVE}} \subset I_{GB}$ is the set of GBs in the RVE. There are n grains in the RVE and n_{GB} GBs with $n_{GB} = \text{card}\,[I_{\text{RVE}}]$. In addition, l_{ij} is the dimensionless joint length, and γ_{ij} and D^*_{ij} are computed from (3.17) and (3.24) respectively. Moreover, $\underline{v}^*$ is the following vector:

$$\underline{v}^* = \left(v^*_{ij}\right)_{(i,j)\in I_{\text{RVE}}} \tag{3.29}$$

By combining (3.24) and (3.29) one obtains:

$$\mathscr{D}(T,\underline{\alpha},\underline{v}^*) = L_0\,\underline{v}^*.\underline{\underline{\chi}}(T,\underline{\alpha}).\underline{v}^* \tag{3.30}$$

where $\underline{\underline{\chi}}(\underline{\alpha})$ is a diagonal second order tensor of size $n_{GB}\times n_{GB}$ whose diagonal reads:

$$\forall (i,j)\in I_{\text{RVE}}, \quad \chi(T,\Delta\theta_{ij}) = \frac{l_{ij}}{m_{CD}(T,\Delta\theta_{ij})} \tag{3.31}$$

As seeds and crystalline orientations are fixed (i.e., $\underline{\dot{x}} = \underline{\dot{y}} = 0$ and $\underline{\theta} = 0$), and considering any virtual variation of weights $\underline{\dot{w}}^*$, it is straightforward to demonstrate that:

$$v_{ij}^* = L_0 \frac{\dot{w}_i^* - \dot{w}_j^*}{2d_{ij}} \tag{3.32}$$

where d_{ij} is the dimensionless distance between seeds:

$$d_{ij} = \left\| \begin{pmatrix} x_i \\ y_i \end{pmatrix} - \begin{pmatrix} x_j \\ y_j \end{pmatrix} \right\| \tag{3.33}$$

It is clear in (3.32) that for each GB an arbitrary choice is made for the positive direction of the normal velocity v_{ij}^*, which has no consequence as the square of the virtual velocity arises in the dissipated power. Hence:

$$\underline{v}^* = L_0 \underline{\underline{K}}(\underline{\alpha}).\underline{\dot{w}}^* \tag{3.34}$$

where $\underline{\underline{K}}(\underline{\alpha})$ is a second order tensor of size $n_{GB} \times n$, which can be evaluated analytically:

$$\underline{\underline{K}}(\underline{\alpha}) = \begin{matrix} \\ (i,j) \end{matrix} \begin{matrix} \begin{matrix} \quad & \quad & \quad & i & \quad & \quad & \quad & j & \quad & \quad & \quad \end{matrix} \\ \begin{bmatrix} \vdots & \vdots & \vdots & \vdots & \vdots & \vdots & \vdots & \vdots & \vdots & \vdots & \vdots \\ 0 & \cdots & 0 & \frac{1}{2d_{ij}} & 0 & \cdots & 0 & -\frac{1}{2d_{ij}} & 0 & \cdots & 0 \\ \vdots & \vdots & \vdots & \vdots & \vdots & \vdots & \vdots & \vdots & \vdots & \vdots & \vdots \end{bmatrix} \end{matrix} \tag{3.35}$$

The tensor $\underline{\underline{K}}(\underline{\alpha})$ represents the link between the normal speed of the n_{GB} GBs and the n weights. However, only the weights are controlled in the evolution law. Thus, consider $\underline{\underline{R}}(\underline{\alpha})$ the following second order tensor of size $n \times n$:

$$\underline{\underline{R}}(T,\underline{\alpha}) = \underline{\underline{K}}(\underline{\alpha})^T.\underline{\underline{\chi}}(T,\underline{\alpha}).\underline{\underline{K}}(\underline{\alpha}) \tag{3.36}$$

As already mentioned, the constraint (3.2) does not apply for the RVE (only for the entire OT), thus $\underline{\underline{R}}(T,\underline{\alpha})$ is invertible and symmetrical positive-definite. For any virtual weight variation $\underline{\dot{w}}^*$, the total dissipated power per unit depth reads:

$$\mathscr{D}(T,\underline{\alpha},\underline{\dot{w}}^*) = L_0^3 \underline{\dot{w}}^* \cdot \underline{\underline{R}}(T,\underline{\alpha}) \cdot \underline{\dot{w}}^* \tag{3.37}$$

The energy balance equation obtained from the first and second laws of thermodynamics holds for any possible state $\underline{\alpha}$ and any possible evolution $\underline{\dot{w}}$ (real not virtual):

$$\mathscr{D}(T,\underline{\alpha},\underline{\dot{w}}) + \dot{\mathscr{E}}(T,\underline{\alpha}) = 0 \tag{3.38}$$

Hence:

$$L_0^3 \underline{\dot{w}} \cdot \underline{\underline{R}}(T,\underline{\alpha}) \cdot \underline{\dot{w}} + \frac{\partial \mathscr{E}}{\partial \underline{w}}(T,\underline{\alpha}) \cdot \underline{\dot{w}} = 0 \tag{3.39}$$

In addition, the mass balance equation reads (if density is assumed constant):

$$\dot{S}(\underline{\alpha}) = \frac{\partial S}{\partial \underline{w}} \cdot \underline{\dot{w}} = 0 \tag{3.40}$$

where S denotes the total area of the n grains in the RVE.

The maximum dissipation principle [45] under the constraint (3.39) and (3.40) is invoked to determine the evolution law:

$$\underline{\dot{w}}_{\text{meso}} = \begin{cases} \underset{\underline{\dot{w}} \in \mathbb{R}^n}{\operatorname{argmax}} \left[L_0^3 \underline{\dot{w}} \cdot \underline{\underline{R}}(T, \underline{\alpha}) \cdot \underline{\dot{w}} \right] \\ \text{subjected to.} \quad L_0^3 \underline{\dot{w}} \cdot \underline{\underline{R}}(T, \underline{\alpha}) \cdot \underline{\dot{w}} + \dfrac{\partial \mathscr{E}}{\partial \underline{w}}(T, \underline{\alpha}) \cdot \underline{\dot{w}} = 0 \\ \qquad\qquad \dfrac{\partial S}{\partial \underline{w}} \cdot \underline{\dot{w}} = 0 \end{cases} \tag{3.41}$$

The maximization problem (3.41) is solved analytically by Lagrangian multiplier method. Consider the following Lagrangian:

$$\mathscr{L}(\underline{\dot{w}}, \lambda_1, \lambda_2) = L_0^3 \underline{\dot{w}} \cdot \underline{\underline{R}} \cdot \underline{\dot{w}} + \lambda_1 \left(L_0^3 \underline{\dot{w}} \cdot \underline{\underline{R}} \cdot \underline{\dot{w}} + \frac{\partial \mathscr{E}}{\partial \underline{w}} \cdot \underline{\dot{w}} \right) + \lambda_2 \frac{\partial S}{\partial \underline{w}} \cdot \underline{\dot{w}} \tag{3.42}$$

The optimality condition reads:

$$\frac{\partial \mathscr{L}}{\partial \underline{\dot{w}}} = 2 L_0^3 (1 + \lambda_1) \underline{\underline{R}} \cdot \underline{\dot{w}} + \lambda_1 \frac{\partial \mathscr{E}}{\partial \underline{w}} + \lambda_2 \frac{\partial S}{\partial \underline{w}} = 0 \tag{3.43a}$$

$$\frac{\partial \mathscr{L}}{\partial \lambda_1} = L_0^3 \underline{\dot{w}} \cdot \underline{\underline{R}} \cdot \underline{\dot{w}} + \frac{\partial \mathscr{E}}{\partial \underline{w}} \cdot \underline{\dot{w}} = 0 \tag{3.43b}$$

$$\frac{\partial \mathscr{L}}{\partial \lambda_2} = \underline{\dot{w}} \cdot \frac{\partial S}{\partial \underline{w}} = 0 \tag{3.43c}$$

Contracting (3.43a) with $\underline{\dot{w}}$, one obtains:

$$2 L_0^3 (1 + \lambda_1) \underline{\dot{w}} \cdot \underline{\underline{R}} \cdot \underline{\dot{w}} + \lambda_1 \frac{\partial \mathscr{E}}{\partial \underline{w}} \cdot \underline{\dot{w}} + \lambda_2 \underline{\dot{w}} \cdot \frac{\partial S}{\partial \underline{w}} = 0 \tag{3.44}$$

Considering (3.43b) and (3.43c), (3.44) reduces to:

$$(2 + \lambda_1) \, \underline{\dot{w}} \cdot \underline{\underline{R}} \cdot \underline{\dot{w}} = 0 \tag{3.45}$$

The tensor $\underline{\underline{R}}$ being symmetric definite-positive, $\underline{\dot{w}} \cdot \underline{\underline{R}} \cdot \underline{\dot{w}} > 0$, thus:

$$\lambda_1 = -2 \tag{3.46}$$

Plugging (3.46) into (3.43a) one obtains:

$$\underline{\dot{w}}_{\text{meso}} = -\frac{1}{L_0^3} \left(\underline{\underline{R}}^{-1} \cdot \frac{\partial \mathscr{E}}{\partial \underline{w}} - \frac{\lambda_2}{2} \underline{\underline{R}}^{-1} \cdot \frac{\partial S}{\partial \underline{w}} \right) \tag{3.47}$$

The multiplier λ_2 is obtained by contracting (3.47) by $\partial S / \partial \underline{w}$ and using (3.43c):

$$\lambda_2 = 2 \frac{\left(\dfrac{\partial S}{\partial \underline{w}} \cdot \underline{\underline{R}}^{-1} \cdot \dfrac{\partial \mathscr{E}}{\partial \underline{w}} \right)}{\left(\dfrac{\partial S}{\partial \underline{w}} \cdot \underline{\underline{R}}^{-1} \cdot \dfrac{\partial S}{\partial \underline{w}} \right)} \tag{3.48}$$

By plugging (3.48) into (3.47) one obtains:

$$\dot{\underline{w}}_{\text{meso}} = -\frac{1}{L_0^3}\left[\underline{\underline{R}}^{-1}\cdot\frac{\partial\mathscr{E}}{\partial\underline{w}} - \frac{\left(\frac{\partial S}{\partial\underline{w}}\cdot\underline{\underline{R}}^{-1}\cdot\frac{\partial\mathscr{E}}{\partial\underline{w}}\right)}{\left(\frac{\partial S}{\partial\underline{w}}\cdot\underline{\underline{R}}^{-1}\cdot\frac{\partial S}{\partial\underline{w}}\right)}\left(\underline{\underline{R}}^{-1}\cdot\frac{\partial S}{\partial\underline{w}}\right)\right] \tag{3.49}$$

Thus, the mesoscopic evolution law reads:

$$\dot{\underline{w}}_{\text{meso}} = -\frac{\underline{\underline{M}}(T,\underline{\alpha})}{L_0^3}\cdot\frac{\partial\mathscr{E}(T,\underline{\alpha})}{\partial\underline{w}} \tag{3.50}$$

where $\underline{\underline{M}}$ is a second order tensor of size $n\times n$ homogenous to a mobility ($\text{m}^4.\text{J}^{-1}.\text{s}^{-1}$) defined as follows:

$$\underline{\underline{M}} = \underline{\underline{R}}^{-1} - \frac{\left(\underline{\underline{R}}^{-1}\cdot\frac{\partial S}{\partial\underline{w}}\right)\otimes\left(\underline{\underline{R}}^{-1}\cdot\frac{\partial S}{\partial\underline{w}}\right)}{\left(\frac{\partial S}{\partial\underline{w}}\cdot\underline{\underline{R}}^{-1}\cdot\frac{\partial S}{\partial\underline{w}}\right)} \tag{3.51}$$

By using (3.28) and (3.17) the mesoscopic evolution law reads:

$$\dot{\underline{w}}_{\text{meso}} = -\frac{\underline{\underline{M}}(T,\underline{\alpha})}{L_0^2}\cdot\left[\sum_{(i,j)\in I_{\text{RVE}}}\frac{\partial l_{ij}}{\partial\underline{w}}\gamma(T,\Delta\theta_{ij})\right] \tag{3.52}$$

The viscous evolution law (3.52) presents a size effect through the scaling parameters L_0. The tensor $\underline{\underline{M}}(T,\underline{\alpha})$ is completely determined by the actual state $(\underline{\alpha},T)$ of the RVE. The gradients $\partial l_{ij}/\partial\underline{w}$ and $\partial S/\partial\underline{w}$ are easily obtained by a geometrical analysis of the OT, which is detailed in A.1.

For simulations of entire OTs in section 3.4 (i.e., all weights are updated and mass conservation is not imposed) the tensor $\underline{\underline{M}}$ in (3.52) should be replaced by:

$$\underline{\underline{M}} = \underline{\underline{R}}^{\dagger} \tag{3.53}$$

where $\underline{\underline{R}}^{\dagger}$ is the *Moore-Penrose* pseudo-inverse of $\underline{\underline{R}}$ that can be computed by singular value decomposition techniques. Indeed, because of the constraint (3.2), there are only $N-1$ independent weights in the entire OT and $\underline{\underline{R}}$ is not invertible (rank $N-1$). It is straightforward to show that the pseudo-inverse enables to obtain the $N-1$ independent weights time derivatives.

3.7 Results

All Voronoi-Laguerre tessellations are produced by using the free software NEPER [29] and the evolution law (3.52) is computed by using the free software SCILAB [91]. The *dialogue* between NEPER and SCILAB is done by writing and reading text files (e.g., Voronoi-Laguerre tessellation files, list of updated weights etc.), which represents the most significant part of the computation time. Despite this unoptimal implementation, computation time is relatively short (e.g., a time increment for a 1000 grains OT is around 1 second on a personal computer). Computation time could be fairly reduced though by implementing the model in C++ language directly in NEPER.

3.7.1 Comparison with von Neumann-Mullins law

In this section, the mesoscopic model is compared to the von Neumann-Mullins (vNM) law [64–66]. The classical vNM law is formulated within a fully isotropic framework (i.e., isotropic GB energy and isotropic mobility), and relies on the curvature driving evolution law (1.1) and the assumption that angles at triple junctions are 120°. Thus, the vNM reads:

$$\frac{\mathrm{d}}{\mathrm{d}t}S_n = \frac{\pi m^*}{3}(n-6) \tag{3.54}$$

where n is the number of sides of the grains family, $\mathrm{d}S_n/\mathrm{d}t$ is the area change rate of n sided grains, and $m^* = \gamma\, m_{CD}$ ($\mathrm{m}^2.\mathrm{s}^{-1}$) is the constant reduced mobility. The vNM law (3.54) applies to individual n sided grains in 2D ideal grain growth [65]. In the following, we determine whether the vNM law is verified in average, where m^* is the average reduced mobility in the entire RVE. In addition, an extended vNM law (3.55) has also been proposed for anisotropic grain growth and tested with a mesoscopic stochastic Monte-Carlo simulations [66].

$$\frac{\mathrm{d}}{\mathrm{d}t}\langle S_n\rangle = \langle m_n^*\rangle\left(\pi - \langle\beta_n\rangle\right)\left(n - \frac{2\pi}{\pi - \langle\beta_n\rangle}\right) \tag{3.55}$$

where $\langle m_n^*\rangle$ is the average reduced mobility, $\langle\beta_n\rangle$ is the average triple junction angle, and where averages are taken over the family of the n sided grains. However, in Voronoi-Laguerre tessellations each grain is polygonal and then $\langle\beta_n\rangle = \pi(n-2)/n$, and therefore $\mathrm{d}\langle S_n\rangle/\mathrm{d}t = 0$ in (3.55). Thus, the extended vNM law is of limited interest within the framework of OTUM. But a simple extended vNM law can be simply derived from (3.54) to take anisotropy into account:

$$\frac{\mathrm{d}}{\mathrm{d}t}\langle S_n\rangle = \frac{\pi\langle m_n^*\rangle}{3}(n-6) \tag{3.56}$$

Three conditions are tested in the following and listed in table 3.1. A purely isotropic condition is tested with constant GB energy γ_0 and mobility m_0 listed in table 3.1. A weakly anisotropic condition is also considered with a constant reduced mobility $m^*(T)$ and an anisotropic GB energy $\gamma(T,\Delta\theta)$, hence $m_{CD}(T,\Delta\theta) = m^*(T)/\gamma(T,\Delta\theta)$, where $m^*(T)$ is given in table 3.1. Despite the anisotropic GB energy and mobility, this condition is similar to the isotropic condition with respect to the curvature driven relation (1.1), which only depends on the reduced mobility. A fully anisotropic condition is also tested by considering (3.26) whose parameters are listed in table 3.1.

A single 2500 grains tessellation is used, and the BMD is assigned as detailed in section 3.3 by a beta probability density function $\mathscr{B}(\alpha,\beta)$ with $\alpha = 2$, $\beta = 3$ (see figure 3.3). Numerical values listed in table 3.1 have been chosen so that the average reduced mobility over the entire RVE is the same for all conditions. For each number of sides, the corresponding normalized area change rate distribution is computed. In figure 3.12a the mean values with standard deviations are presented as a function of the number of sides. As expected, the isotropic condition fits well with the vNM law with small standard deviations (excepted for grains with 3 sides). The same behavior is observed for condition 1 as the reduced mobility is also constant. Larger standard deviations are obtained though, as the vNM law (3.54) relies on isotropic energy, which is not verified for condition 1. Results for condition 2 fits better with the extended vNM law (3.56), which is due to the anisotropy. This result is similar to what is obtained in [66] for the same condition.

Table 3.1: Conditions related to GB energy, mobility and reduced mobility. For all conditions the average reduced mobility over the entire tessellation is $m^* = 0.06\ 10^{-12}$ m^2.s^{-1} and $T = 800°$ (the symbol T is omitted).

	Isotropic 0	Anisotropic 1	Anisotropic 2 (3.26)
GB energy (J.m^{-2})	$\gamma_0 = 0.535$	$\gamma(\Delta\theta)$ (3.16)	$\gamma(\Delta\theta)$ (3.16)
Mobility (m^4.J^{-1}.s^{-1})	$m_0 = 1.112\ 10^{-13}$	-	$m_{\max} = 0.291\ 10^{-13}$
Reduced mobility (m^2.s^{-1})	-	$m^* = 0.06\ 10^{-12}$	-
Coefficient (-)	-	-	$K = 5$
Exponent (-)	-	-	$p = 4$
Misorientation angle (-)	-	-	$\Delta\theta_1 = \pi/9$
Misorientation angle (-)	-	-	$\Delta\theta_0 = 4.5\pi/180$

3.7.2 Comparison with Hillert and Rayleigh distributions

In this section, the equivalent grain size distribution $R/\langle R\rangle$ is analyzed (where R is the grain equivalent radius and $\langle R\rangle$ its average over the RVE). The well known Hillert [67] and Rayleigh distributions are compared to the model for all conditions listed in table 3.1. The tested OT has initially 5000 grains with a misorientation distribution defined by a beta probability density function $\mathscr{B}(\alpha,\beta)$ with $\alpha = 2$, $\beta = 3$. The histograms of $R/\langle R\rangle$ are given for different numbers of grains left in the tessellation after evolution. For all conditions, results are similar to what is observed for purely isotropic grain growth in [82]. Histograms for condition 2 are presented in figure 3.12b. The quasi steady-state distribution is in between Hillert and Rayleigh distributions, and can be fitted by a log-normal density function. In addition, the average grain size $\langle R\rangle$ is presented as a function of time in figure 3.13 for condition 2. The well-known grain growth power law $\langle R\rangle \sim t^n$ (where $n = 1/2$ as for isotropic grain growth) is rapidly reached by the proposed model.

3.7.3 Comparison with experiments

A recent experiment has been conducted on pure iron during annealing for 75 min at 800 °C [83]. The sample is initially fully recrystallized. Grain evolution has been determined in three dimensions using diffraction contrast tomography at a synchrotron source. Since the present model has been derived in 2D, only a plane section of the sample is compared to the model at three different time steps (0 min, 40 min and 75 min). Approximating a real grain structure with a Voronoi-Laguerre tessellation is usually done by numerical optimization. However, as the proposed comparison is mostly qualitative, a rough approximation of the initial grain structure is proposed and crystal orientations have been assigned manually by following the misorientation estimation proposed in [83] (i.e., black and white lines represent boundaries with misorientations above and below 15°, respectively). The specimen in [83] is around 500 µm in diameter, and the best fit between the model and experimental results is obtained for 480 µm. The reduced mobility has been estimated in [83], and linearly evolves during annealing from 0.12 10^{-12} m^2.s^{-1} to 0.02 10^{-12} m^2.s^{-1}. The mobility (3.26) is considered with parameters are listed in table 3.1 excepted $m_{\max}$ that is set so that the average reduced mobility over the sample is 0.06 10^{-12} m^2.s^{-1}. The GB energy is obtained by molecular dynamics computations on pure iron as shown in figure 3.10. The qualitative comparison is presented in figure 3.14

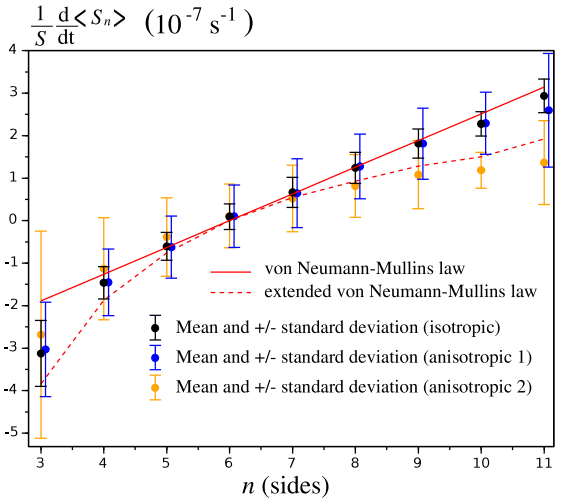

(a) Normalized average area change rate as a function of the number of sides, and comparison with (3.54) and (3.56). Error bars represent more or less one standard deviation. $\mathrm{d}\langle S_n\rangle/\mathrm{d}t$ is the average area change rate and S is the total area of the OT.

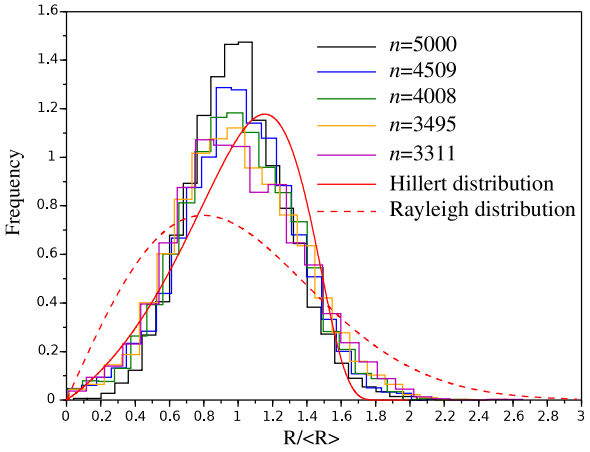

(b) Histograms of equivalent size distribution for different number of grains left in the polycrystal, and comparison with classical Hillert and Rayleigh distributions

Figure 3.12: Validation of basic grain statistics

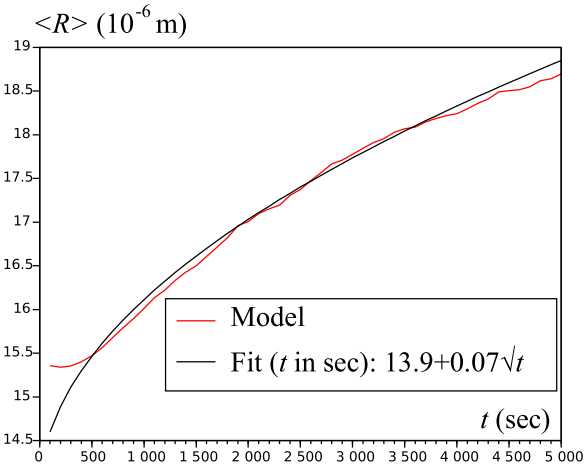

(a) Average grain size $\langle R\rangle$ as a function of time

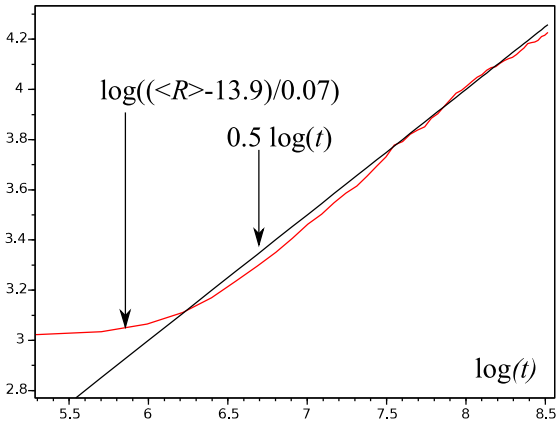

(b) Average grain size $\langle R\rangle$ as a function of time as a log-log plot

Figure 3.13: Validation of grain growth power law $\langle R\rangle \sim t^n$

where grains are colored as in [83] to facilitate the reading. It should also be noted that several neighboring grains have the same crystal orientations to form larger grains. The average equivalent grain radius $\langle R\rangle$ has been extracted from [83] and compared with the model. Good agreement is observed in figure 3.15.

3.7.4 Discussion

In this section, grain statistics are analyzed in more details. The objective is to determine meaningful statistical information that should be considered at the macroscopic scale. In-

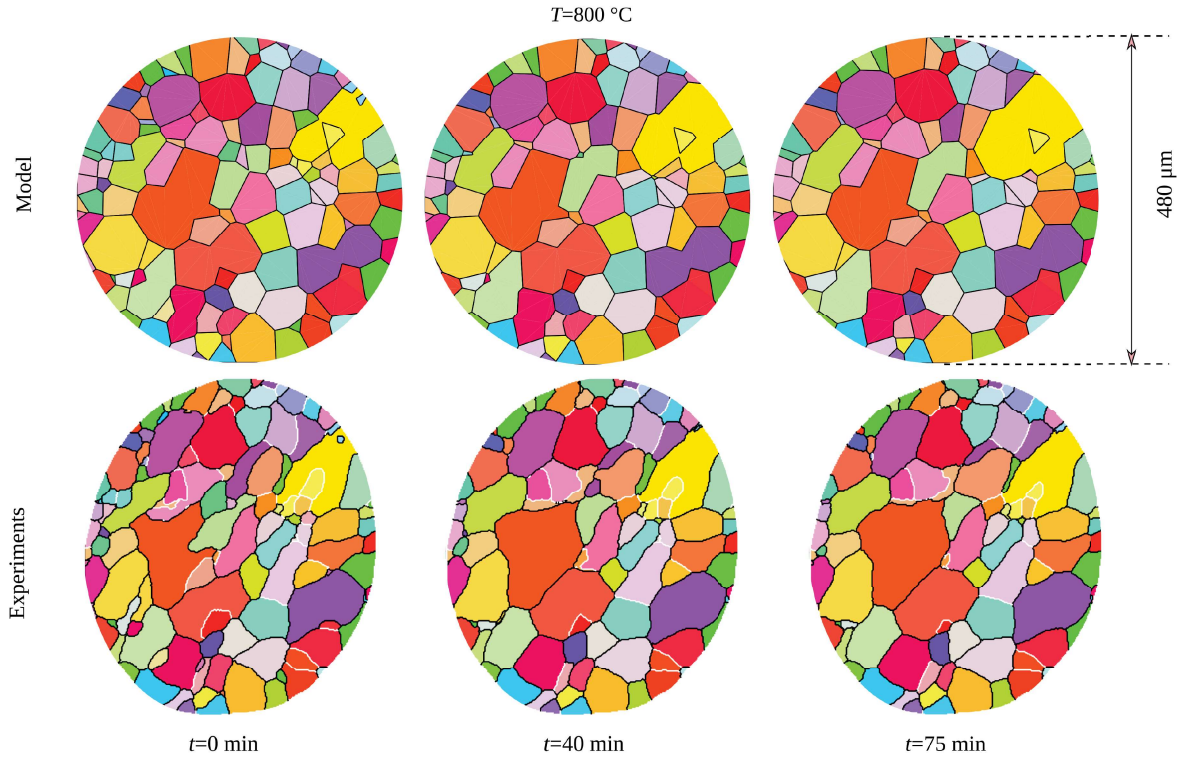

Figure 3.14: Comparison between the model (top) and experiment (bottom).

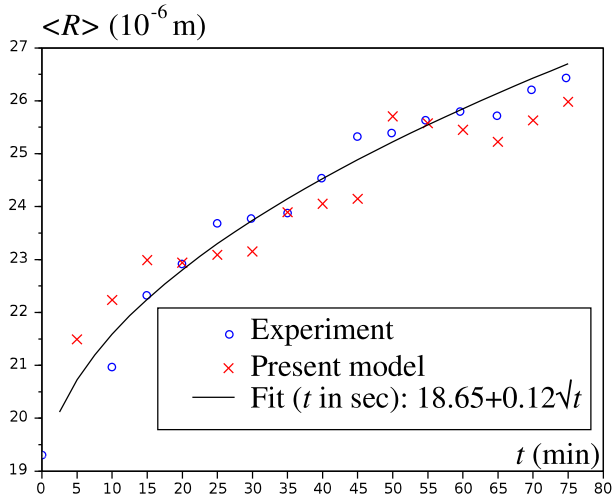

Figure 3.15: Average equivalent radius $\langle R \rangle$, comparison between the proposed model and the experiment.

deed, classical vNM law and Hillert distribution are based only on the average grain size, which is very limited if a specific microstructure is targeted during fabrication or forming processes. In addition, since anisotropic grain growth is considered, BMDs should be captured with sufficient details so that other distributions (e.g., grain size and shape) may be estimated accurately. Four simulations have been performed, with the same initial 2500 grains Voronoi-Laguerre tessellation (see figure 3.16). Crystallographic orientations have

been assigned so that different means and standard deviations of BMDs are obtained, as listed in table 3.2. The evolution is computed according to condition 2 listed in table 3.1. The evolution of mean and standard deviation of grain surface distribution (denoted by $\langle S \rangle$ and σ_S) and BMD (denoted by $\langle \Delta\theta \rangle$ and $\sigma_{\Delta\theta}$) are provided respectively in figures 3.17 and 3.18. Since anisotropic grain growth is considered, the initial mean misorientation affects the growth rate (see figure 3.17a). In addition, the initial mean misorientation also affects the standard deviation of size distribution (see figure 3.17b, comparison between conditions BMD 2 and BMD 3). Thus, grains not only tends to grow in average at different rates according to the mean misorientation, but the distribution also tends to spread at different rates. The evolution of the grain surface distribution also depends on the initial standard deviation of BMD (comparison between conditions BMD 3 and BMD 4). Moreover, significant variations of the mean of BMD are observed in figure 3.18a and strongly depend on the initial standard deviation (see figure 3.18b).

Distributions characterizing microstructures (grain size, shape, orientation, misorientation etc.) constitute a very rich information, which cannot be processed for each material points at the macroscopic scale. However, these distributions may be characterized in a simplified way by a measure of central tendency and statistical dispersion (e.g., mean and standard deviation). Previous examples demonstrate that both mean and standard deviation significantly evolve during anisotropic grain growth. Moreover, couplings between different distributions (e.g., size and misorientation) have been obtained. Thus, the macroscopic model that has to be developed in the subsequent chapter 4, should involve fully coupled state variables characterizing means and standard deviations of different distributions.

Table 3.2: BMD: initial condition

Condition	Mean (°)	Standard deviation (°)
BMD 1	≈ 21	≈ 13.5
BMD 2	≈ 21	≈ 10
BMD 3	≈ 12.5	≈ 10
BMD 4	≈ 12.5	≈ 6.5

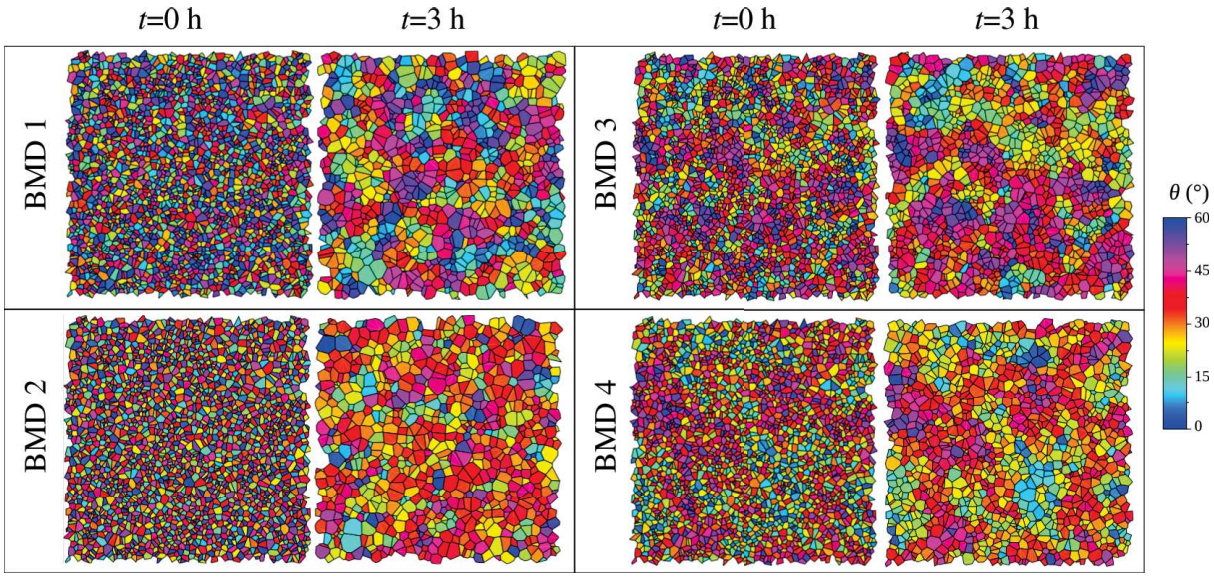

Figure 3.16: Initial OT and after 3 h evolution at $T = 800°$ for all conditions listed in table 3.2

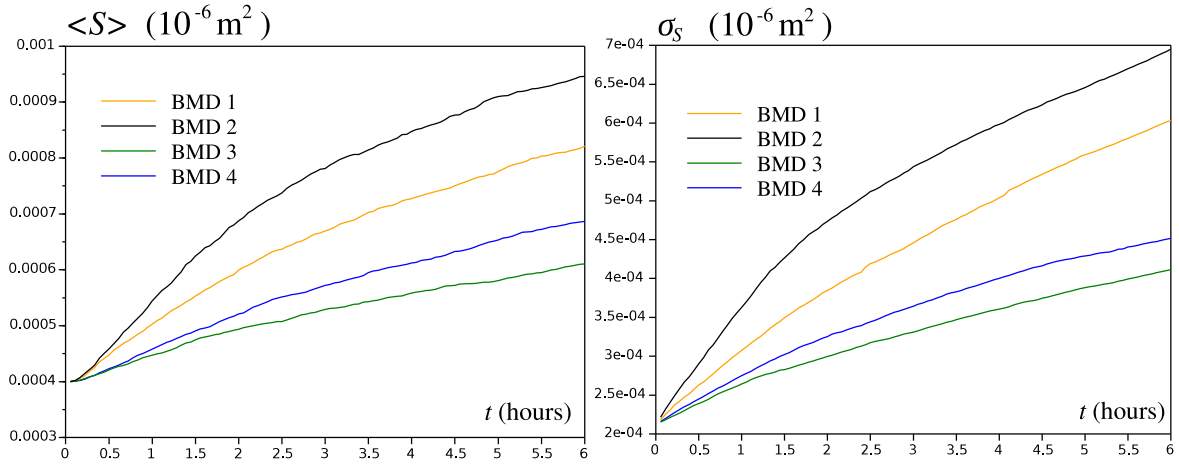

(a) Mean grain surface $\langle S \rangle$

(b) Standard deviation of grain surface σ_S

Figure 3.17: Evolution of grain surface statistics

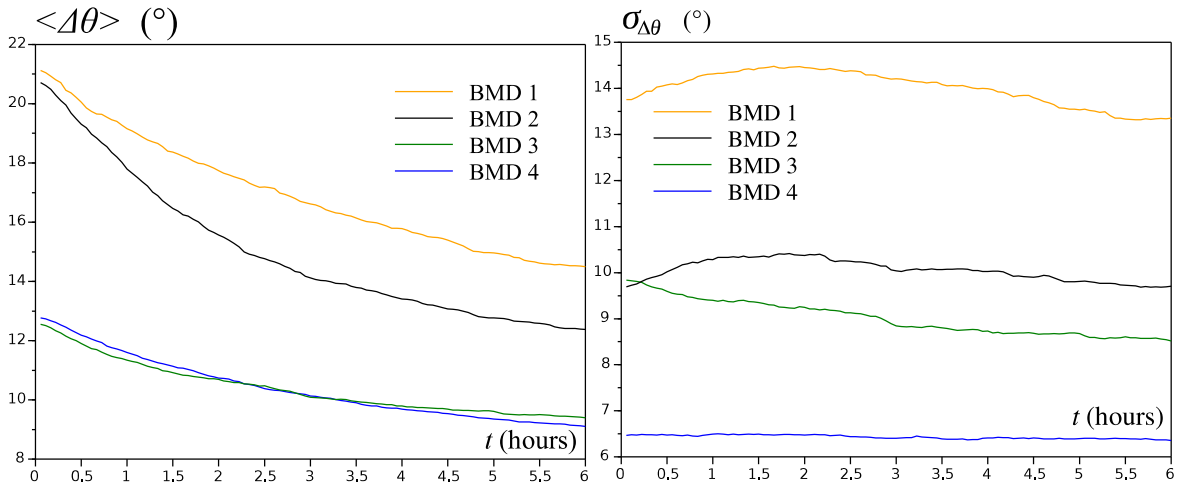

(a) Mean misorientation $\langle \Delta\theta \rangle$

(b) Standard deviation of misorientation $\sigma_{\Delta\theta}$

Figure 3.18: Evolution of misorientation statistics

3.8 Conclusion

An energetic upscaling strategy has been proposed to model grain growth by considering energetic contributions and dissipated power at various scales. This strategy necessitates to establish a large database of computations at the mesoscopic scale in order to feed a macroscopic model whose state variables represent statistical descriptor of the polycrystal. Thus, a fast mesoscopic model based on orientated tessellation updating method has been proposed. The space of possible orientated tessellations can be probed by generating a large number of tessellations with various grain statistics and boundary misorientation distributions. To do so, a procedure to assign crystal orientations has been proposed, and relies on a probabilistic approach enabling to approximately fit targeted boundary misorientation distributions. Representative volume elements have been defined so that boundary conditions may be applied, and mass conservation has been verified to be statistically valid if the number of grains is sufficient. The grain boundary energy has been evaluated by molecular dynamics computations and the dissipated power associated to boundary motion has been evaluated. Thus, the total grain boundary energy and total dissipation in the representative volume element have been calculated as the sum of all grain boundary contributions. The mesoscopic evolution law has been derived by maximizing the total dissipation under the constraint of the first and second laws of thermodynamics and mass balance. The present mesoscopic model has been validated for several conditions by comparing to von Neumann-Mullins law, and classical Hillert distribution. In addition, a good agreement is observed with an annealing experiment conducted on pure iron. The model has been used to analyze the evolution of grain statistics during grain growth, and couplings between means and standard deviations of various distributions (size, misorientation etc.) have been found necessary to capture grain growth at the macroscopic scale. Thus, the present fast mesoscopic model can be intensively used in chapter 4 within framework of the proposed upscaling strategy, and therefore contributes to model detailed grain statistics at very large scales, and tailor microstructures by optimizing fabrication or forming processes.

Chapter 4

Probabilistic macroscopic model identified by Bayesian techniques.

« If people do not believe that mathematics is simple, it is only because they do not realize how complicated life is. »

John von Neumann

Contents

4.1 Introduction

This chapter is adapted from a paper that will be submitted to *Acta Materialia* [92]. We develop the macroscopic model relying on the database of mesoscopic computations, as detailed in chapter 3. The chapter is organized as follows. The reduction of the amount of data for the construction the macroscopic state variables is broached in section 4.2. Primary state variables are defined to explain the GB energy, and an additional state secondary variable is introduced to account for the sensitivity of the mobility tensor to small grains. In section 4.3 the macroscopic evolution laws of the state variables are derived from the mesoscopic model. These macroscopic evolution laws involve to identify several functions that fully depend on the macroscopic state variables. The identification is performed by using a large database of mesoscopic computations whose content is described in section 4.4. The function involved in the energy is deterministic and identified in section 4.5 although the function involved in the mobility is identified in section 4.6, and is probabilistic. Indeed the reduction of the amount of data leads to an epistemic uncertainty that is modeled as a random variable. This epistemic uncertainty is identified by using Bayesian techniques in section 4.7. Results are provided in section 4.8., and additional statistical descriptors of the polycrystalline structure such as the average grain size are estimated as a post-processing. Conclusive remarks are given in section 4.9.

4.2 Macroscopic state variables

4.2.1 Primary state variables

In this section, the macroscopic state variables considered in this work are introduced and discussed. Since the model identification relies on a database that depends on the choice of the macroscopic state variables, it is convenient to define dimensionless state variables so that the database do not depend on the physical length of the tessellations. All physical quantities are explicitly written as a scaling factor in the dimensionless macroscopic evolution law. This choice presents the advantage to obtain a dimensionless database (e.g, the same tessellation is not computed several times depending on its physical length) and to demonstrate analytically in the evolution law the influence of physical length, mobility and surface energy. State variables are not defined arbitrarily as the macroscopic energy should be a function of these variables. However, it is a difficult task to determine suitable variables directly from raw data. Thus, we introduce intuitive state variables and then we demonstrate that such variables are suitable to describe the macroscopic energy.

Each material point of the macroscopic model should represent a polycrystalline structure (RVE) whose energy is the sum of the surface energies carried by the GBs multiplied by their respective length (see chapter 3). Since the surface energy depends on misorientation, we expect the total macroscopic energy at each material point to depend on the statistical distributions of GB lengths and misorientations. However, it is clear that complete statistical distributions constitute a far too rich information to be reasonably processed at each material point of the macroscopic domain. Thus, statistical descriptors (e.g., mean, standard deviation etc.) of length and misorientation distributions should be considered instead of the complete statistical distributions. The successive statistical moments of the misorientation distribution weighted by the GB lengths are chosen. Since GB lengths con-

tinuously tend to zero when a grain disappear, they are used as weights in the statistical moments so that the statistical moments evolve continuously with respect to time. Indeed, otherwise (i.e., without the GB lengths as weights) the statistical moments would be piecewise constant with a discontinuity each time a grain disappear. Thus, the weighted statistical moments obtained from the mesoscopic state read:

$$\mu_k = \sum_{(i,j)\in I_{\mathrm{RVE}}} l_{ij}\Delta\theta_{ij}^k \tag{4.1}$$

where I_{RVE} is the set of grain boundaries in the RVE, l_{ij} the dimensionless length and $\Delta\theta_{ij}$ the misorientation. In addition, $k \in \{0,1,2\}$, indeed as demonstrated in section 4.5 it is sufficient to consider only the three first statistical moments to accurately account for the total energy.

To give a more intuitive interpretation of μ_k ($k \in \{0,1,2\}$), one can refer to L_0 (m) the physical side of the RVE. This parameter enables to determine the average grain size. Thus, for instance μ_0/L_0 is the GB length density (length per unit surface). In addition, the mean of misorientations in the RVE denoted by $\widetilde{\mu}_1$, and the square of the relative standard deviation[1] denoted by $\widetilde{\mu}_2$ read:

$$\begin{cases} \widetilde{\mu}_1 = \dfrac{\mu_1}{\mu_0} \\ \widetilde{\mu}_2 = \dfrac{\mu_2\mu_0}{\mu_1^2} - 1 \end{cases} \tag{4.2}$$

For the sake of clarity, following notations are considered. On the one hand, the statistical moments μ_k ($k \in \{0,1,2\}$) may be computed from the detailed mesoscopic structure by using (4.1). In this case, these variables are denoted by $\underline{\mu}_{\mathrm{meso}} = (\mu_0, \mu_1, \mu_2)$ and correspond to a data reduction with respect to the complete information needed to characterize the OT. Thus, $\underline{\mu}_{\mathrm{meso}}$ is a function of $\underline{\alpha}$ (where $\underline{\alpha} = (\underline{x}, \underline{y}, \underline{w}, \underline{\theta})$ is the mesoscopic state as introduced in chapter 3). The role of $\underline{\mu}_{\mathrm{meso}}$ is twofold: (i) give an overview of mesoscopic evolutions with a limited amount of data, and (ii) provide a tool to define macroscopic state variables within the framework of the upscaling strategy from the mesoscopic scale to the macroscopic scale, as shown in section 4.3.

On the other hand, the overall aim of this chapter is to derive a macroscopic evolution law that do not rely on knowledge of the mesoscopic state. At each material point, only the macroscopic state variables are known, without computing any mesoscopic evolution. The upscaling strategy actually consists in establishing such a macroscopic evolution law. These primary state variables are denoted by $\underline{\mu}_{\mathrm{macro}}$, and correspond to a macroscopic version of $\underline{\mu}_{\mathrm{meso}}$, but exist and can be computed independently from the mesoscopic model, that is to say without using the very definition (4.1). Of course, the identification of the macroscopic model relies on the database of mesoscopic computations, but as soon as this identification is performed, both models are independent. Thus, $\underline{\mu}_{\mathrm{macro}}$ does not refer to a specific RVE, but should represent all possible RVEs sharing the same macroscopic state $\underline{\mu}_{\mathrm{macro}}$.

The quality of the proposed upscaling strategy can be evaluated by comparing (i) the overall behavior of detailed mesoscopic evolutions of specific RVEs, obtained by data reduction in (4.1), and (ii) the corresponding macroscopic evolutions obtained directly from

[1] ratio of the standard deviation over the mean

the macroscopic evolution law. Hence the requirement:

$$\begin{cases} \underline{\mu}_{\text{macro}}(t) \approx \underline{\mu}_{\text{meso}}(t) \\ \dot{\underline{\mu}}_{\text{macro}}(t) \approx \dot{\underline{\mu}}_{\text{meso}}(t) \end{cases} \tag{4.3}$$

As detailed in the following, the loss of information (due to the fact that several different mesoscopic states can share the same macroscopic state) require to consider the macroscopic evolution law within a probabilistic framework. Thus, the latter condition for the upscaling strategy to be reliable (4.3) should be understood in a probabilistic sense. Intuitively, that is to say that the for a particular RVE, the mesoscopic evolution summarized by $\underline{\mu}_{\text{meso}}(t)$ should lie in the zone defined by the point-wise dispersion around the mean macroscopic evolution $\langle \underline{\mu}_{\text{macro}}(t) \rangle$, where $\underline{\mu}_{\text{macro}}$ is a random variable. Alternatively, considering a large number of different RVEs initially sharing the same overall state $\underline{\mu}_{\text{meso}}(t=0)$, one can compute the empirical mean and standard deviation as a function of time, and compare them to the mean and standard deviation as a function of time of the macroscopic probabilistic evolution.

Consistently with previous notations, for any given quantity denoted by Q, Q_{meso} refers to the quantity Q computed from the mesoscopic state $\underline{\alpha} = (\underline{x}, \underline{y}, \underline{w}, \underline{\theta})$, although Q_{macro} refers to the quantity Q computed from the macroscopic evolution law, without knowledge of the mesoscopic state, hence Q_{macro} only depends on $\underline{\mu}_{\text{macro}}$.

4.2.2 Secondary state variable

In addition, even though it is demonstrated in section 4.5 that the total energy of an RVE is completely determined by $\underline{\mu}_{\text{meso}}$, it is shown in section 4.6 that the dissipated power requires a probabilistic framework and necessitates the introduction of an additional state variable. Indeed, at the mesoscopic scale the dissipated power depends on a second order mobility tensor $\underline{\underline{M}}_{\text{meso}}$ defined in (3.51) in section 3.6. When a grain i tends to vanish i.e., $S_i \to 0$ (where S_i is the dimensionless surface of the grain), the corresponding grain boundaries vanish, i.e., $l_{ij} \to 0$ (with j denoting the neighboring grains). Since the mobility tensor $\underline{\underline{M}}_{\text{meso}}$ includes the inverse of a tensor that linearly depends on the GB lengths, when a grain i tends to vanish the corresponding components in the mobility tensor $\underline{\underline{M}}_{\text{meso}}$ diverge. This could be interpreted as a numerical conditioning issue. However, this behavior actually reflects an instability of small grains that can freely disappear with negligible dissipation cost (i.e., very high mobility). This sensitivity of the mobility tensor to small grains also arises at the macroscopic scale as discussed in section 4.6. Thus, an additional variable should be added to capture this behavior. To that end, the following variable is introduced:

$$\eta_{\text{meso}} = -\sum_{k=1}^{n} \log(S_k) \tag{4.4}$$

where S_k are the dimensionless surfaces in the RVE. At first glance this variable may seem arbitrary. However it is clear that the more small grains the RVE contains and the higher η_{meso} will be. Unlike $\underline{\mu}_{\text{meso}}$, the variable η_{meso} is not continuous with respect to time as it diverges each time a grain disappear. This is illustrated in figure 4.1a, where $0.5\eta_{\text{meso}}$ is presented as a function of time with a refined time discretization in order to detect discontinuities (the time step is 10 s). It is clear that $0.5\eta_{\text{meso}}$ is fairly well correlated with

the evolution of the number of grain boundaries n_{GB}. This aspect is demonstrated more systematically in figure 4.1b where n_{GB} is presented as a function of $0.5\eta_{\text{meso}}$ for the tessellations extracted from the database presented in section 4.4. As for the primary state

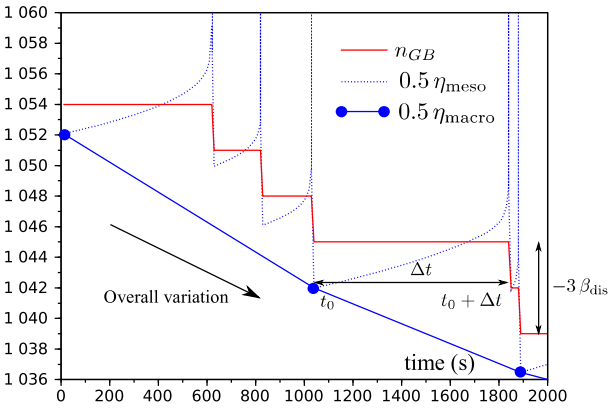

(a) Evolution of n_{GB} and $0.5\eta_{\text{meso}}$ with a refined time discretization, and macroscopic counterpart.

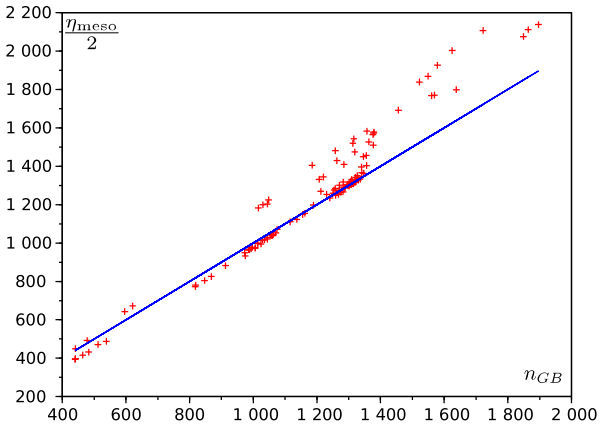

(b) n_{GB} *vs* $0.5\eta_{\text{meso}}$ for the tessellations extracted from the database.

Figure 4.1: Approximation of n_{GB} by $0.5\eta_{\text{meso}}$.

variables $\underline{\mu}_{\text{macro}}$, a secondary state variable η_{macro} should be determined by establishing a macroscopic evolution law that do not refer to the mesoscopic scale and such as:

$$\eta_{\text{macro}}(t) \approx \eta_{\text{meso}}(t) \tag{4.5}$$

However, a difficulty arises with the fact that η_{meso} is discontinuous. Indeed, the time derivative $\dot{\eta}_{\text{meso}}$ is always positive although the overall variation with respect to time is negative (see. figure 4.1a), which implies that:

$$\dot{\eta}_{\text{macro}}(t) \neq \dot{\eta}_{\text{meso}}(t) \tag{4.6}$$

To overcome this difficulty, a smooth approximation of $\eta_{\text{meso}}(t)$ is sought by considering a larger time scale avoiding the jumps of $\eta_{\text{meso}}(t)$ as shown in figure 4.1a. This continuous approximation is obtained by considering the overall variation of n_{GB} during a finite time interval. More precisely the following idealized situation is considered. During a mesoscopic evolution, consider an instant t_0 belonging to the macroscopic time scale (see figure 4.1a). In particular small grains sizes are not negligible as η_{meso} is stable. Consider a grain i the next grain to disappear. This grain i is much smaller than the others, and reduces in size. The time needed for the grain i to disappear is denoted by Δt (see. figure 4.1a). A crude approximation of Δt is determined by considering a first order Taylor expansion of the dimensionless grain radius $\sqrt{S_i}/\sqrt{\pi}$, namely:

$$\sqrt{S_i(t_0+\Delta t)} \approx \sqrt{S_i(t_0)} + \frac{\dot{S}_i(t_0)}{2\sqrt{S_i(t_0)}}\Delta t = 0 \tag{4.7}$$

Hence:

$$\Delta t \approx -2\frac{S_i(t_0)}{\dot{S}_i(t_0)} \tag{4.8}$$

It should be noted that the choice of $\sqrt{S_i}$ instead of S_i to estimate the time needed for the grain to disappear is not arbitrary: the equivalent radius evolves more linearly than the grain surface.

The vanishing grain i is very likely to be triangular, therefore three GBs disappear. In addition, since n_{GB} and $0.5\eta_{\text{meso}}$ share the same overall evolution, we impose that the time derivative of $0.5\dot{\eta}_{\text{macro}}$ is equal to the overall variation of n_{GB} over Δt. However, it can be observed in figure 4.1a that when a grain i disappears at $t_0 + \Delta t$, several other grains may disappear almost immediately after that. This shorter time scale cannot be considered at the macroscopic scale as a smooth representation of n_{GB} is sought. To overcome this difficulty, consider β_{dis} the average number of grains that almost immediately disappear after the grain i, hence:

$$0.5\dot{\eta}_{\text{macro}} = \frac{n_{GB}(t_0 + \Delta t) - n_{GB}(t_0)}{\Delta t} = -\frac{3\beta_{\text{dis}}}{\Delta t} \tag{4.9}$$

Since at time t_0 the only grain that is much smaller than the other is the grain i (i.e., $1/S_i(t_0) \gg S_k(t_0)$ for $k \neq i$), the time derivative of η_{meso} defined in (4.4) can be approximated as follows:

$$\dot{\eta}_{\text{meso}}(t_0) = -\sum_{k=1}^{n} \frac{\dot{S}_k(t_0)}{S_k(t_0)} \approx -\beta_{\text{dis}} \frac{\dot{S}_i(t_0)}{S_i(t_0)} \tag{4.10}$$

Thus, by using (4.8), (4.9) and (4.10) one obtains:

$$\dot{\eta}_{\text{macro}} \approx -3\beta_{\text{dis}}\dot{\eta}_{\text{meso}}(t_0) \tag{4.11}$$

Since the previous analysis is very simplified, the factor $-3\beta_{\text{dis}}$ in (4.11) is not fully determined as β_{dis} is unknown. A specific analysis could be carried out to identify β_{dis} as a function of η_{meso} (and potentially additional morphological variables). However, this aspect has not been broached in this work. Instead β_{dis} is approximated in a phenomenological way, that is to say without rigorous derivation from the mesoscopic scale, as for the rest of the model. The very definition of η_{meso} (4.4) shows that β_{dis} is an increasing function of η_{meso}. Moreover, $\beta_{\text{dis}} = 1$ when η_{meso} is under a certain threshold. Indeed, when a grain i is disappearing, the minimum number of grains that can disappear is one. These remarks lead to consider a power law with a threshold, and by replacing η_{meso} by its macroscopic counterpart η_{macro}:

$$\beta_{\text{dis}} = \begin{cases} \left(\dfrac{0.5\eta_{\text{macro}}}{\beta_0}\right)^{\delta} & 0.5\eta_{\text{macro}} \geq \beta_0 \\ 1 & 0.5\eta_{\text{macro}} \leq \beta_0 \end{cases} \tag{4.12}$$

where $\delta = 3$ and $\beta_0 = 1000$ are identified from numerical results presented in section 4.8 so that n_{GB} is well captured by $0.5\eta_{\text{macro}}$. It should be noted that the other quantities arising in the macroscopic evolution laws derived in section 4.3 are not identified in phenomenological way as for β_{dis}, but in a more theoretical and systematic way as detailed in sections 4.5 and 4.6. The simplified phenomenological identification of β_{dis} is an exception that is proposed to avoid technicalities. The choice of β_{dis} has a significant impact on η_{macro}, however since μ_{macro} only slightly depends on η_{macro}, the choice of β_{dis} has limited impact on μ_{macro}. Thus, this phenomenological identification seems sufficient as the whole model is not conditioned to it.

In addition, the latter relation (4.11) shows that to overcome the difficulty due to the discontinuity of η_{meso}, the database should avoid tessellations with very small grains, whose sizes are negligible. Indeed, a smooth macroscopic secondary state variable is derived by using $\dot{\eta}_{\text{meso}}(t_0)$, which should be finite (i.e., without grains such as $S_i \approx 0$).

4.3 Macroscopic evolution laws

4.3.1 Primary state variables evolution law

In this section the macroscopic evolution law is derived. Some results related to the database of mesoscopic computations and presented in following sections are required in this section. Nevertheless, the derivation of the macroscopic evolution law is derived first as it enables us to introduce the mathematical quantities to compute in the database.

The mesoscopic evolution law (3.52), has been derived in chapter 3 from thermodynamical principles. For the sake of clarity, this law is recalled here by using the previously discussed notations. Thus, considering a mesoscopic structure the following evolution law holds:

$$\underline{\dot{w}}_{\text{meso}} = -\frac{m(T)}{L_0^3}\underline{\underline{M}}_{\text{meso}} \cdot \frac{\partial \mathscr{E}_{\text{meso}}}{\partial \underline{w}} \tag{4.13}$$

where $\underline{w}_{\text{meso}}$ are the weights of the OT, $\mathscr{E}_{\text{meso}}$ is the total energy per unit depth in the RVE, $m(T)$ is a scalar mobility that depends on temperature, and $\underline{\underline{M}}_{\text{meso}}$ is the dimensionless mobility second order tensor of size $n \times n$ depending on the mesoscopic state $\underline{\alpha}$. It should be noted that $\underline{\underline{M}}_{\text{meso}}$ depends on the choice of the mobility as a function of misorientation at the scale of GBs. In the following the database and then the macroscopic model are based on the mobility function (3.26) introduced in chapter 3.

Since $\underline{\mu}_{\text{meso}}$ depends on the mesoscopic state the following derivation rule holds:

$$\underline{\dot{\mu}}_{\text{meso}} = \frac{\partial \underline{\mu}_{\text{meso}}}{\partial \underline{w}} \cdot \underline{\dot{w}}_{\text{meso}} \tag{4.14}$$

where $\partial \underline{\mu}_{\text{meso}} / \partial \underline{w}$ is a dimensionless second order tensor of size $3 \times n$, which can be computed analytically (see. A). Hence from (4.13) and (4.14):

$$\underline{\dot{\mu}}_{\text{meso}} = -\frac{m(T)}{L_0^3}\frac{\partial \underline{\mu}_{\text{meso}}}{\partial \underline{w}} \cdot \underline{\underline{M}}_{\text{meso}} \cdot \frac{\partial \mathscr{E}_{\text{meso}}}{\partial \underline{w}} \tag{4.15}$$

In addition, in section 4.5 the analysis of the database of mesoscopic computations shows that the total mesoscopic energy per unit depth denoted by $\mathscr{E}_{\text{meso}}$ can be very accurately approximated by a deterministic function $f(\underline{\mu}_{\text{meso}})$:

$$\mathscr{E}_{\text{meso}}(T, \underline{\alpha}) \approx L_0 \gamma_S \frac{G(T)}{G(0)} f(\mu_{\text{meso}}) \tag{4.16}$$

where $\gamma_S = 1$ J.m^{-2}, $G(T)$ is the temperature dependent shear modulus that captures the temperature dependance of the GB energy (see. chapter 3), and f is an analytic function

determined in (4.39) in section 4.5. Hence, from (3.52), (4.15) and (4.16) one obtains the overall mesoscopic evolution law:

$$\underline{\dot{\mu}}_{\text{meso}} = -\left(\frac{\gamma_S\, m(T)}{L_0^2}\frac{G(T)}{G(0)}\right)\left[\left(\frac{\partial \underline{\mu}_{\text{meso}}}{\partial \underline{w}}\right)\cdot \underline{\underline{M}}_{\text{meso}}\cdot\left(\frac{\partial \underline{\mu}_{\text{meso}}}{\partial \underline{w}}\right)^T\right]\cdot\frac{\partial f(\underline{\mu}_{\text{meso}})}{\partial \underline{\mu}} \tag{4.17}$$

On the basis of (4.17) the following dimensionless second order tensor of size 3×3 (called mobility tensor) is introduced:

$$\underline{\underline{\Gamma}}_{\text{meso}} = \frac{\partial \underline{\mu}}{\partial \underline{w}}\cdot \underline{\underline{M}}_{\text{meso}}\cdot\left(\frac{\partial \underline{\mu}}{\partial \underline{w}}\right)^T \tag{4.18}$$

Since the upscaling strategy relies on the objective that the macroscopic state variables $\underline{\mu}_{\text{macro}}$ provide a good approximation of the mesoscopic overall state $\underline{\mu}_{\text{meso}}$ (see. (4.3)), the macroscopic energy is defined as the same deterministic function f but evaluated in $\underline{\mu}_{\text{macro}}$, that is to say:

$$\mathscr{E}_{\text{macro}}(T,\underline{\mu}_{\text{macro}}) = L_0\gamma_S\frac{G(T)}{G(0)}f(\mu_{\text{macro}}) \approx \mathscr{E}_{\text{meso}}(T,\underline{\alpha}) \tag{4.19}$$

For the energy, the upscaling strategy reduces to the identification of γ_S and the deterministic dimensionless function f. In addition, the upscaling strategy also consists in approximating the dimensionless mesoscopic mobility tensor $\underline{\underline{\Gamma}}_{\text{meso}}$ by a macroscopic tensor $\underline{\underline{\Gamma}}_{\text{macro}}$ defined in (4.72) that only depends on the macroscopic state without any knowledge of the detailed mesoscopic state:

$$\underline{\underline{\Gamma}}_{\text{macro}} \approx \underline{\underline{\Gamma}}_{\text{meso}} \tag{4.20}$$

In addition, it is shown in section 4.6 that $\underline{\underline{\Gamma}}_{\text{meso}}$ depends on the secondary variable η_{meso} defined in (4.4) and $\underline{\underline{\Gamma}}_{\text{macro}}$ requires a probabilistic framework and depends on the secondary state variable η_{macro}. Thus, by using (4.3), (4.19), (4.20) and (4.5) into (4.17), the macroscopic evolution law of the primary state variables is obtained:

$$\underline{\dot{\mu}}_{\text{macro}} = -\left(\frac{\gamma_S\, m(T)}{L_0^2}\frac{G(T)}{G(0)}\right)\underline{\underline{\Gamma}}_{\text{macro}}\left(\underline{\mu}_{\text{macro}},\eta_{\text{macro}}\right)\cdot\frac{\partial f(\underline{\mu}_{\text{macro}})}{\partial \underline{\mu}} \tag{4.21}$$

where $\partial f(\mu_{\text{macro}})/\partial\underline{\mu}$ can be interpreted as the dimensionless macroscopic driving force.

4.3.2 Secondary state variable evolution law

Of course, the secondary state variable η_M also needs a macroscopic evolution law in order to update $\underline{\underline{\Gamma}}_{\text{macro}}\left(\underline{\mu}_{\text{macro}},\eta_{\text{macro}}\right)$ at each time step. Since surfaces S_k depend on the mesoscopic state the following derivation rule holds:

$$\dot{\eta}_{\text{meso}} = -\sum_{k=1}^{n}\frac{\dot{S}_k}{S_k} \tag{4.22}$$

where:

$$\dot{S}_k = \frac{\partial S_k}{\partial \underline{w}}\cdot \dot{w}_{\text{meso}} \tag{4.23}$$

And by using (4.13) one obtains:

$$\dot{\eta}_{\text{meso}} = \frac{m(T)}{L_0^3}\left(\sum_{k=1}^{n}\frac{1}{S_k}\frac{\partial S_k}{\partial \underline{w}}\right)\cdot \underline{\underline{M}}_{\text{meso}}\cdot\frac{\partial \mathscr{E}_{\text{meso}}}{\partial \underline{w}} \tag{4.24}$$

Hence, from (3.52), (4.24) and (4.16) one obtains the overall mesoscopic evolution law:

$$\dot{\eta}_{\text{meso}} = \left(\frac{\gamma_S\, m(T)}{L_0^2}\frac{G(T)}{G(0)}\right)\left[\left(\sum_{k=1}^{n}\frac{1}{S_k}\frac{\partial S_k}{\partial \underline{w}}\right)\cdot \underline{\underline{M}}_{\text{meso}}\cdot\left(\frac{\partial \underline{\mu}_{\text{meso}}}{\partial \underline{w}}\right)^T\right]\cdot\frac{\partial f(\underline{\mu}_{\text{meso}})}{\partial \underline{\mu}} \tag{4.25}$$

On the basis of (4.25) the following dimensionless vector of size 3 is introduced:

$$\underline{\Lambda}_{\text{meso}} = \left(\sum_{k=1}^{n}\frac{1}{S_k}\frac{\partial S_k}{\partial \underline{w}}\right)\cdot \underline{\underline{M}}_{\text{meso}}\cdot\left(\frac{\partial \underline{\mu}_{\text{meso}}}{\partial \underline{w}}\right)^T \tag{4.26}$$

With the same reasoning as before, the upscaling strategy consists in approximating the dimensionless mesoscopic vector $\underline{\Lambda}_{\text{meso}}$ by a macroscopic vector $\underline{\Lambda}_{\text{macro}}$ defined in (4.72) that only depends on the macroscopic state without any knowledge of the detailed mesoscopic state:

$$\underline{\Lambda}_{\text{macro}} \approx \underline{\Lambda}_{\text{meso}} \tag{4.27}$$

Thus, thus macroscopic evolution law of the secondary state variable is obtained:

$$\dot{\eta}_{\text{macro}} = -3\,\beta_{\text{dis}}(\eta_{\text{macro}})\left(\frac{\gamma_S\, m(T)}{L_0^2}\frac{G(T)}{G(0)}\right)\underline{\Lambda}_{\text{macro}}\left(\underline{\mu}_{\text{macro}},\eta_{\text{macro}}\right)\cdot\frac{\partial f(\underline{\mu}_{\text{macro}})}{\partial \underline{\mu}} \tag{4.28}$$

where the factor $-3\,\beta_{\text{dis}}$ is due to (4.11).

All terms involved in (4.21) and (4.28) are defined from the macroscopic state, and do not refer to the RVE. However, L_0 explicitly arises in (4.21) and (4.28), which shows the influence of the physical grain size on grain growth as already discussed in chapter 3. Of course, it seems that L_0 refers to the RVE in (4.21) and (4.28) and that state variables could have been defined as densities per unit area instead of being defined as dimensionless quantities in order to discard L_0 from (4.21) and (4.28). Nevertheless, L_0 can be seen as a scaling parameter fixing the average grain size, which is a macroscopic quantity. In addition to the primary state variables $\underline{\mu}_{\text{macro}}$ several other interesting macroscopic quantities such as the average grain size or the average GB length can be computed as a post-processing of the macroscopic evolution law, as shown in section 4.8.3.

4.4 Database content

In this section the database of mesoscopic computations is presented. As discussed in chapter 1, the mesoscopic model based on OTUM has mainly been developed to be intensively used in order to construct a large database that probes the space of OTs. The database is analyzed to identify the energy $\mathscr{E}_{\text{meso}}$ in (4.16), the mobility tensor $\underline{\underline{\Gamma}}_{\text{meso}}$ in (4.18), and the vector $\underline{\Lambda}_{\text{macro}}$ in (4.26).

The free software NEPER [29] is used to generate Voronoi-Laguerre tessellations with various morphological statistics. In addition, the probabilistic procedure described in section 3.3 enables us to obtain various OTs with morphological and crystallographic textures.

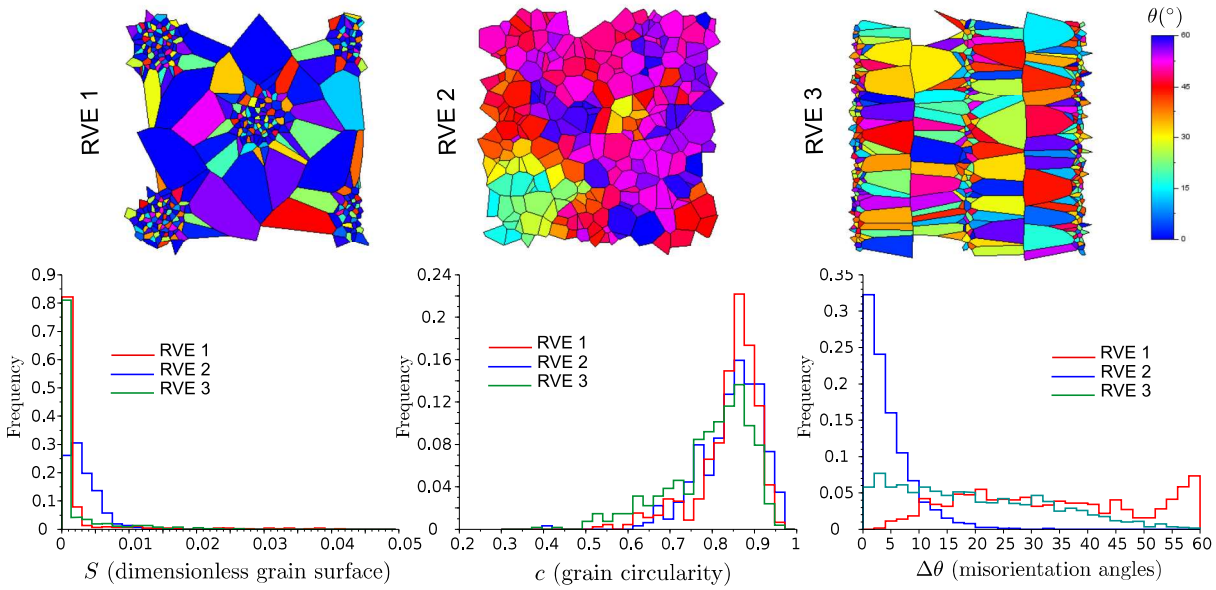

Figure 4.2: Three different examples of OTs considered for the database, with histograms of grain size, grain circularity, and BMD.

In figure 4.2 three examples of RVEs are presented with grain size and circularity distribution as well as boundary misorientation distribution (BMD).

The database that has been used in this work does not include results from mesoscopic evolutions, which would provide successions of OTs that could be included in the database. Instead a more *static* approach has been chosen, the database is constructed from $N_{\text{tess}} = 121$ different tessellations, each of which is assigned with $N_{\text{ori}} = 162$ different crystal orientation fields, leading to a total of $N_{\text{data}} = 19.602$ OTs. Crystal orientation fields are generated as follows. First, a beta probability density $\mathscr{B}(\alpha,\beta)$ has been used with $(\alpha,\beta) \in \{1,\cdots,9\}^2$ (i.e., 81 crystal orientation fields), then a normal probability density $\mathscr{N}(\mu,\sigma)$ has been used with μ and σ describing a homogeneous discretization (with 9 steps) of intervals $[15,45]$ and $[5,30]$ respectively (i.e., 81 crystal orientation fields). Of course, several draws of each probability density function involved in the orientation field assignment procedure could be generated instead of only one to enrich the database.

This *static* approach has been chosen to optimize the computation time, as the succession of OTs obtained during a mesoscopic evolution provides rather similar OTs, although the proposed *static* approach enables to probe more efficiently the large space of OTs by selecting very different OTs. But of course, a more *dynamic* approach can also be used to complete the database. When running the mesoscopic code for a given RVE, the intermediate states at each time step can be stored along with the different elements needed for the database, making easy to enrich the database automatically each time the mesoscopic code is used.

The database is constructed on the basis of RVEs obtained from the OTs. Indeed, as discussed in chapter 3, boundary conditions in the mesoscopic model are defined by considering a group of connected grains in the OT that do not belong to the edge of the OT.

Even though the database is dimensionless and do not depend for instance on L_0, it should be noted that the database obviously depends on the choice of the local GB energy (3.16) and mobility (3.26) as a function of misorientation at the scale of the grain boundary.

This choice has been discussed in section 3.5 in chapter 3.

An extract of the database is given in table 4.1 where i_d (with $1 \leq i_d \leq N_{\text{tess}}$) is the index of the Voronoi-Laguerre tessellation, k (with $1 \leq k \leq N_{\text{data}}$) is the index of each entry in the database, and E_{meso} is the dimensionless GB energy at 0 K:

$$E_{\text{meso}} = \frac{\mathscr{E}_{\text{meso}}(T=0)}{L_0 \gamma_S} \tag{4.29}$$

The complete database for pure iron that has been constructed in this work is available as a supplement to this PhD thesis at the following link: `http://site`.

Table 4.1: Extract of the database of mesoscopic computations for pure iron.

k	i_d	n	n_{GB}	$\underline{\mu}_{\text{meso}}$			E_{meso}	$\underline{\underline{\Gamma}}_{\text{meso}}$						$\underline{\Lambda}_{\text{meso}}$			η_{meso}
				μ_0	μ_1	μ_2		Γ_{11}	Γ_{22}	Γ_{33}	Γ_{12}	Γ_{13}	Γ_{23}	Λ_1	Λ_2	Λ_3	
1	1	397	1268	39	8.7	2.4	26.3	1593	387	77	475	153	166	37961	10592	3269	2505
2	1	397	1268	39	8.9	2.7	26.0	1903	521	133	410	116	251	48056	11834	3819	2505
3	1	397	1268	39	9.4	3.1	26.1	1892	550	151	554	190	269	47833	13775	4376	2505
4	1	397	1268	39	10.2	3.8	26.6	1951	969	387	662	312	587	50740	12303	4950	2505
5	1	397	1268	39	9.9	3.7	26.1	1947	1017	349	823	355	561	47579	17698	7287	2505
6	1	397	1268	39	11.1	4.6	27.1	1919	949	420	711	324	595	46292	15144	5529	2505
7	1	397	1268	39	11.5	4.9	27.4	2436	1230	633	996	463	826	60631	20881	8602	2505
8	1	397	1268	39	11.4	5.0	26.9	2445	1371	699	974	427	911	63145	22542	7226	2505
9	1	397	1268	39	11.7	5.3	26.8	2300	1600	911	991	504	1150	66895	36583	20213	2505
10	1	397	1268	39	10.5	3.5	28.7	2686	850	264	806	291	456	66612	19521	6991	2505
11	1	397	1268	39	10.6	3.7	28.1	2198	751	264	585	200	422	55423	14248	4402	2505
12	1	397	1268	39	10.8	4.0	27.8	2430	1104	406	910	381	633	62014	19663	8526	2505
13	1	397	1268	39	11.0	4.4	27.3	2414	1035	445	883	383	640	61547	22430	9771	2505
⋮	⋮	⋮	⋮	⋮	⋮	⋮	⋮	⋮	⋮	⋮	⋮	⋮	⋮	⋮	⋮	⋮	⋮

4.5 Identification of the macroscopic free energy

In this section, the macroscopic GB energy per unit depth $\mathscr{E}_{\text{macro}}$ is identified on the basis of $\mathscr{E}_{\text{meso}}$ computed for all the OTs listed in the database. The upscaling strategy is conducted in two steps. (i) The first step consists in determining an analytic expression for $\mathscr{E}_{\text{meso}}$ as a function of $\underline{\mu}_{\text{meso}}$ by considering small angle misorientations, which enables to use the analytical local GB energy function proposed by Read & Shockley [1] and a Taylor expansion of the total energy per unit depth in the RVE. (ii) The second step consists in identifying the unknown coefficients involved in the analytic expression exhibited for small angle misorientations (step (i)) by a simple minimization process (least-squares method) between the energy stored in the database and predictions of the analytic expression. This identification procedure leads to a macroscopic energy function that fit the data almost perfectly, which strongly supports the idea of modeling the macroscopic energy $\mathscr{E}_{\text{macro}}$ as a deterministic function of $\underline{\mu}_{\text{macro}}$.

4.5.1 Analytic expression for the grain boundary energy

The total mesoscopic GB energy defined in chapter 3 is recalled here for the sake of clarity:

$$\mathscr{E}_{\text{meso}}(T, \underline{\alpha}) = L_0 \frac{G(T)}{G(0)} \sum_{(i,j) \in I_{\text{RVE}}} l_{ij} \gamma(0, \Delta\theta_{ij}) \tag{4.30}$$

where $\gamma(0,\Delta\theta_{ij})$ is the local anisotropic GB energy per unit area at 0 K. If small angle misorientations are considered the Read & Shockley formula [1] is accurate, and presents the advantage to deal with simple analytic expressions, and then:

$$\gamma(0,\Delta\theta) = \gamma_S \kappa_1 \Delta\theta \left(\kappa_2 - \log(\Delta\theta)\right) \tag{4.31}$$

where $\gamma_S = 1$ J.m^{-2}, κ_1, κ_2 are dimensionless parameters. Hence:

$$\mathscr{E}_{\text{meso}}(T,\underline{\alpha}) = L_0 \frac{G(T)}{G(0)} \gamma_S \kappa_1 \sum_{(i,j)\in I_{\text{RVE}}} l_{ij} \Delta\theta_{ij} \left(\kappa_2 - \log\left(\Delta\theta_{ij}\right)\right) \tag{4.32}$$

Moreover, ϵ_{ij} denotes the deviation of the misorientation $\Delta\theta_{ij}$ from the mean misorientation $\widetilde{\mu}_1$ defined in (4.2), hence:

$$\Delta\theta_{ij} = \widetilde{\mu}_1 + \epsilon_{ij} \tag{4.33}$$

Thus, combining (4.32) and (4.33) one obtains:

$$\mathscr{E}_{\text{meso}}(T,\underline{\alpha}) = L_0 \frac{G(T)}{G(0)} \gamma_S \kappa_1 \sum_{(i,j)\in I_{\text{RVE}}} l_{ij} \left(\widetilde{\mu}_1 + \epsilon_{ij}\right) \left(\kappa_2 - \log\left(\widetilde{\mu}_1\right) - \log\left(1 + \frac{\epsilon_{ij}}{\widetilde{\mu}_1}\right)\right) \tag{4.34}$$

By considering that the deviations ϵ_{ij} are small compared to $\widetilde{\mu}_1$ (i.e., $\epsilon_{ij}/\widetilde{\mu}_1 \ll 1$), the Taylor expansion at the second order in ϵ_{ij} reads:

$$\mathscr{E}_{\text{meso}}(T,\underline{\alpha}) = L_0 \frac{G(T)}{G(0)} \gamma_S \kappa_1 \sum_{(i,j)\in I_{\text{RVE}}} l_{ij} \left(\widetilde{\mu}_1 + \epsilon_{ij}\right) \left(\kappa_2 - \log\left(\widetilde{\mu}_1\right) - \frac{\epsilon_{ij}}{\widetilde{\mu}_1} + \frac{\epsilon_{ij}^2}{2\widetilde{\mu}_1^2} + o\left(\epsilon_{ij}^2\right)\right) \tag{4.35}$$

Moreover, using the definition (4.33), the following equations can be easily verified:

$$\begin{cases} \displaystyle\sum_{(i,j)\in I_{\text{RVE}}} l_{ij}\epsilon_{ij} = 0 \\ \displaystyle\sum_{(i,j)\in I_{\text{RVE}}} l_{ij}\epsilon_{ij}^2 = \mu_2 - \frac{\mu_1^2}{\mu_0} \end{cases} \tag{4.36}$$

Hence:

$$\mathscr{E}_{\text{meso}}(T,\underline{\alpha}) \approx L_0 \frac{G(T)}{G(0)} \gamma_S \kappa_1 \mu_0 \widetilde{\mu}_1 \left(\kappa_2 - \log\left(\widetilde{\mu}_1\right) - \frac{\mu_2 \mu_0}{2\mu_1^2}\right) \tag{4.37}$$

By using the definition of the relative standard deviation introduced in (4.2), the total GB energy for small angle misorientations can approximated as follows:

$$\mathscr{E}_{\text{meso}}(T,\underline{\alpha}) \approx L_0 \frac{G(T)}{G(0)} \gamma_S f(\underline{\mu}_{\text{meso}}) \tag{4.38}$$

where the dimensionless function f reads:

$$f(\mu_0,\mu_1,\mu_2) = \kappa_1 \mu_0 \widetilde{\mu}_1 \left(\kappa_2 - \log\left(\widetilde{\mu}_1\right) - \frac{1}{2}\left(\widetilde{\mu}_2 + 1\right)\right) \tag{4.39}$$

The simple analytic expression (4.38) is used to fit the energy stored in the database as a function of $\underline{\mu}_{\text{meso}}$. The two coefficients κ_1 and κ_2 need to be identified.

4.5.2 Identification of the unknown coefficients

As introduced in chapter 3, the local GB energy used in the model is not the Read & Shockley formula [1] but an analytic function (3.16) proposed by Wolf [88], which enables to interpolated molecular dynamics computations. However, for low angle misorientations the interpolation function matches the Read & Shockley formula and the analysis presented in section 4.5.1 remains valid. In addition, even though the analysis has been conducted for very small angle misorientations, the obtained analytic function f in (4.39) is used as an educated guess to interpolate the energy in the database even for large angle misorientations.

In the following, a minimization is performed to identify κ_1 and κ_2, in order to fully determine the function f defined in (4.39). This function is essential to defined the macroscopic energy $\mathscr{E}_{\text{macro}}$ as detailed in (4.19). The data set used for the minimization is composed of the following components of the database:

$$U = \left\{ \left(\mu_0^{(k)}, \mu_1^{(k)}, \mu_2^{(k)}, E_{\text{meso}}^{(k)} \right), 1 \leq k \leq N_{\text{data}} \right\} \tag{4.40}$$

where E_{meso} is the dimensionless GB energy at 0 K defined in (4.29), and the exponent (k) stands for the k-th entry in the database (i.e., a particular RVE). The least-squares method is used to carry out the minimization procedure. More precisely, the natural Euclidean distance between the dimensionless GB energy E_{meso} in the database and predictions of the analytical function f in (4.39) is minimized. Thus the minimization problem reads:

$$(\kappa_1, \kappa_2) = \underset{(\kappa_1^*, \kappa_2^*) \in \mathbb{R}^2}{\text{argmin}} \sum_{k=1}^{N_{\text{data}}} \left(E_{\text{meso}}^{(k)} - \mathscr{F}^{(k)} \left[\kappa_1^*, \kappa_2^* \right] \right)^2 \tag{4.41}$$

where:

$$\mathscr{F}^{(k)} \left[\kappa_1^*, \kappa_2^* \right] = \kappa_1^* \mu_0^{(k)} \widetilde{\mu}_1^{(k)} \left(\kappa_2^* - \log\left(\widetilde{\mu}_1^{(k)} \right) - \frac{1}{2} \left(\widetilde{\mu}_2^{(k)} + 1 \right) \right) \tag{4.42}$$

where $\widetilde{\mu}_1^{(k)}, \widetilde{\mu}_2^{(k)}$ are computed from $\mu_0^{(k)}, \mu_1^{(k)}, \mu_2^{(k)}$ accordingly to (4.2).

The linear minimization problem (4.41) is fairly simple and is equivalent to solve:

$$\underline{\underline{X}} \cdot \begin{bmatrix} \kappa_1 \kappa_2 \\ \kappa_1 \end{bmatrix} = \underline{E}_{\text{meso}} \tag{4.43}$$

where $\underline{E}_{\text{meso}} = (E_{\text{meso}}^{(k)})_{1 \leq k \leq N_{\text{data}}}$ is a vector of size N_{data}, and $\underline{\underline{X}}$ is a second order tensor of size $N_{\text{data}} \times 2$ defined by:

$$\begin{cases} X_{k,1} = \mu_0^{(k)} \widetilde{\mu}_1^{(k)} \\ X_{k,2} = -\mu_0^{(k)} \widetilde{\mu}_1^{(k)} \left(\log\left(\widetilde{\mu}_1^{(k)} \right) + \dfrac{1}{2} \left(\widetilde{\mu}_2^{(k)} + 1 \right) \right) \end{cases} \tag{4.44}$$

Thus, the solution of the minimization problem (4.41) reads:

$$\begin{bmatrix} \kappa_1 \kappa_2 \\ \kappa_1 \end{bmatrix} = \left(\underline{\underline{X}}^T \cdot \underline{\underline{X}} \right)^{-1} \cdot \underline{\underline{X}}^T \cdot \underline{E}_{\text{meso}} \tag{4.45}$$

Table 4.2: Dimensionless coefficients involved in the energy.

κ_1	1.7
κ_2	0.9

And results are listed in table 4.2.

The coefficient of determination r^2 quantifies the part of the variance of the data (i.e., E_{meso}) that is explained by the model (i.e., the f function). This coefficient of determination has been computed, and $r^2 = 0.998$. Thus, the dimensionless analytic function f almost perfectly captures the GB energy at the macroscopic scale, which can be considered as deterministic function. A comparison between data and the model is presented in figure 4.3, and a perfect fit is observed.

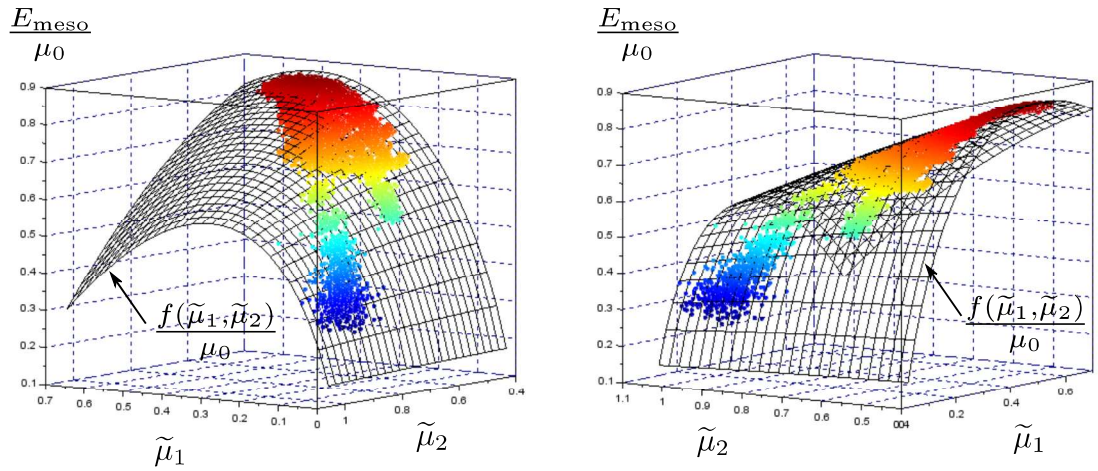

Figure 4.3: Dimensionless GB energy E_{meso}/μ_0 and analytic function f/μ_0 as a function of $\widetilde{\mu}_1$ and $\widetilde{\mu}_2$ computed from $\underline{\mu}_{\text{meso}}$.

The main result of this section is that the upscaling of the total GB energy leads to a deterministic function of the macroscopic state. Therefore, the choice of considering the successive statistical moments in (4.1) as a basis to construct the primary state variables $\underline{\mu}_{\text{macro}}$ is validated.

4.6 Identification of the macroscopic mobility tensor

In this section, the mobility tensor $\underline{\underline{\Gamma}}_{\text{meso}}$ arising in(4.18) and the vector $\underline{\Lambda}_{\text{meso}}$ arising in (4.26) are analyzed. There is no available analytical computation such as presented in section 4.5.1 to guide the development of a macroscopic model. Thus, the identification is carried out only with statistical treatments of the data. In addition, as already mentioned in section 4.2.2, a secondary state variable η_{macro} is necessary to deal with the sensitivity of $\underline{\underline{\Gamma}}_{\text{meso}}$ and $\underline{\Lambda}_{\text{meso}}$ to the presence of very small grains. The secondary state variable is introduced to explain a new quantity that will be called the tessellation amplification factor, which is a scaling factor so that all tessellations are comparable.

4.6.1 Raw data

In figure 4.4, raw data of the dimensionless mobility tensor $\underline{\underline{\Gamma}}_{\text{meso}}$ and the vector $\underline{\Lambda}_{\text{meso}}$ are presented as a function of $\widetilde{\mu}_1$ (computed from $\underline{\mu}_{\text{meso}}$ according to (4.2)). Colors correspond to the tessellation index. More precisely, each point in figure 4.4 correspond to a specific OT indexed by k (with $1 \leq k \leq N_{\text{data}}$) and all points sharing the same color correspond to a single tessellations indexed by i_d (where $1 \leq i_d \leq N_{\text{tess}}$) with different BMDs. It should be noted that the variable $\widetilde{\mu}_2$ that has been used for the energy (see. figure 4.3) does not explain the variance of the raw data for $\underline{\underline{\Gamma}}_{\text{meso}}$ and $\underline{\Lambda}_{\text{meso}}$, and is not used to interpret these results. In addition, it is clear from figure 4.4 that the dispersion of the raw data is

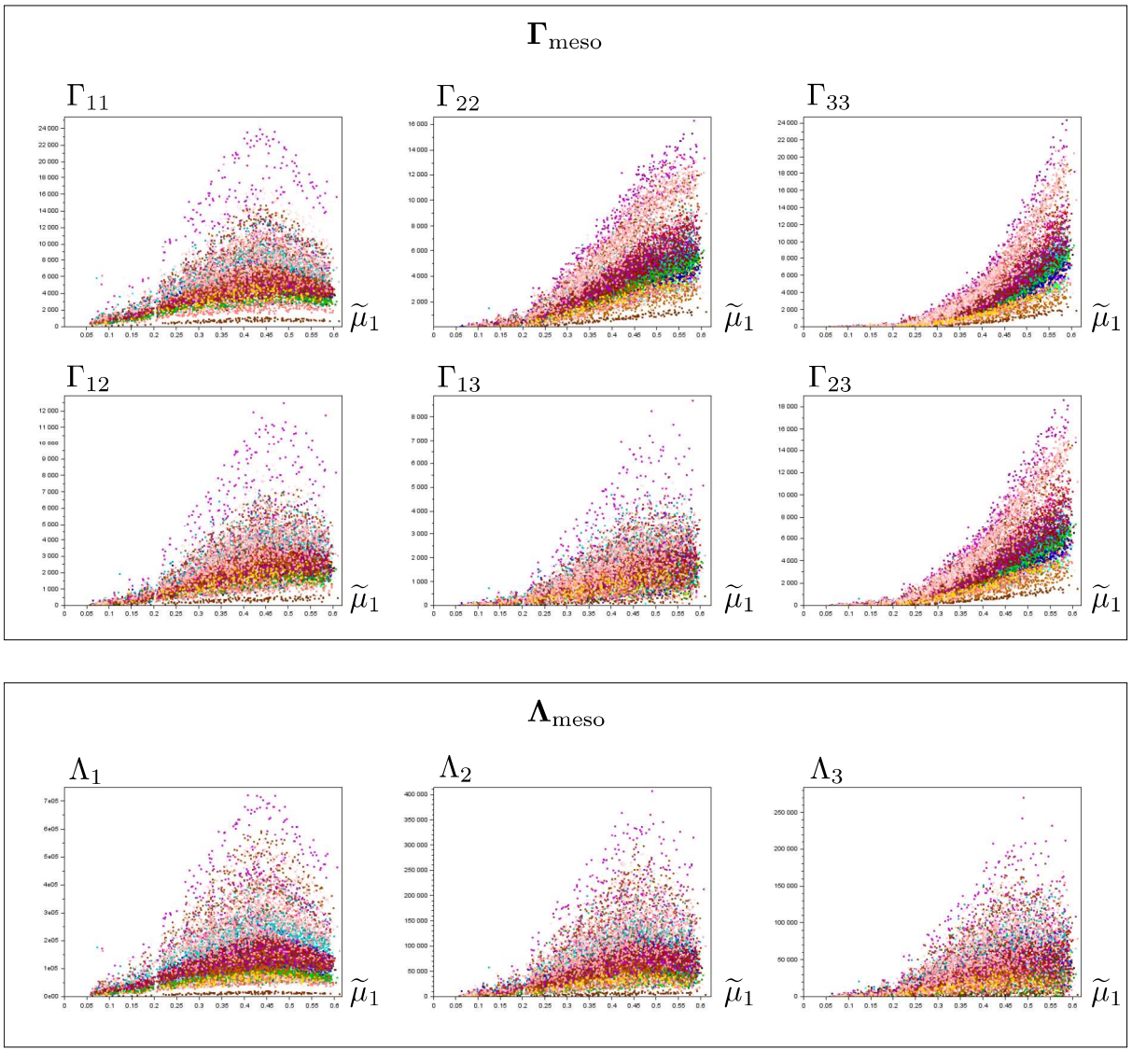

Figure 4.4: Raw data of the dimensionless mobility tensor $\underline{\underline{\Gamma}}_{\text{meso}}$ and the vector $\underline{\Lambda}_{\text{meso}}$ as a function of $\widetilde{\mu}_1$ computed from $\underline{\mu}_{\text{meso}}$. Colors correspond to the tessellation index i_d ($1 \leq i_d \leq N_{\text{tess}}$).

very significant, which would hinders the development of the macroscopic mobility tensor $\underline{\underline{\Gamma}}_{\text{macro}}$ and the vector $\underline{\Lambda}_{\text{macro}}$ involved in the macroscopic evolution laws (4.21) and (4.28) respectively. However, it seems that the tessellation index i_d explains a significant part of

the variance of the raw data, thus there is a quantity that only depends on the tessellation (and does not depends on BMD) that explains a large part of the dispersion observed in figure 4.4, this quantity is introduced as a scaling factor in the following. This aspect is evidences in logarithmic scales as shown in figure 4.5. Indeed, for each component the behavior corresponding the different tessellations i_d is very similar for all tessellations up to an offset in logarithmic scales, which shows that a tessellation amplification factor can be introduced in the usual scales in order to reduce data dispersion.

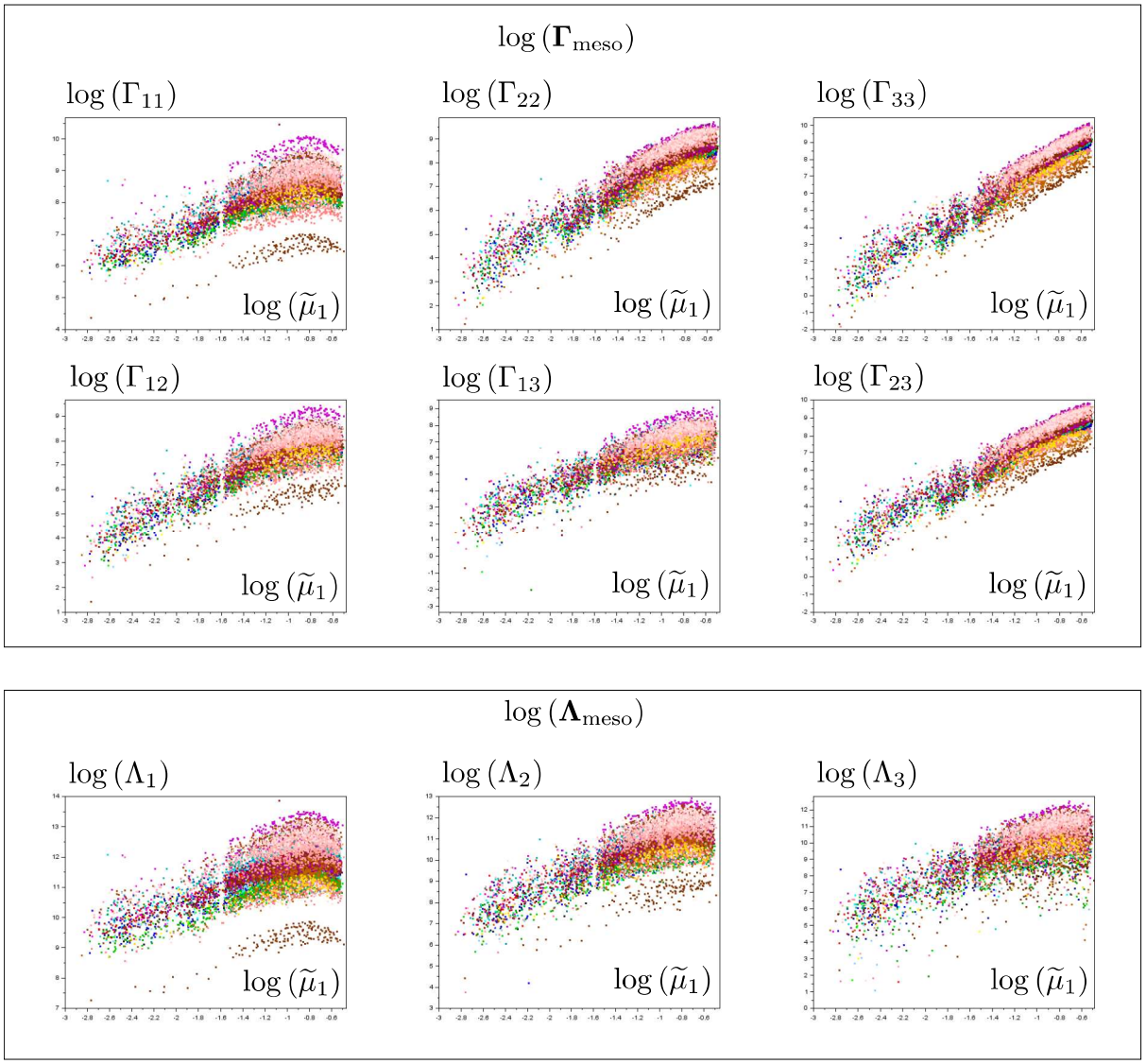

Figure 4.5: Raw data of the dimensionless mobility tensor $\underline{\underline{\Gamma}}_{\text{meso}}$ and the vector $\underline{\Lambda}_{\text{meso}}$ as a function of $\widetilde{\mu}_1$ computed from $\underline{\mu}_{\text{meso}}$ in logarithmic scales. Colors correspond to the tessellation index i_d ($1 \leq i_d \leq N_{\text{tess}}$).

4.6.2 Interpolation in logarithmic scales and amplification factor

The raw data in logarithmic scales are almost linear as a function of $\log\widetilde{\mu_1}$, as shown in figure 4.5. More precisely, it is convenient to interpolate these data with two linear func-

tions that smoothly merge at $\log\left(\widetilde{\mu}_1\right) = x_{\text{cut}}$ where $x_{\text{cut}} = -0.82$. Thus, sigmoid functions are considered for the interpolation to carry out the smooth connection between the two linear functions. Thus the interpolation function in logarithmic scales, for each tessellation i_d, and each component reads:

$$F_{(.)}^{(i_d)} : x \mapsto \frac{A_{(.)}^{(i_d)} x + B_{(.)}^{(i_d)}}{1 + \exp\left(a\left(x - x_{\text{cut}}\right)\right)} + \frac{C_{(.)}^{(i_d)} x + D_{(.)}^{(i_d)}}{1 + \exp\left(-a\left(x - x_{\text{cut}}\right)\right)} \tag{4.46}$$

where the symbol (.) stands for the index of the component (i.e., 11,22, etc. for $\underline{\underline{\Gamma}}_{\text{meso}}$ and 1,2,3 for $\underline{\Lambda}_{\text{meso}}$), and a is a parameter that determines the behavior of the connection between the two linear functions $x \mapsto A_{(.)}^{(i_d)} x + B_{(.)}^{(i_d)}$ and $x \mapsto C_{(.)}^{(i_d)} x + D_{(.)}^{(i_d)}$. In the following this parameters has been set to $a = 10$. Coefficients $A_{(.)}^{(i_d)}, B_{(.)}^{(i_d)}, C_{(.)}^{(i_d)}, D_{(.)}^{(i_d)}$ are not independent as the linear functions should connect in $x = x_{\text{cut}}$. Thus the following relation holds:

$$D_{(.)}^{(i_d)} = \left(A_{(.)}^{(i_d)} - C_{(.)}^{(i_d)}\right) x_{\text{cut}} + B_{(.)}^{(i_d)} \tag{4.47}$$

Thus, coefficients $A_{(.)}^{(i_d)}, B_{(.)}^{(i_d)}, C_{(.)}^{(i_d)}$ should be determined by minimizing a distance between the data the predictions of the interpolation functions $F_{(.)}^{(i_d)}$ defined in (4.46). The least-squares method is used to carry out the minimization, thus:

$$\left(A_{(.)}^{(i_d)}, B_{(.)}^{(i_d)}, C_{(.)}^{(i_d)}\right) = \underset{\left(A^*, B^*, C^*\right) \in \mathbb{R}^4}{\operatorname{argmin}} \sum_{k \in \mathscr{K}(i_d)} \left[\log\left(\Gamma_{(.)}^{(k)}\right) - F_{(.)}^{(i_d)}\left(\log\left(\widetilde{\mu}_1^{(k)}\right)\right)\right]^2 \tag{4.48}$$

where $\Gamma_{(.)}^{(k)}$ is the component (.) of $\underline{\underline{\Gamma}}_{\text{meso}}$ for the k-th OT in the database, and where $\mathscr{K}(i_d)$ is the set of OTs sharing the tessellation i_d. Thus, $\text{card}\left[\mathscr{K}(i_d)\right] = N_{\text{ori}}$, where N_{ori} is the number of crystallographic orientation fields for each tessellation i_d. Of course the same minimization problem holds for the components of $\underline{\Lambda}_{\text{meso}}$. The minimization problem (4.48) is linear and is equivalent to solve:

$$\underline{\underline{X}} \cdot \begin{bmatrix} A_{(.)}^{(i_d)} \\ B_{(.)}^{(i_d)} \\ C_{(.)}^{(i_d)} \end{bmatrix} = \log\left(\underline{\Gamma}_{(.)}^{(i_d)}\right) \tag{4.49}$$

where $\underline{\Gamma}_{(.)}^{(i_d)} = \left(\Gamma_{(.)}^{(k)}\right)_{k \in \mathscr{K}(i_d)}$. The vector $\underline{\Gamma}_{(.)}^{(i_d)}$ is of size N_{ori}, and $\underline{\underline{X}}$ is a second order tensor of size $N_{\text{ori}} \times 3$ defined by:

$$\forall k \in \mathscr{K}(i_d), \begin{cases} X_{k,1} = \dfrac{\log\left(\widetilde{\mu}_1^{(k)}\right)}{\left(1 + \exp\left(a\left(\log\left(\widetilde{\mu}_1^{(k)}\right) - x_{\text{cut}}\right)\right)\right)} + \dfrac{x_{\text{cut}}}{\left(1 + \exp\left(-a\left(\log\left(\widetilde{\mu}_1^{(k)}\right) - x_{\text{cut}}\right)\right)\right)} \\ X_{k,2} = \dfrac{1}{\left(1 + \exp\left(a\left(\log\left(\widetilde{\mu}_1^{(k)}\right) - x_{\text{cut}}\right)\right)\right)} + \dfrac{1}{\left(1 + \exp\left(-a\left(\log\left(\widetilde{\mu}_1^{(k)}\right) - x_{\text{cut}}\right)\right)\right)} \\ X_{k,3} = \dfrac{\left(\log\left(\widetilde{\mu}_1^{(k)}\right) - x_{\text{cut}}\right)}{\left(1 + \exp\left(-a\left(\log\left(\widetilde{\mu}_1^{(k)}\right) - x_{\text{cut}}\right)\right)\right)} \end{cases} \tag{4.50}$$

Thus, the solution of the minimization problem reads:

$$\begin{bmatrix} A_{(.)}^{(i_d)} \\ B_{(.)}^{(i_d)} \\ C_{(.)}^{(i_d)} \end{bmatrix} = \left(\underline{\underline{X}}^T \cdot \underline{\underline{X}}\right)^{-1} \cdot \underline{\underline{X}}^T \cdot \underline{\Gamma}_{(.)}^{(i_d)} \tag{4.51}$$

Of course the same minimization procedure holds for the components of $\underline{\Lambda}_{\text{meso}}$. For instance, the interpolation is demonstrated for some tessellations for the 11 component of $\underline{\underline{\Gamma}}_{\text{meso}}$ in figure 4.6a. It is clear that all tessellations have similar interpolation up to an offset. Thus in classic scales there is a tessellation amplification factor denoted by $\zeta_{(.)}$, which leads in logarithmic scales to an additive offset $\log\left(\zeta_{(.)}\right)$. This quantity is specific to each tessellation and does not depend on the crystal orientation distribution in the RVE. Thus, in the following the notation $\zeta_{(.)}^{(i_d)}$ refers to the specific value of $\zeta_{(.)}$ for the tessellation i_d where $1 \leq i_d \leq N_{\text{tess}}$. For the first tessellation (i.e., $i_d = 1$) the offset is arbitrarily set to:

$$\log\left(\zeta_{(.)}^{(1)}\right) = F_{(.)}^{(1)}\left(x_{\text{cut}}\right) \tag{4.52}$$

For the other tessellations (i.e., $i_d \geq 2$), the offset $\log\left(\zeta_{(.)}^{(i_d)}\right)$ is determined by solving the following least-squares minimization problem:

$$\log\left(\zeta_{(.)}^{(i_d)}\right) = \underset{\log\left(\zeta^*\right) \in \mathbb{R}}{\operatorname{argmin}} \sum_{k \in \mathcal{K}(i_d)} \left[F_{(.)}^{(i_d)}\left(\log\left(\widetilde{\mu}_1^{(k)}\right)\right) - \log\left(\zeta^*\right) - \left(F_{(.)}^{(1)}\left(\log\left(\widetilde{\mu}_1^{(k)}\right)\right) - \log\left(\zeta_{(.)}^{(1)}\right)\right)\right]^2 \tag{4.53}$$

The minimization problem (4.53) is linear, and the solution reads for $i_d \geq 2$:

$$\log\left(\zeta_{(.)}^{(i_d)}\right) = \frac{1}{N_{\text{ori}}} \sum_{k \in \mathcal{K}(i_d)} F_{(.)}^{(i_d)}\left(\log\left(\widetilde{\mu}_1^{(k)}\right)\right) - \left(F_{(.)}^{(1)}\left(\log\left(\widetilde{\mu}_1^{(k)}\right)\right) - \log\left(\zeta_{(.)}^{(1)}\right)\right) \tag{4.54}$$

Of course (4.54) also holds for the components of $\underline{\Lambda}_{\text{meso}}$. For instance the interpolation corrected with the tessellation amplification factor is demonstrated for the 11 component of $\underline{\underline{\Gamma}}_{\text{meso}}$ in figure 4.6b.

4.6.3 Interpolation of rescaled data

The rescaled data are by definition:

$$\mathcal{S} = \left\{ \left(\frac{\Gamma_{11}^{(k)}}{\zeta_{11}^{(i_d)}}, \frac{\Gamma_{22}^{(k)}}{\zeta_{22}^{(i_d)}}, \frac{\Gamma_{33}^{(k)}}{\zeta_{33}^{(i_d)}}, \frac{\Gamma_{12}^{(k)}}{\zeta_{12}^{(i_d)}}, \frac{\Gamma_{13}^{(k)}}{\zeta_{13}^{(i_d)}}, \frac{\Gamma_{23}^{(k)}}{\zeta_{23}^{(i_d)}}, \frac{\Lambda_1^{(k)}}{\zeta_1^{(i_d)}}, \frac{\Lambda_2^{(k)}}{\zeta_2^{(i_d)}}, \frac{\Lambda_3^{(k)}}{\zeta_3^{(i_d)}} \right), \forall k \in \mathcal{K}(i_d), \forall i_d \in \{1, \cdots, N_{\text{tess}}\} \right\} \tag{4.55}$$

Since the rescaled data coincide on a common trend (see. figure 4.6b), it is possible to propose a single interpolation function in logarithmic scales for all the tessellations:

$$F_{(.)}^{\text{sc}} : x \mapsto \frac{A_{(.)}x + B_{(.)}}{1 + \exp\left(a\left(x - x_{\text{cut}}\right)\right)} + \frac{C_{(.)}x + D_{(.)}}{1 + \exp\left(-a\left(x - x_{\text{cut}}\right)\right)} \tag{4.56}$$

where the exponent sc stands for *re-scaled*, and the symbol (.) stands for 11, 22, etc. for the components of $\underline{\underline{\Gamma}}_{\text{meso}}$ and for 1,2,3 for the components of $\underline{\Lambda}_{\text{meso}}$ and where:

$$D_{(.)} = \left(A_{(.)} - C_{(.)}\right) x_{\text{cut}} + B_{(.)} \tag{4.57}$$

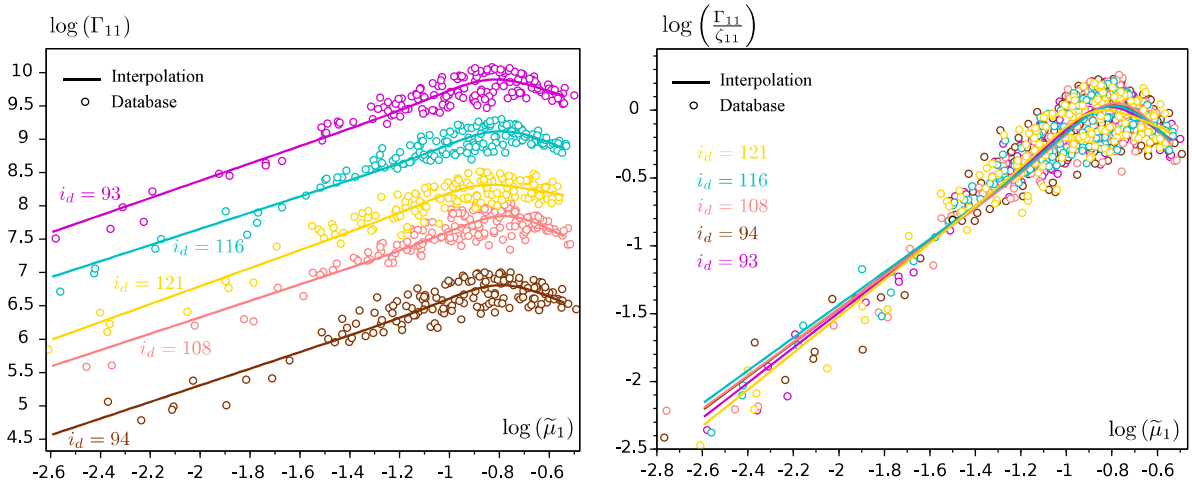

(a) $\log(\Gamma_{11})$ *vs* $\log(\tilde{\mu}_1)$ for some tessellations.

(b) $\log\left(\frac{\Gamma_{11}}{\zeta_{11}}\right)$ *vs* $\log\left(\tilde{\mu}_1\right)$ for some tessellations.

Figure 4.6: Comparison between data and interpolation for some tessellations.

Coefficients $A_{(.)}, B_{(.)}, C_{(.)}$ are determined in a very similar way as in section 4.6.2. The first difference is that the rescaled data (4.55) are considered instead of the raw data. The second difference is that for each component of $\underline{\underline{\Gamma}}_{\text{meso}}$ and $\underline{\Lambda}_{\text{meso}}$ instead of identifying an interpolation for each tessellation, a single interpolation is identified for all the tessellations considered as a whole. The rescaled data (4.55) are presented along with the interpolation (4.56) in logarithmic scales in figure 4.7 and in classic scales in figure 4.8. The identified coefficients are listed in table 4.3.

Table 4.3: Coefficients for the interpolation of rescaled data.

Component	$A_{(.)}$	$B_{(.)}$	$C_{(.)}$
11	1.238	1.031	-0.926
22	2.585	2.245	1.129
33	3.991	3.534	3.459
12	1.925	1.609	-0.402
13	2.506	2.086	0.238
23	3.296	2.898	2.332
1	1.244	1.043	-0.986
2	1.944	1.643	-0.58
3	2.554	2.174	-0.239

Moreover, it should be noted that the different components of $\zeta_{(.)}$ are strongly correlated. In figure 4.9 linear relationships are exhibited. Thus, in order to simplify the analysis, only ζ_{33} is analyzed in the following, as the other components can be inferred with reasonable accuracy from ζ_{33}. Proportionality coefficient are listed in table 4.4. Of course this analysis is simplified and a multivariate model with a covariance could have been used instead, nevertheless the correlation between the different components of the tessellation amplification factor $\zeta_{(.)}$ is sufficient to enable such an assumption.

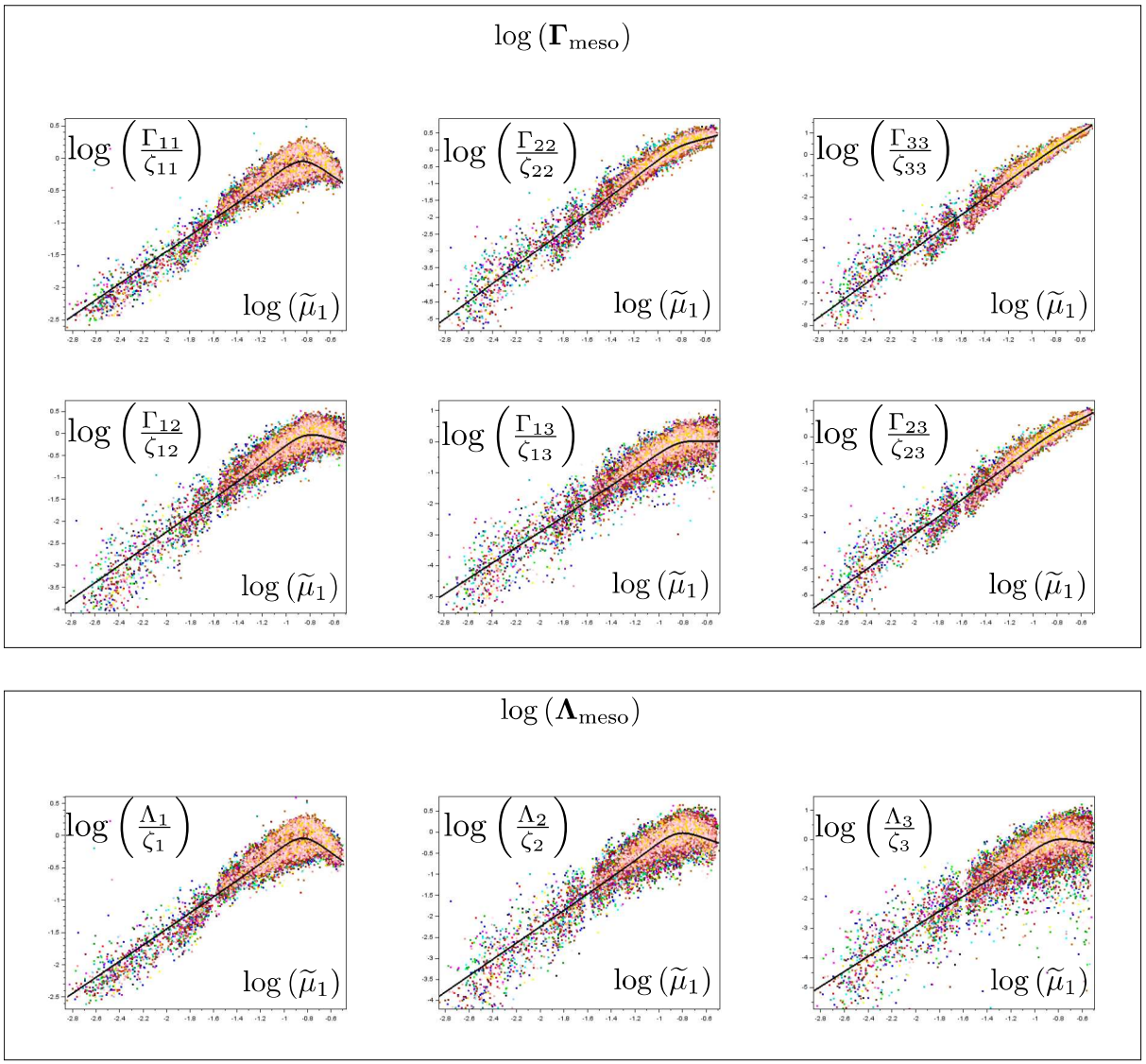

Figure 4.7: Rescaled data corresponding to $\underline{\underline{\Gamma}}_{\text{meso}}$ and $\underline{\Lambda}_{\text{meso}}$ as a function of $\widetilde{\mu}_1$ computed from $\underline{\mu}_{\text{meso}}$ in logarithmic scales. Colors correspond to the tessellation index i_d ($1 \leq i_d \leq N_{\text{tess}}$).

Table 4.4: Proportionality coefficients for $\zeta_{(.)}$.

Component	Coefficient
11	2.189
22	1.431
33	1.000
12	1.019
13	0.543
23	1.137
1	61.980
2	28.428
3	14.450

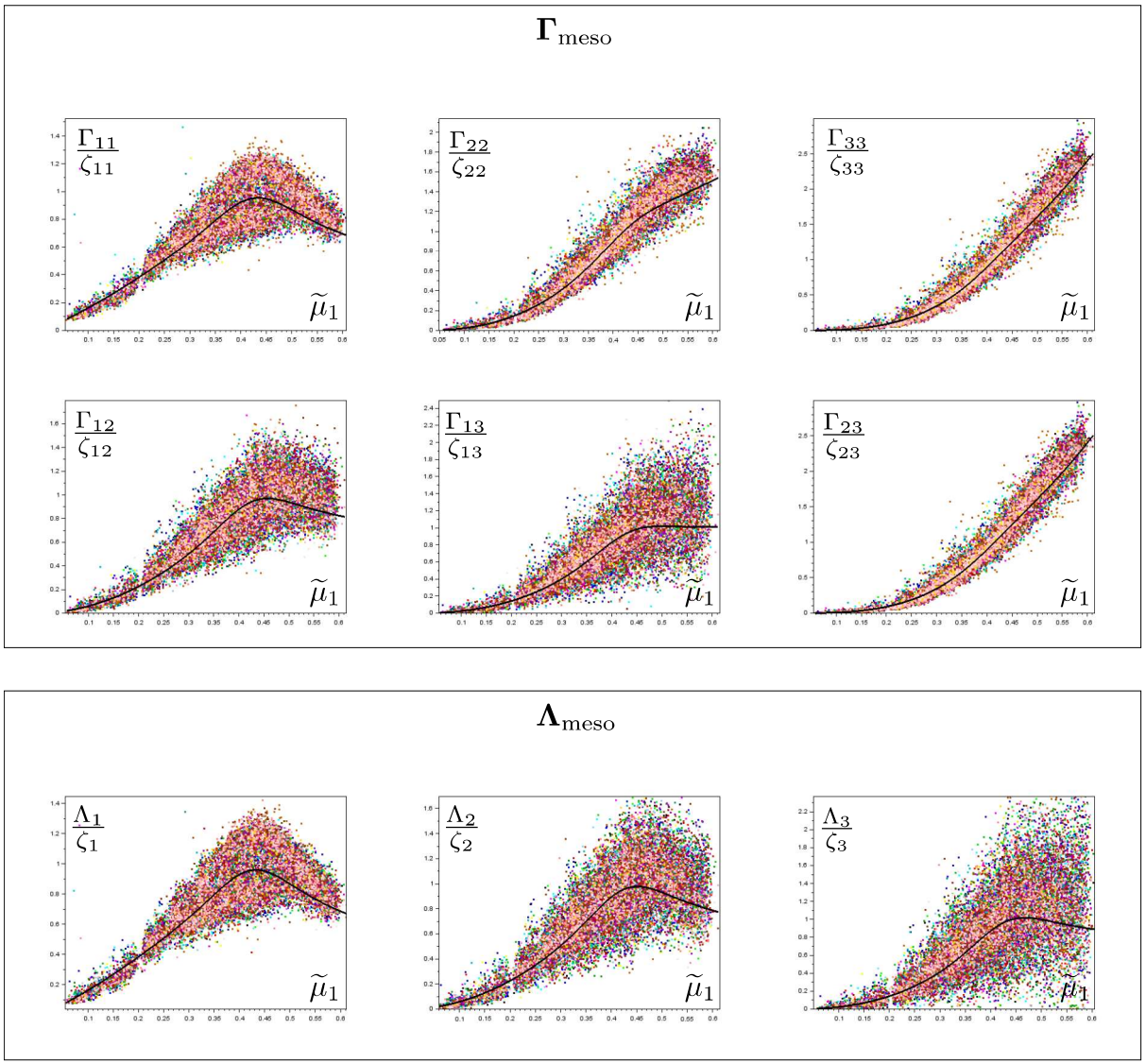

Figure 4.8: Raw data corresponding to $\underline{\underline{\Gamma}}_{\text{meso}}$ and $\underline{\Lambda}_{\text{meso}}$ as a function of $\widetilde{\mu}_1$ computed from $\underline{\mu}_{\text{meso}}$. Colors correspond to the tessellation index i_d ($1 \leq i_d \leq N_{\text{tess}}$).

4.6.4 Macroscopic amplification factor

At this stage, the interpolation (4.56) can be used at the macroscopic scale. However, the tessellation amplification factor $\zeta_{(.)}$ obtained in (4.54) highly depends on the detailed arrangement of the tessellation. An interpolation function that can be used at the macroscopic scale is derived in this section. This interpolation relies on the variable η_{meso} introduced in (4.4). In figure 4.10 the values of ζ_{33} obtained for all tessellations in (4.54) are presented as a function of η_{meso}. A correlation can be observed and a linear interpolation function is proposed:

$$G : x \mapsto \widehat{A}\,x + \widehat{B} \tag{4.58}$$

It should be mentioned that the proposed linear model explains a large part of the variance observed in the data (i.e., $r^2 = 0.79$), however the linear relationship between the different components of $\zeta_{(.)}$ is imperfect (see. figure 4.9). Therefore, further work should focus on

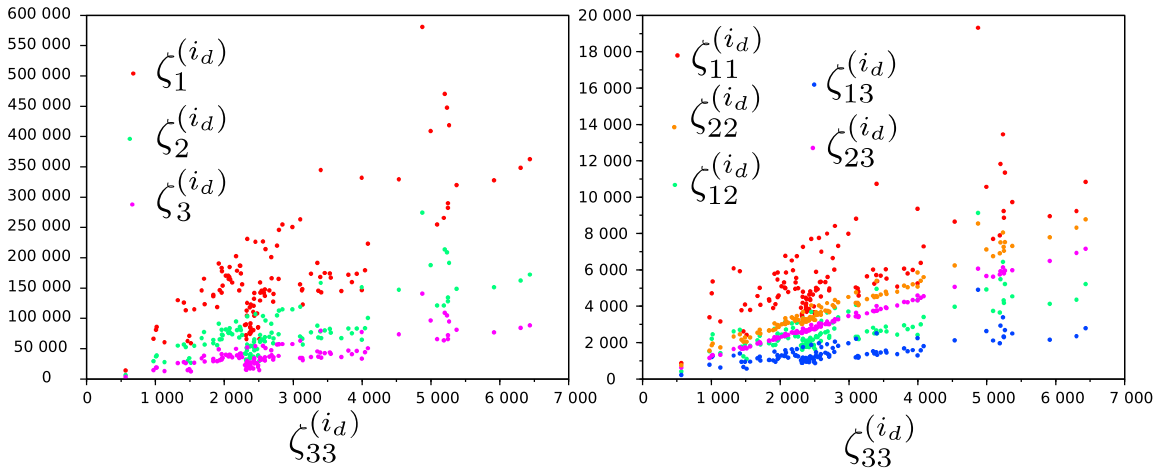

Figure 4.9: Correlation between the different components of $\zeta_{(.)}$

improving this particular aspect of the model.

A simple linear regression can be performed by minimizing with the least-squares method. However since the are a limited amount of data with non negligible statistical dispersion, it is preferable to identify the linear model within the framework of Bayesian inference as detailed in section 4.7. Since η_{meso} has a macroscopic counterpart η_{macro} defined in section 4.2.2, whose evolution has been obtained in (4.28), a macroscopic amplification factor can be defined on the basis of the interpolation function $G_{(.)}\left(\eta_{\text{macro}}\right)$.

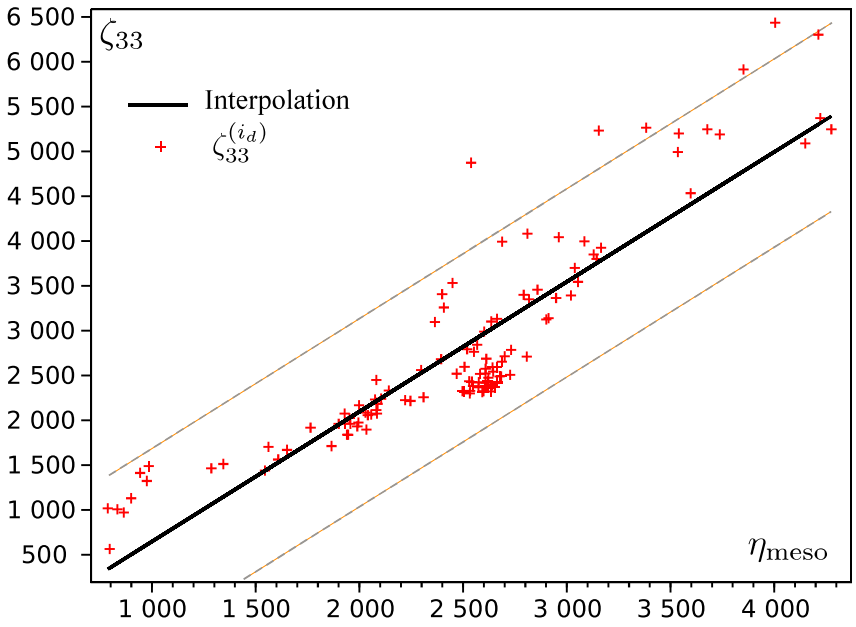

Figure 4.10: Amplification factor ζ_{33} as a function of η_{meso}

4.7 Epistemic uncertainty and Bayesian identification

4.7.1 Model for the tessellation amplification factor

In figures 4.8 and 4.10, it is clear that data are affected by a non negligible statistical dispersion around the interpolation models (4.56) and (4.58) respectively. Since the mesoscopic model introduced in chapter 3 is fully deterministic, this statistical dispersion arises from the reduction of the amount of data introduced in section 4.2. Indeed, to a single overall state $\underline{\mu}_{\text{meso}}, \eta_{\text{meso}}$ correspond several different detailed mesoscopic states $\underline{\alpha} = (\underline{x}, \underline{y}, \underline{w})$. The statistical dispersion evidenced in figure 4.8 and 4.10 shows that these different detailed mesoscopic states are not equivalent with respect to the mobility tensor $\underline{\underline{\Gamma}}_{\text{meso}}$, the vector $\underline{\Lambda}_{\text{meso}}$ and the amplification factor $\zeta_{(.)}$. In other words, different RVEs sharing the same initial overall state $\underline{\mu}_{\text{meso}}, \eta_{\text{meso}}$ do not have the same evolution paths. Thus, the dispersion around the interpolation models (4.56) and (4.58) can be understood as the evidence of an epistemic uncertainty due to the loss of information in the process of reducing the amount of data by introducing the overall state $\underline{\mu}_{\text{meso}}, \eta_{\text{meso}}$. This epistemic uncertainty is not due to the rescaling process detailed in section 4.6.2. Indeed, the statistical dispersion can be observed for each tessellation individually as shown in figure 4.6. Thus, even for the same tessellation, the detailed arrangement of crystal orientations is lost in the overall state, and the epistemic uncertainty arises.

As mentioned in section 4.6.4, parameters $\widehat{A}, \widehat{B}$ involved in the interpolation model (4.58) are identified by using Bayesian techniques. It consists in considering a prior probability density for the model parameters $\widehat{A}, \widehat{B}$, and the likelihood, which is the conditional probability density of the data ζ_{33} with respect to the model parameter $\widehat{A}, \widehat{B}$. Then, by using the Bayes theorem, the posterior probability density is obtained as the conditional probability of the model parameters with respect to the observed data. A normal model is considered, so the likelihood reads:

$$\zeta_{33}^{(i_d)} | \widehat{A}, \widehat{B}, \widehat{\sigma} \sim \mathcal{N}\left(\widehat{A}\eta_{\text{macro}} + \widehat{B}, \widehat{\sigma}^2\right) \tag{4.59}$$

where $\mathcal{N}\left(\widehat{A}\eta_{\text{macro}} + \widehat{B}, \widehat{\sigma}^2\right)$ is the normal distribution of mean $\widehat{A}\eta_{\text{macro}} + \widehat{B}$, and $\widehat{\sigma}$ is the standard deviation, which characterizes the dispersion around the mean. In addition, Bayesian techniques rely on prior distributions for the unknown parameters. An informative normal distribution is chosen for $\widehat{A}$ the slope can be clearly identified in figure 4.10, and a non-informative uniform distribution is chosen for $\widehat{B}$. Classically conjugate standard deviation prior follows a inverted chi-squared probability density. Hence:

$$\begin{cases} \widehat{A} \sim \mathcal{N}\left(\mu_{\widehat{A}}, s_{\widehat{A}}\right) \\ \widehat{B} \sim \mathcal{U}\left(\widehat{B}_{\min}, \widehat{B}_{\max}\right) \\ \widehat{\sigma} \sim \text{Inv}-\chi^2\left(\widehat{s}^2, \widehat{\nu}\right) \end{cases} \tag{4.60}$$

where parameters $\mu_{\widehat{A}}, s_{\widehat{A}}, \widehat{B}_{\min}, \widehat{B}_{\max}, \widehat{s}, \widehat{\nu}$ are chosen so that the priors are consistent with figure 4.10:

$$\begin{cases} \mu_{\widehat{A}} = 1.5 \\ s_{\widehat{A}} = 0.3 \\ \widehat{B}_{\min} = -1300 \\ \widehat{B}_{\max} = 300 \\ \widehat{s} = 400 \\ \widehat{\nu} = 20 \end{cases} \tag{4.61}$$

Bayesian inference consists in computing the posterior probability density by using the Bayes theorem, hence:

$$p(\widehat{A},\widehat{B},\widehat{\sigma}|\underline{\zeta}_{33}) \propto p(\underline{\zeta}_{33}|\widehat{A},\widehat{B},\sigma)p(\widehat{A})p(\widehat{B})p(\sigma) \tag{4.62}$$

Statistics of posterior probability density function (4.62) are explored by Markov-Chain Monte Carlo (MCMC) sampling techniques. In practice, a No U-Turn Sampler (NUTS) developed by [93] is used within the framework of the PYMC3 package developed by [94] in PYTHON ([95]). The posterior densities are presented in figure 4.11 as well as a pairplot showing a strong correlation between $\widehat{A}$ and $\widehat{B}$. In addition, maximum a posteriori estimates are computed and listed in table 4.5, and have been used in figure 4.10.

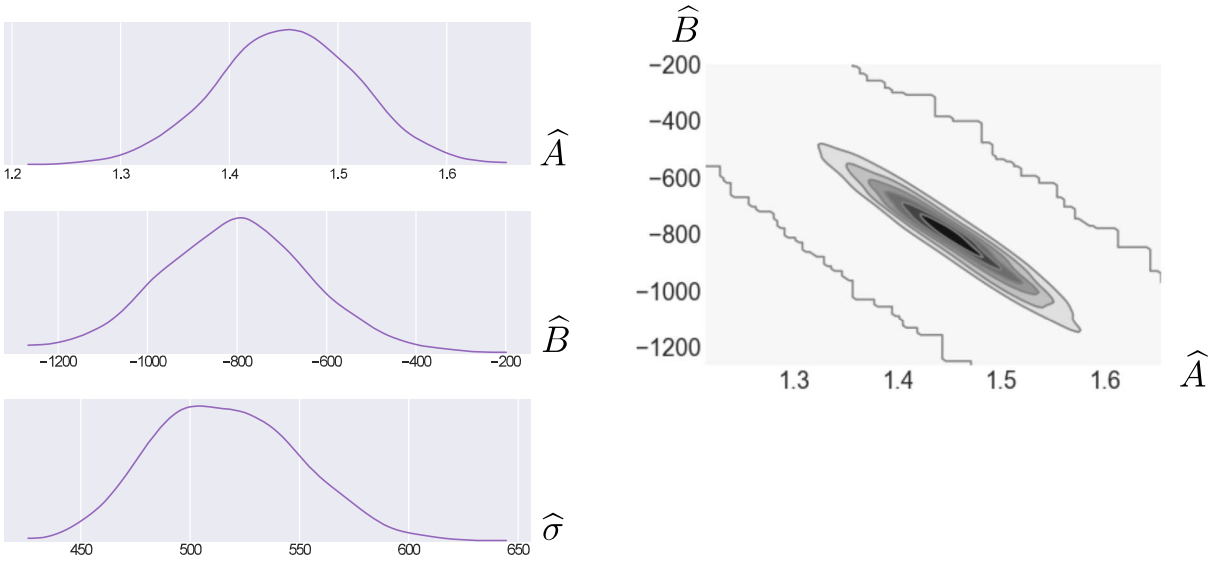

Figure 4.11: Posterior densities and pairplot

Table 4.5: Maximum a posteriori estimates.

Component	$\widehat{A}$	$\widehat{B}$	$\widehat{\sigma}$
33	1.451	-802	512

Thus, one can define a macroscopic deviation with respect to the interpolation model (4.58) denoted by $\widehat{\epsilon}_{\text{macro}}$, whose probability density function reads:

$$\widehat{\epsilon}_{\text{macro}} \sim \mathcal{N}\left(0,\widehat{\sigma}^2\right) \tag{4.63}$$

4.7.2 Uncertainty associated to the macroscopic mobility

For each entry k in the rescaled database (4.55), the deviation with respect to the interpolation model (4.56) is denoted by $\epsilon_{(.)}^{(k)}$ and reads:

$$\forall i_d \in \{1,\cdots,N_{\text{tess}}\}, \forall k \in \mathcal{K}(i_d),\ \epsilon_{(.)}^{(k)} = \frac{\Gamma_{(.)}^{(k)}}{\zeta_{(.)}^{(i_d)}} - \exp\left[F_{(.)}^{\text{sc}}\left(\log\left(\tilde{\mu}_1^{(k)}\right)\right)\right] \tag{4.64}$$

Of course, replacing $\Gamma_{(.)}^{(k)}$ by $\Lambda_{(.)}^{(k)}$ in (4.64), the same definition applies for the deviation with respect to the interpolation model of $\underline{\Lambda}_{\text{meso}}$. For instance $\epsilon_{33}^{(k)}$ is presented as a function of $\widetilde{\mu}_1^{(k)}$ for $1 \leq k \leq N_{\text{data}}$ in figure 4.12a. It is clear the the deviation depends on $\widetilde{\mu}_1$, and $\epsilon_{33}^{(k)} / \left(\widetilde{\mu}_1^{(k)}\right)^2$ is presented in figure 4.12b. The corresponding histogram is presented in figure 4.14 showing that a Gaussian model is acceptable.

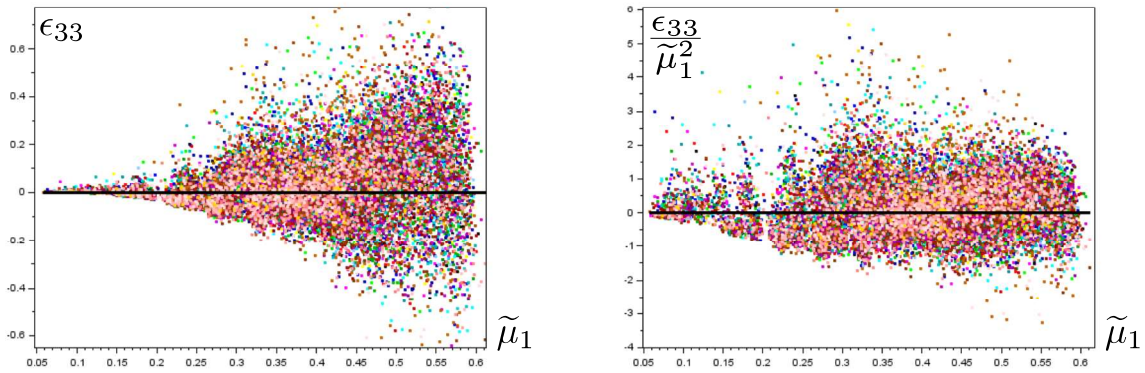

(a) ϵ_{33} *vs* $\widetilde{\mu}_1$.

(b) $\epsilon_{33}/\widetilde{\mu}_1^2$ *vs* $\widetilde{\mu}_1$.

Figure 4.12: Statistical dispersion around the interpolation function.

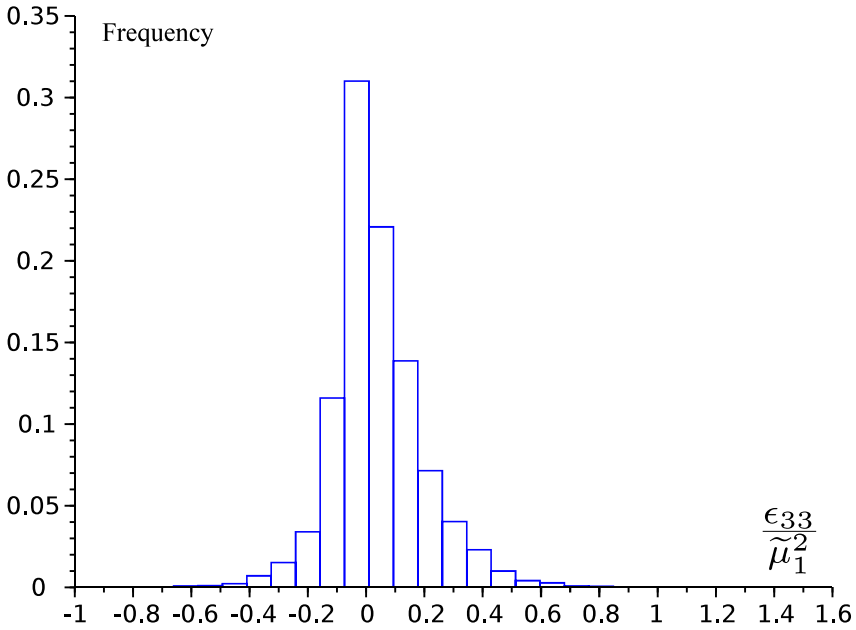

Figure 4.13: Histogram of statistical dispersion around the interpolation function for the 33 component of $\underline{\Gamma}_{\text{meso}}$.

Figure 4.14: Statistical dispersion around the interpolation function.

Since the different components of the deviation (4.64) are correlated, a multivariate Gaussian distribution is chosen. Thus, one can define the macroscopic deviation as a ran-

dom variable vector denoted by $\underline{\epsilon}_{\text{macro}}/\widetilde{\mu}_1^2$ whose probability density function is a multivariate Gaussian distribution of zero mean and covariance matrix $\underline{\underline{C}}$ of size 9×9. Alternatively one can estimate the probability density function of $\underline{\underline{C}}$ within the framework of Bayesian inference. Since a Gaussian model has been chosen, the likelihood is the following conditional probability density function:

$$\frac{\underline{\epsilon}_{\text{macro}}}{\widetilde{\mu}_1^2} | \underline{\underline{C}} \sim \mathcal{N}_9(0, \underline{\underline{C}}) \tag{4.65}$$

The inverse-Wishart distribution is the conjugate prior for the covariance matrix of a multivariate normal distribution. However, such a distribution is not implemented in usual Bayesian computational packages. Thus, we use the LKJ-Cholesky covariance prior, which is well-suited to computational Bayesian methods:

$$\underline{\underline{L}} \sim \text{LKJ-}\mathscr{C}(9, \nu, \sigma) \tag{4.66}$$

where $\underline{\underline{L}}$ is a lower triangular matrix arising in the Cholesky decomposition of $\underline{\underline{C}}$, namely:

$$\underline{\underline{C}} = \underline{\underline{L}} \cdot \underline{\underline{L}}^T \tag{4.67}$$

and where LKJ-$\mathscr{C}(9, \nu, \sigma)$ the the LKJ-Cholesky distribution of size 9×9, ν is a parameter, which controls the amount of correlation between components of $\underline{\epsilon}_{\text{macro}}/\mu_1^2$, and σ controls the distribution of standard deviation.

$$\begin{cases} \sigma \sim \mathscr{E}(\lambda) \\ \lambda = 1 \\ \nu = 2 \end{cases} \tag{4.68}$$

where $\mathscr{E}(\lambda)$ is the exponential density function of parameter λ. The posterior density function reads:

$$p\left(\underline{\underline{L}} | \frac{\underline{\epsilon}_{\text{macro}}}{\widetilde{\mu}_1^2}\right) \propto p\left(\frac{\underline{\epsilon}_{\text{macro}}}{\widetilde{\mu}_1^2} | \underline{\underline{C}}\right) p(\underline{\underline{L}}) \tag{4.69}$$

Statistics of posterior probability density function (4.69) are explored by Markov-Chain Monte Carlo (MCMC) sampling techniques. In practice, a No U-Turn Sampler (NUTS) developed by [93] is used within the framework of the PYMC3 package developed by [94] in Python ([95]).

4.7.3 Time dependance and numerical implementation

The fundamental nature of the epistemic uncertainty can be understood as follows. Consider random variables denoted by $\Omega_{(.)}$, each of which corresponds to a component (.) of $\underline{\underline{\Gamma}}_{\text{meso}}$ and $\underline{\Lambda}_{\text{meso}}$. The random variable vector $\underline{\Omega} = (\Omega_{11}, \ldots, \Omega_{23}, \Omega_1 \cdots, \Omega_3)$ of size 9 captures the uncertainty due to the random "selection" of a virtual mesoscopic state knowing the macroscopic state. Ideally, a single scalar random variable Ω^* could account for this random "selection". However, the link between the different components of $\underline{\underline{\Gamma}}_{\text{meso}}$ and $\underline{\Lambda}_{\text{meso}}$, which would enable from a single draw of Ω^* to compute the deviations associated to the different components, is unknown at the macroscopic scale and fully depends on the mesoscopic scale. That is why at the macroscopic scale the uncertainty is modeled by

a random variable vector $\underline{\Omega}$. It should be noted that the covariance matrix $\underline{\underline{C}}$ represents the macroscopic link between the different components. The deviation with respect to the interpolation model reads:

$$\begin{cases} \underline{\epsilon}_{\text{macro}} = \widetilde{\mu}_1^2 \underline{\underline{L}} \cdot \underline{\Omega} \\ \widehat{\epsilon}_{\text{macro}} = \widehat{\sigma}\, \widehat{\Omega} \end{cases} \tag{4.70}$$

where $\underline{\underline{L}}$ is defined in (4.67). In addition, $\Omega_{(.)}$ are independent and identically distributed standard normal distributions as well as $\widehat{\Omega}$:

$$\begin{cases} \Omega_{(.)} \sim \mathcal{N}(0,1) \\ \widehat{\Omega} \sim \mathcal{N}(0,1) \end{cases} \tag{4.71}$$

The macroscopic model is therefore probabilistic. However, since the mesoscopic model is fully deterministic, there is no fundamental indeterminacy, only an epistemic uncertainty within the upscaling process due to the loss of information.

At this stage the macroscopic counterparts $\underline{\underline{\Gamma}}_{\text{macro}}$ and $\underline{\Lambda}_{\text{macro}}$ of $\underline{\underline{\Gamma}}_{\text{meso}}$ and $\underline{\Lambda}_{\text{meso}}$ can be stated:

$$\begin{cases} \underline{\underline{\Gamma}}_{\text{macro}} = \left(\underline{\underline{G}}\left(\eta_{\text{macro}}\right) + \underline{\underline{\widehat{\upsilon}}}_{\text{macro}}\right)\left(\exp\left[\underline{\underline{F}}^{\text{sc}}\left(\underline{\mu}_{\text{macro}}\right)\right] + \underline{\underline{\upsilon}}_{\text{macro}}\right) \\ \underline{\Lambda}_{\text{macro}} = \left(\underline{G}\left(\eta_{\text{macro}}\right) + \underline{\widehat{\upsilon}}_{\text{macro}}\right)\left(\exp\left[\underline{F}^{\text{sc}}\left(\underline{\mu}_{\text{macro}}\right)\right] + \underline{\upsilon}_{\text{macro}}\right) \end{cases} \tag{4.72}$$

where $\underline{\underline{F}}^{\text{sc}}$ and $\underline{F}^{\text{sc}}$ are the tensor and vector interpolation functions defined from (4.56), $\underline{\underline{G}}$ and $\underline{G}$ are the tensor and vector interpolation functions defined from (4.58). In addition $\underline{\underline{\upsilon}}_{\text{macro}}$ and $\underline{\upsilon}_{\text{macro}}$ are the tensors and vectors derived form $\underline{\epsilon}_{\text{macro}}$ defined in (4.70). Second order tensors are symmetric of size 3×3 composed of the 11, 22, 33, 12, 13 and 23 components, and vectors are composed of the $1,2,3$ components. Similarly $\underline{\underline{\widehat{\upsilon}}}_{\text{macro}}$ and $\underline{\widehat{\upsilon}}_{\text{macro}}$ are obtained from $\widehat{\epsilon}_{\text{macro}}$ defined in (4.63) and the proportionality coefficients listed in table 4.4.

With the macroscopic definition (4.72), the evolution law (4.21) for $\underline{\mu}_{\text{macro}}$ and the evolution law (4.28) for η_{macro} can be computed numerically. The main difficulty lies in the fact that the random vector $\underline{\Omega}$ correspond to the random "selection" of a virtual mesoscopic state for a known macroscopic state. However, the mesoscopic state slowly evolves during grain growth. Thus, this "selection" of a virtual mesoscopic state should be updated at each time step. If new draws of the random vector $\underline{\Omega}$ were computed at each time step, a completely new virtual mesoscopic state would be "selected" leading to Brownian motion. Of course, this does not correspond to the epistemic uncertainty that has been introduced. Ideally, at each time step new draws of $\underline{\Omega}$, which strongly depend of the draws at the previous time step, would be computed. However, this would need to identify an autocovariance matrix, which is the function of the covariance with respect to pairs of different time steps. In this work, the identification of the macroscopic model has been done according to a *static* approach, as mentioned in section 4.4. Thus, the identification of such an autocovariance matrix is not possible. To overcome this difficulty, we assume that the virtual mesoscopic state, which has been "selected" by the initial draw of the random vector $\underline{\Omega}$, evolves sufficiently slowly so that there is no need to "re-select" a new virtual mesoscopic state for further time steps. That is to say that $\underline{\Omega}$ does not depend on time, and draws of $\underline{\Omega}$ are computed only at $t = 0$ and remain constant during the evolution. However, since $\underline{\epsilon}_{\text{macro}}$ in (4.70) explicitly depends on $\widetilde{\mu}_1(t)$ (computed from $\underline{\mu}_{\text{macro}}$), the overall epistemic uncertainty is nevertheless adjusted during the evolution, but in a simplified way. This leads to consider the evolution laws (4.21) and (4.28) as simple

stochastic processes. The evolutions of means $\langle \underline{\mu}_{\text{macro}} \rangle(t), \langle \eta_{\text{macro}} \rangle(t)$ and point-wise standard deviations $\sigma_{\underline{\mu}_{\text{macro}}}(t), \sigma_{\eta_{\text{macro}}}(t)$ can be computed easily by simulating a large number of evolutions with various draws of $\underline{\Omega}, \widehat{\epsilon}_{\text{macro}}$. One could significantly reduce the number of evolutions to accurately estimate $\langle \underline{\mu}_{\text{macro}} \rangle(t), \langle \eta_{\text{macro}} \rangle(t)$ and $\sigma_{\underline{\mu}_{\text{macro}}}(t), \sigma_{\eta_{\text{macro}}}(t)$ by using spectral approaches [96], but this has not been done in this study as computation time is already reduced.

4.8 Results

In this section, the macroscopic model is implemented numerically and applied to various conditions. More precisely the evolution laws (4.21) and (4.28) are discretized with a simple explicit scheme. It should be mentioned that the temperature T in (4.21) and (4.28) is an external quantity, which of course can depend on time if temperature cycles are considered for instance. To take into account time dependent temperature it is sufficient to update the temperature at each time step in the explicit scheme. However, in the following constant temperature is considered.

Comparisons with the evolution of the overall mesoscopic state are provided to evaluate the model quality. Several tessellations included in the data base $i_d \in \mathscr{I}$ where $\mathscr{I} = \{1, 80, 100\}$ have been considered as initial states for mesoscopic evolutions with crystal orientations assigned with a beta probability density $\mathscr{B}(\alpha, \beta)$ where $(\alpha, \beta) = (1,1)$ and $(\alpha, \beta) = (5,9)$. These tessellations have been selected so that very different morphological textures can be tested. In addition, four tessellations that do not belong to the database have also been considered with very similar initial overall mesoscopic state (these four tessellations are referred in the following as $i_d = 0$). All mesoscopic evolutions have been computed according to the mesoscopic model detailed in chapter 3, and parameters are listed in table 4.6. Some examples of OTs at different times during grain growth are presented in figures 4.15, 4.16 and 4.17.

Table 4.6: Simulation parameters used for both the mesoscopic evolutions.

Temperature	(°C)	T	800
Mobility	($m^4.J^{-1}.s^{-1}$)	$m(T)$	0.146×10^{-13}
Physical size	(mm)	L_0	1
Duration	(hours)	d	10

4.8.1 First validation and numerical implementation

Since the macroscopic model is probabilistic, typical results are the means $\langle \underline{\mu}_{\text{macro}} \rangle(t), \langle \eta_{\text{macro}} \rangle(t)$ and point-wise standard deviations $\sigma_{\underline{\mu}_{\text{macro}}}(t), \sigma_{\eta_{\text{macro}}}(t)$. However, a simplified condition is considered in this section, and consists in neglecting the epistemic uncertainty, that is to say neglecting $\underline{\underline{\upsilon}}_{\text{macro}}$, $\underline{\widehat{\upsilon}}_{\text{macro}}$, $\underline{\upsilon}_{\text{macro}}$, and $\widehat{\upsilon}_{\text{macro}}$ in (4.72). Thus, a single particular macroscopic evolution is compared to the evolution of the overall mesoscopic state $\underline{\mu}_{\text{meso}}, \eta_{\text{meso}}$ in order to determine how both models behave with respect to smoothness.

Comparisons for $i_d = 1$ are presented in figure 4.18. These results show that the general behavior of the macroscopic model is satisfying, but as expected it is smoother than the

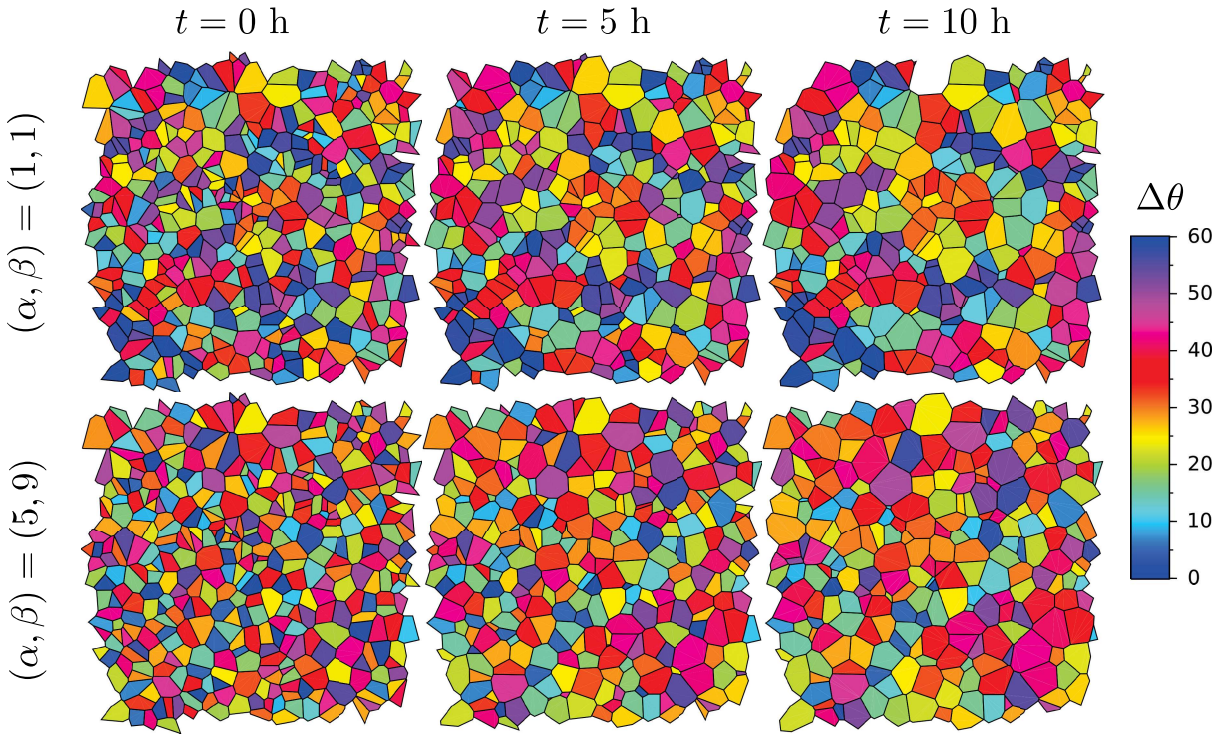

Figure 4.15: OTs at different times for two different BMDs obtained with a beta density $\mathscr{B}(\alpha, \beta)$ for $(\alpha, \beta) = (1, 1)$ and $(\alpha, \beta) = (5, 9)$, $i_d = 1$.

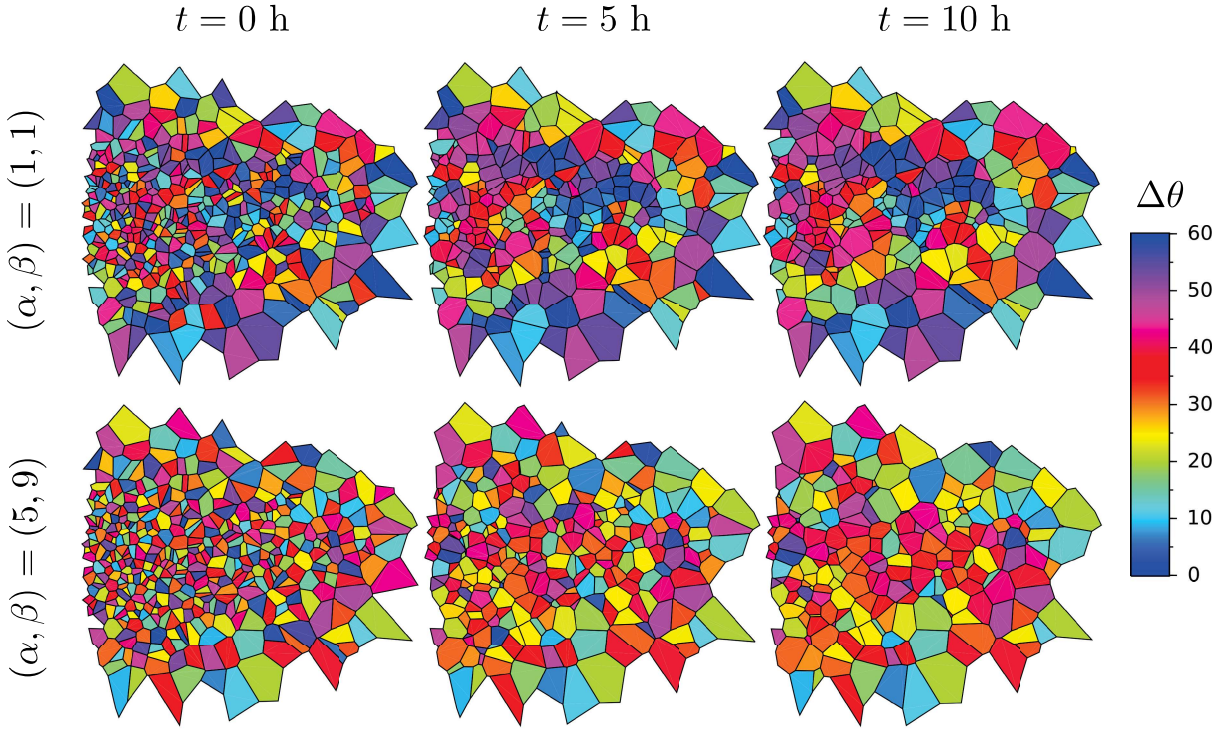

Figure 4.16: OTs at different times for two different BMDs obtained with a beta density $\mathscr{B}(\alpha, \beta)$ for $(\alpha, \beta) = (1, 1)$ and $(\alpha, \beta) = (5, 9)$, $i_d = 80$.

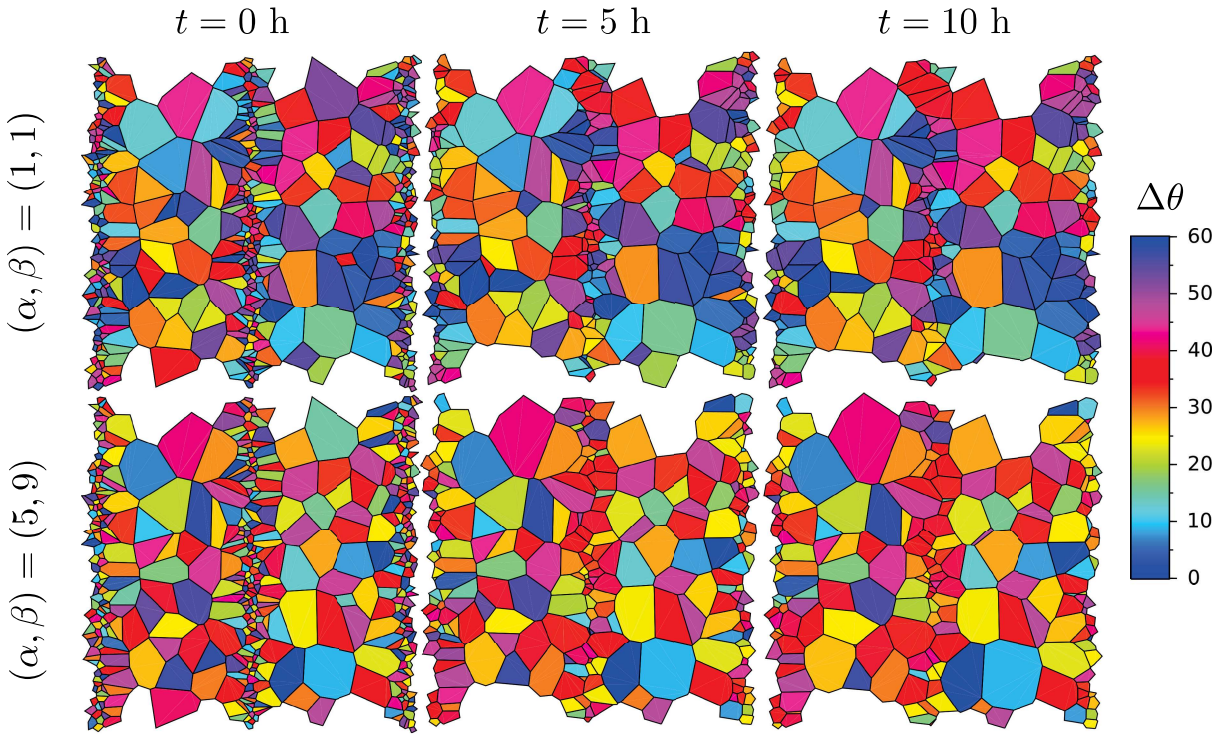

Figure 4.17: OTs at different times for two different BMDs obtained with a beta density $\mathscr{B}(\alpha, \beta)$ for $(\alpha, \beta) = (1, 1)$ and $(\alpha, \beta) = (5, 9)$, $i_d = 100$.

overall mesoscopic evolution. At the beginning of the evolution the macroscopic model is rather accurate even though it may significantly diverge from the overall mesoscopic behavior after the first few hours. A perfect match is of course not expected as the macroscopic evolution is a particular draw of a stochastic process. Nevertheless, the proposed comparisons show that the macroscopic model is unable to capture sudden slope changes for long duration simulations. These slope changes correspond to local events that have significant overall effect. However, $\underline{\underline{\Gamma}}_{\text{macro}}$ depends on $\underline{\mu}_{\text{macro}}, \eta_{\text{macro}}$ in a smooth manner, which explains the regularity of the macroscopic evolutions. This observation shows that the proposed *static* approach, which leads to set the epistemic uncertainty at a constant value during the evolution, contributes to the smoothness of the obtained solution. To take into account sudden slope changes at the macroscopic scale one can propose a *dynamic* approach with a probability of local "events" increasing with time, and leading to sudden changes of $\underline{\underline{\Gamma}}_{\text{macro}}$. However, such an approach seems difficult to develop as the identification of the probability density of local "events" would necessitate to analyze in details a large number of mesoscopic evolutions, although the database used in this study is only composed of various and disconnected mesoscopic states.

4.8.2 Probabilistic results

In this section, the epistemic uncertainty is not neglected in (4.72), thus the probabilistic nature of the macroscopic model is evidenced. Draws of the various model parameters involved in the Bayesian identification are obtained as detailed detailed in section 4.7 and used to generate $N_{\text{stat}} = 500$ macroscopic evolutions whose means, medians and point-

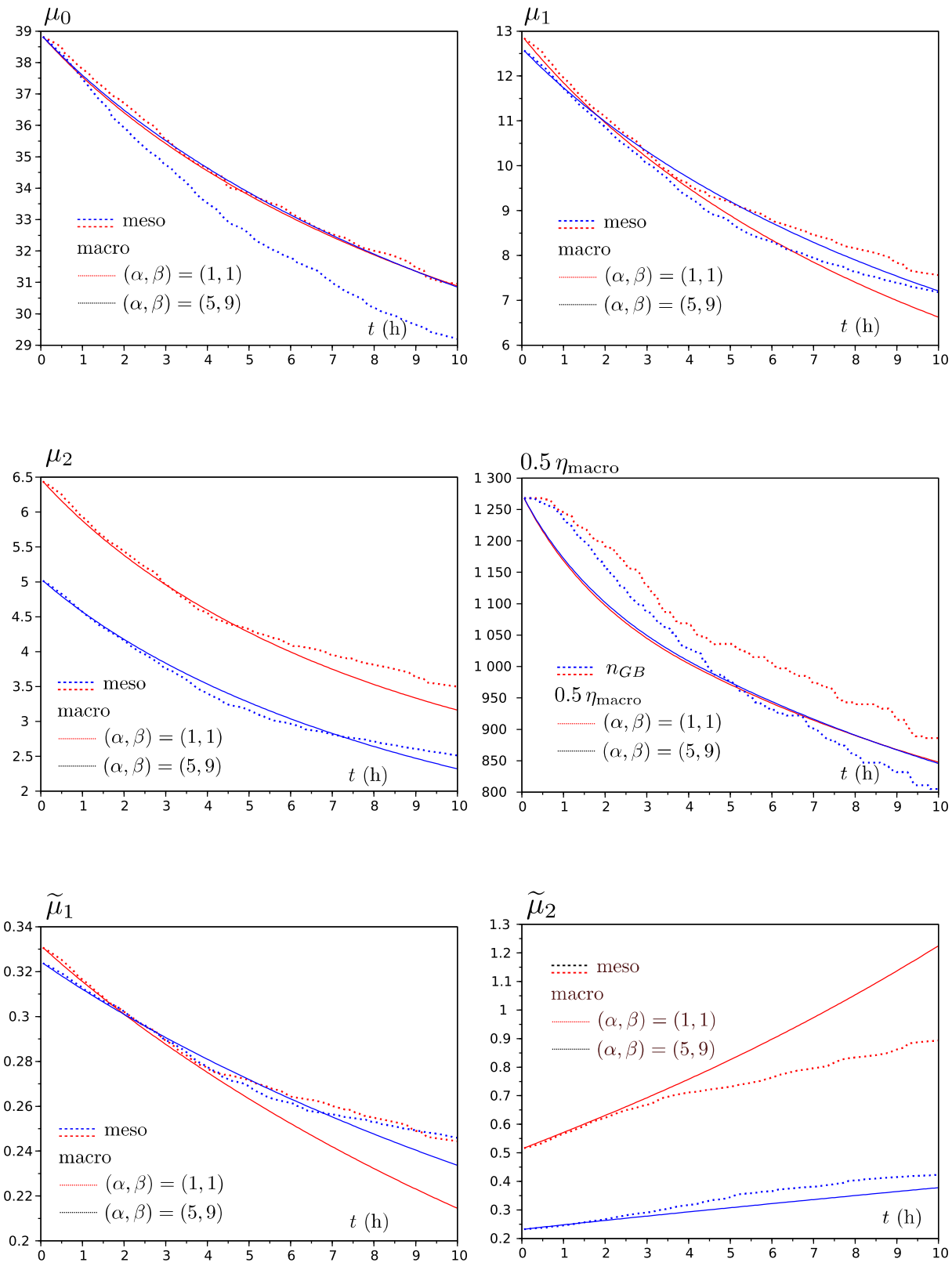

Figure 4.18: Comparison between the overall mesoscopic state and one particular macroscopic state obtained by neglecting the epistemic uncertainty, $i_d = 1$.

wise standard deviations are computed. The comparisons between the overall mesoscopic state $\underline{\mu}_{\text{meso}}, \underline{\eta}_{\text{meso}}$ and the mean macroscopic state $\langle \mu_{\text{macro}} \rangle (t), \langle \eta_{\text{macro}} \rangle (t)$ with point-wise standard deviations $\sigma_{\mu_{\text{macro}}}(t), \sigma_{\eta_{\text{macro}}}(t)$ are presented for the different tested conditions in figures 4.19, 4.20 and 4.21 for $i_d \in \{1, 80, 100\}$ and in figure 4.22 for the 4 tessellations, which do not belong to the database (i.e., $i_d = 0$). The zone defined by more or less one standard deviation is centered on the median and not the mean in case the distribution is not symmetrical (e.g., $\widetilde{\mu}_2$). Results show that the macroscopic model is satisfying, as mesoscopic evolutions lie for the most part in the zone defined by more or less one standard deviation around the median.

It should be noted that the mesoscopic "events", which are not easily captured by the macroscopic model are more likely for tessellations whose morphological textures are very pronounced (i.e., $i_d = 80$ or $i_d = 100$). This is a general trend that has been checked for many other tessellations. Nevertheless, the macroscopic model proposed in this study seems sufficiently accurate to carry on macroscopic simulation of annealing processes or large fabrication or forming processes with heterogeneous and unsteady temperature.

In figure 4.22 all the four mesoscopic evolutions are stacked in one half of the zone defined by the point-wise standard deviation for μ_1, μ_2. This observation could rise the idea that there is a bias, that is to say a systematic error in the estimation of the mean evolution. However, this is likely due to the fact that all the four evolutions have been obtained from similar tessellations to facilitate the search of almost identical initial overall mesoscopic states $\underline{\mu}_{\text{meso}}(t = 0), \underline{\eta}_{\text{meso}}(t = 0)$. Since the macroscopic model has been identified by using very different tessellations, the epistemic uncertainty reflects this diversity, and the macroscopic results spread on a larger zone than if similar tessellations were used for the identification. Thus, for some applications, if equiaxed grains are the most likely mesoscopic structure, the macroscopic model could be identified with a specific database, which only involves such tessellations, and therefore the epistemic uncertainty could be reduced.

4.8.3 Average grain size

Results obtained in section 4.8.2 provide interesting information such as the GB length density per unit area μ_0 / L_0, the average misorientation $\widetilde{\mu}_1$ (rad), the square of the relative standard deviation $\widetilde{\mu}_2$, and the standard deviation that can be obtained from $\widetilde{\mu}_1, \widetilde{\mu}_2$. In addition to these statistical descriptors of the polycrystalline structure, a morphological quantity is also known η_{macro}. Furthermore, the following analysis enables to identify the average grain size evolution. The dimensionless average grain size reads:

$$S_{\text{meso}} = \frac{1}{n} \sum_{k=1}^{n} S_k \tag{4.73}$$

where n is the number of grains in the RVE and S_k are the dimensionless grain surfaces. A macroscopic estimation of the number of grains n_{macro} is obtained from η_{macro}. Indeed, since for each grain that disappears $0.5 \dot{\eta}_{\text{macro}} \approx \dot{n}_{GB}$ and each grain which disappears is likely to be triangular:

$$\dot{n}_{\text{macro}} \approx \frac{\dot{n}_{GB}}{3} \approx \frac{\dot{\eta}_{\text{macro}}}{6} \tag{4.74}$$

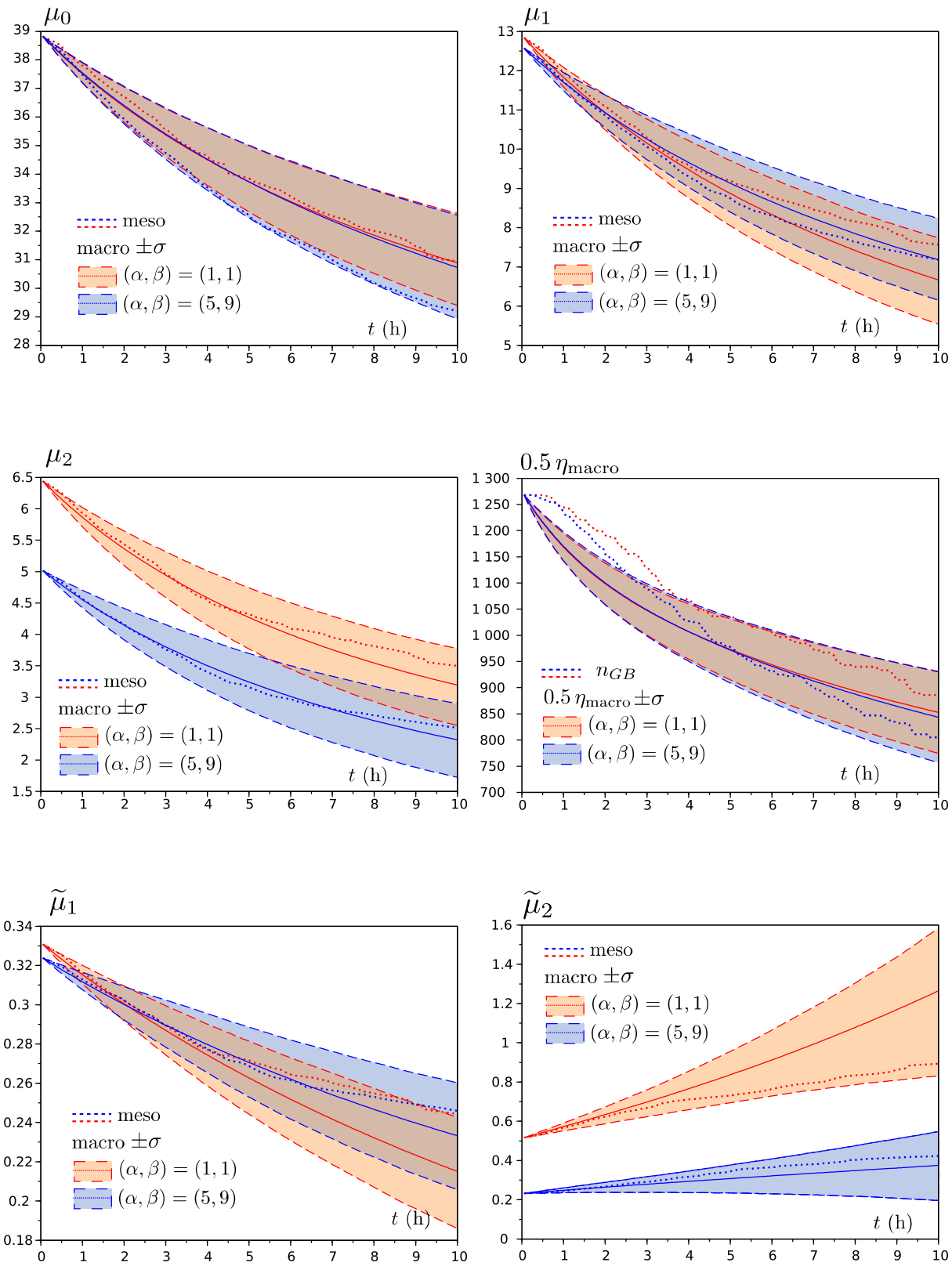

Figure 4.19: Comparison between overall mesoscopic state and macroscopic state with point-wise standard deviation $\pm\sigma$, $i_d = 1$.

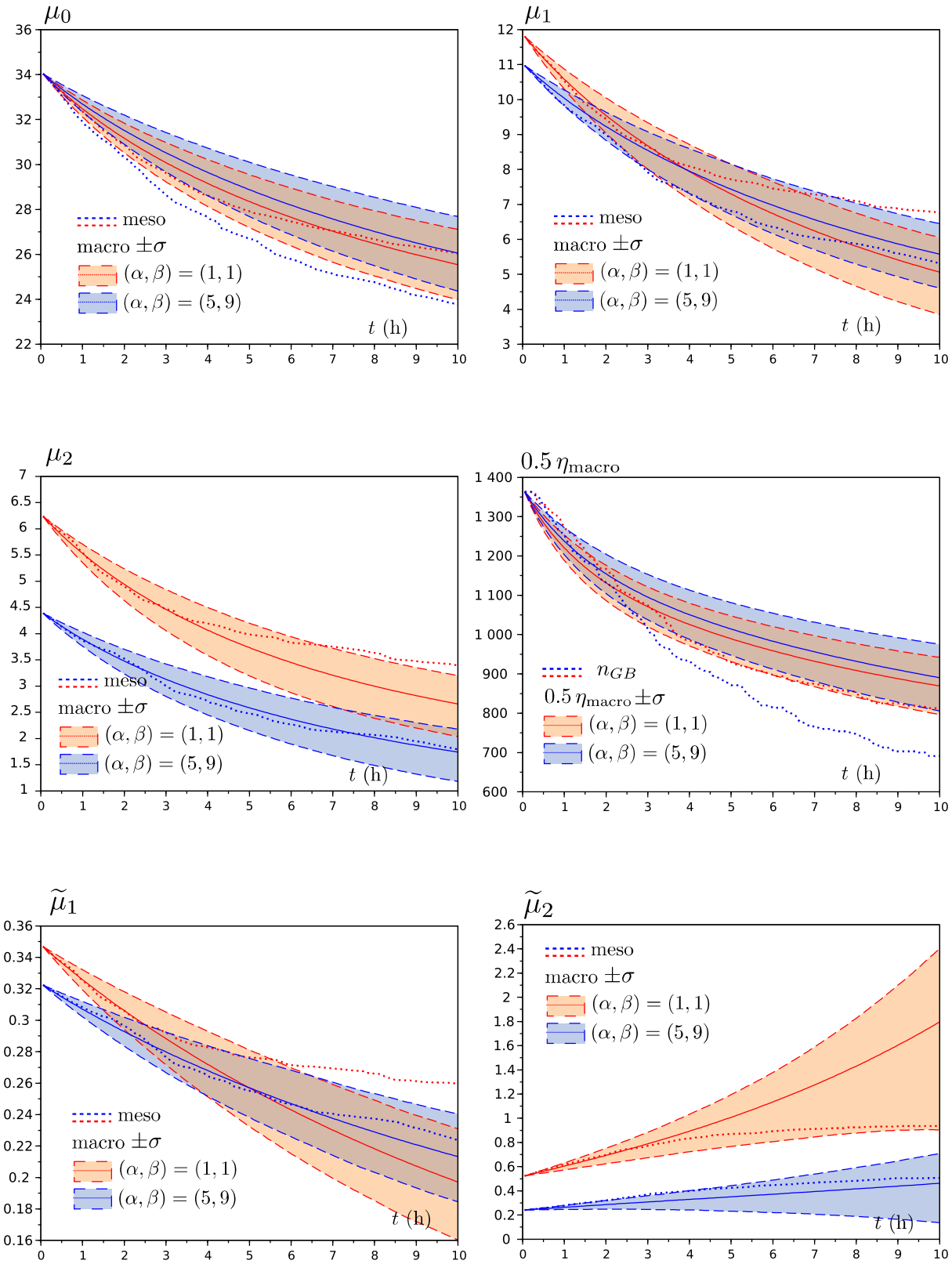

Figure 4.20: Comparison between overall mesoscopic state and macroscopic state with point-wise standard deviation $\pm\sigma$, $i_d = 80$.

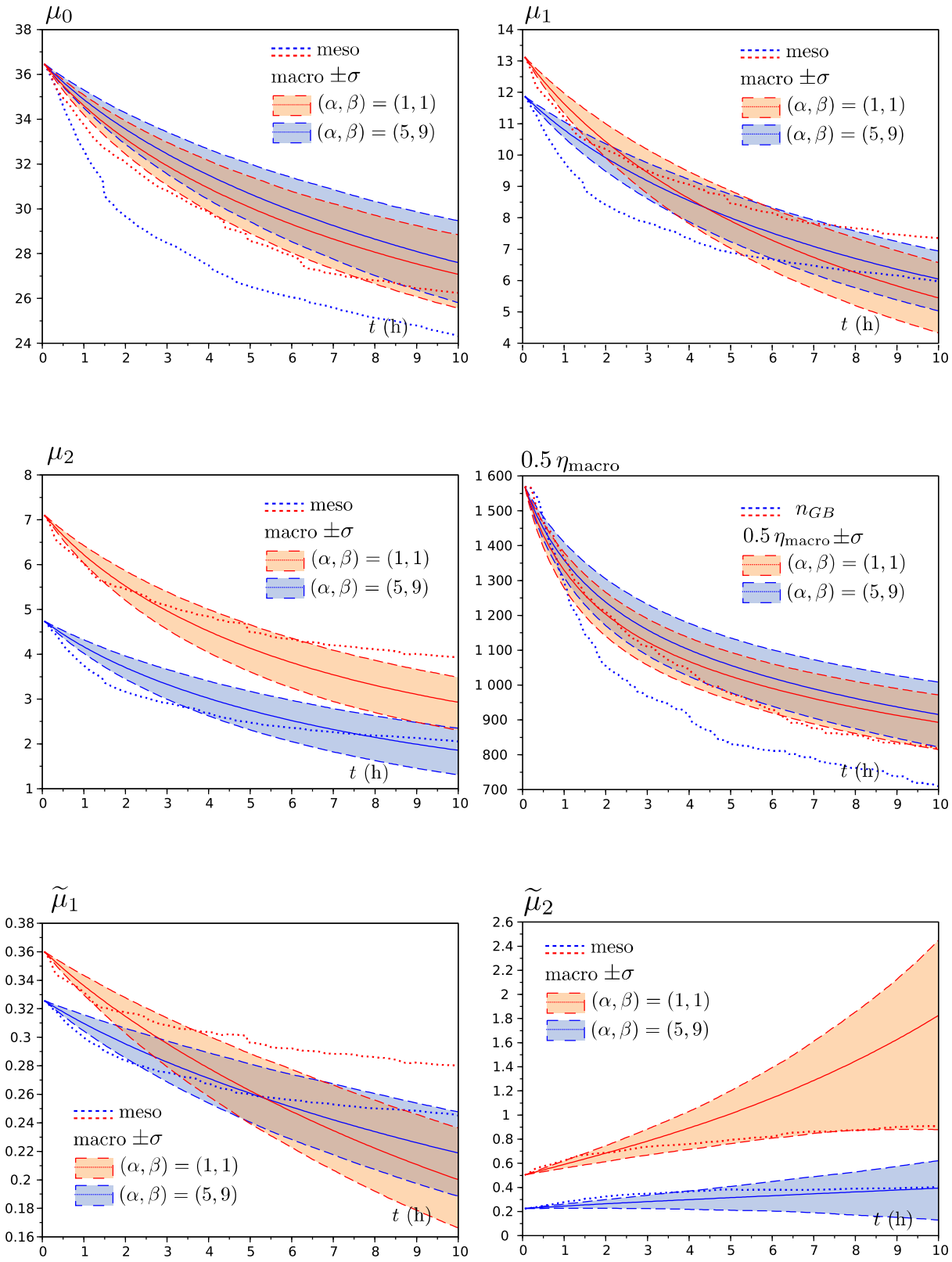

Figure 4.21: Comparison between overall mesoscopic state and macroscopic state with point-wise standard deviation $\pm\sigma$, $i_d = 100$.

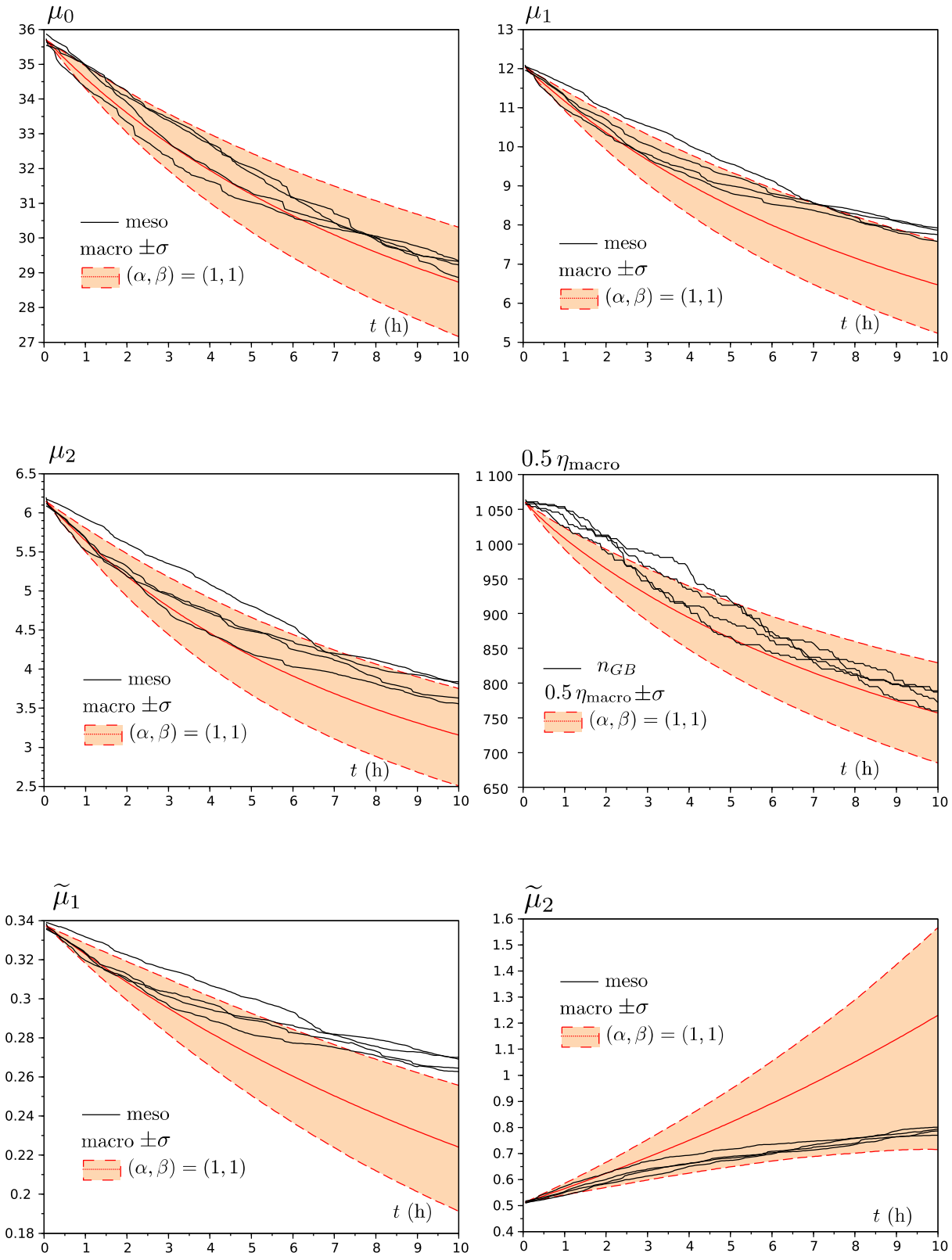

Figure 4.22: Comparison between 4 overall mesoscopic states and macroscopic state with pointwise standard deviation $\pm\sigma$, $i_d = 0$.

In addition the surface of the RVE denoted by $S = \sum_{k=1}^{n} S_k$ is constant as detailed in chapter 3, that is to say $\dot{S} = 0$, thus:

$$\dot{S}_{\text{meso}} = -\frac{\dot{n}}{n^2} S \tag{4.75}$$

Hence the evolution law of the macroscopic average grain size S_{macro} is obtained by replacing in (4.75) the constant surface of the RVE S by $S_{\text{macro}}(t=0)n_{\text{macro}}(t=0)$:

$$\dot{S}_{\text{macro}} = -\frac{\dot{n}_{\text{macro}}}{n_{\text{macro}}^2}(S_{\text{macro}}(t=0)n_{\text{macro}}(t=0)) \tag{4.76}$$

where n_{macro} is computed from (4.74). In figure 4.23 we present the comparison between dimensionless mesoscopic and macroscopic average grain sizes obtained from (4.73) and (4.76) respectively. As for the other statistical estimators of the polycrystalline structure, the average size is satisfying as it lies for the most part in the zone defined by more or less one standard deviation.

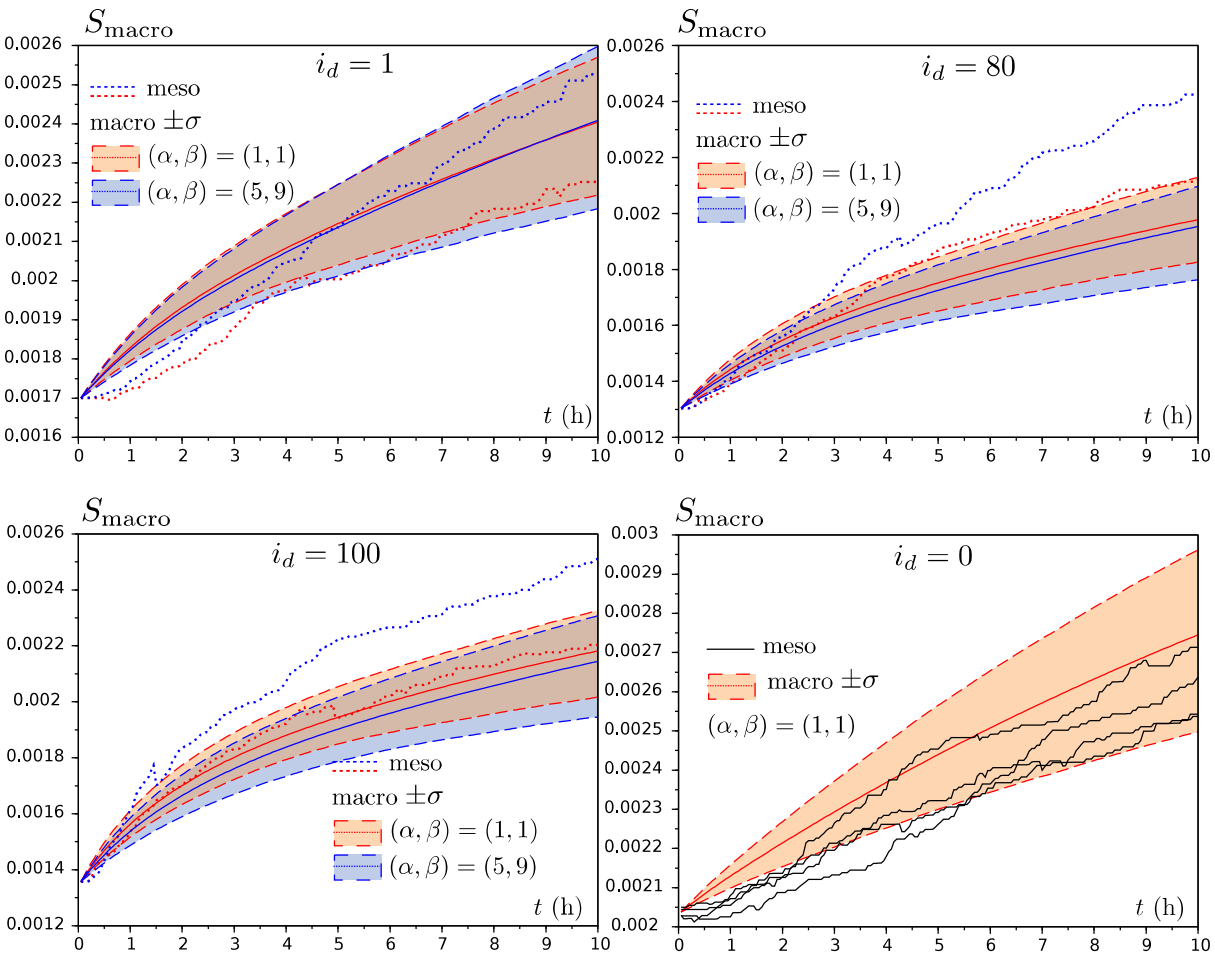

Figure 4.23: Comparison between dimensionless mesoscopic and macroscopic average grain size with point-wise standard deviation $\pm\sigma$.

4.9 Conclusion

In this chapter the macroscopic model has been derived as the final step of the proposed upscaling method. The chosen macroscopic variables fully account for the total energy in a deterministic way, which is essential to compute the macroscopic driving force. In addition, the evolution laws of these macroscopic variables have been established in a rigorous way from the mesoscopic evolution law derived in chapter 3. In the macroscopic evolution laws, a mobility tensor and a vector arise, and have been identified in a *static* approach by using a large database of different and unrelated mesoscopic states in opposition to a *dynamic* approach that would have included mesoscopic evolutions (i.e., successive mesoscopic states). The analysis has shown that an epistemic uncertainty arises from the loss of information due to the reduction of the amount of data encapsulated in the macroscopic state variables in comparison to the mesoscopic state variables. This epistemic uncertainty has been modeled by random variables, whose probability density functions have been estimated by standard Bayesian inference. The macroscopic model is therefore probabilistic and the main result is the mean evolution of the state variables along with point-wise standard deviation.

Results show that the macroscopic model is satisfying as good agreement is observed in the comparisons with particular overall states arising from mesoscopic evolutions. Indeed, the mesoscopic evolutions lie for the most part in the zone defined between more or less one standard deviation. In addition, the computation time is fairly reduced as a few seconds are necessary to compute the entire probabilistic macroscopic evolution, which involves the computation of $N_{\text{stat}} = 500$ particular evolutions. Thus, the proposed approach can be used to carry out simulations of large processes with heterogeneous temperature fields.

The macroscopic model enables to quantify the grain boundary length per unit area μ_0/L_0 and other statistical descriptors of the polycrystalline structure such as the mean misorientation, its standard deviation or the average grain size. Additional morphological descriptors such as grain circularity have not been included in this study, but there is no fundamental difficulties to adapt the proposed work and include such details.

Chapter 5

General conclusion

« *You cannot swim for new horizons until you have courage to lose sight of the shore.* »

William Faulkner

This PhD thesis enabled to establish an original energetic upscaling strategy for grain growth during annealing processes. Indeed, this strategy is based on a thermodynamic framework and accounts for energies and dissipated powers. Such quantities have the same interpretation at all scales and can be summed in order to derive a macroscopic version of the problem. Very different tools were used in order to successfully carry out the different tasks of the project. First and foremost, the use of Voronoi-Laguerre tessellations and associated tensor calculus, along with the thermodynamic analysis that constitutes the bases of this work and differential calculus leading to the evolution law. Moreover, we used various tools associated to the construction of the database and the corresponding statistical treatments, the probabilistic interpolation using classic Bayesian inference and finally the numerical simulation of stochastic differential equations.

We are very well aware of the limitations within which this work has been developed. Indeed, the ambition to have macroscopic state variables that statistically represent the polycrystal and its anisotropies during grain growth is to the best of our knowledge an original contribution, thus no existing and well established methods were found in the literature to rely on. Therefore, to avoid the risk of achieving nothing, our choice was to limit the number of physical phenomena to be considered at the different scales, and to work with a simple model as a proof of concept. Thus, we didn't try to model recrystallization, since the consideration of dislocation density would have led to much more complexity. An other example is phase changes due to crystal rearrangement. Furthermore, we considered simplifying assumptions, the most severe of which is to work in 2D. Even though the obtained model can be applied for plane polycrystals like crystal films, this assumption is a limitation for the applications that we had in mind, namely the classical forming and fabrication processes or more recent processes such as additive manufacturing. However, the considered assumptions enabled us to avoid beig lost in complexity and enabled to focus on theoretical aspects and on the development of a methodology. Nonetheless, a comparison with experimental observations was proposed to make sure that the developed model was sufficiently realistic.

If the extension to 3D does not rise theoretical difficulties in the scope of the proposed approach, the difficulty lies in the search for an analytical grain boundary energy that is function of the five parameters of the 3D grain boundary. Such an interpolation using molecular dynamic computations can be very costly and requires going through the different configurations of the grain boundary. Moreover, the present work raises other research questions. For example, the mesoscopic model developed in this work limited the grain growth kinetics to only the grain weights, although seeds evolution would make the model more versatile as the number of degrees of freedom would be significantly higher. It could also be possible to associate an energy to the triple junctions, since the atomic arrangement at the triple junctions can be even more disrupted than in the grain boundary. The effect of the local inclination angle can also be investigated, due to the dependance of the local grain boundary energy. Major developments can also be considered by using generalized tessellations that are not subjected to the same constraint as Voronoi-Laguerre tessellations, and enable to better account for real polycrystalline structures. The more significant improvement yet would be to include the volume energy density associated with the dislocation density in the grains and the dissipated power associated to their virtual motion. Such considerations would enable us to model nucleation and growth of new grains with no dislocations (i.e., recrystallization). Similarly, we could model phase tran-

sitions by considering the default stack energy and by enabling the system to create new grains (i.e., nucleation) with a different crystal lattice in order to decrease in energy. Of course, nucleation challenges raise several questions in the scope of the OTUM approach, none of which have been developed in this PhD thesis, and are left for future work.

Regarding the macroscopic model, several questions are also left open. Aside from the upscaling of a more complex mesoscopic model (as discussed above), some changes can be adopted directly on the macroscopic model as established in this thesis. For example, we opted for a *static* approach for the database. In other words, the database in composed of different mesoscopic states that are not related to each other, although an other approach could have been to consider mesoscopic structures representing different steps of mesoscopic evolutions. Thus, we were not able to fully understand the evolution in time of the epistemic uncertainty (related to the loss of information due to the reduction of the amount of data in the upscaling strategy). Therefore, we did not update the epistemic uncertainty during the evolution, although its corresponds to the random selection of a virtual mesoscopic state among all the states corresponding to a given macroscopic state, which of course evolves in time. Moreover, some of the morphological indicators of the polycrystal were not taken into account in the macroscopic model (e.g. circularity).

These few perspectives show the amount of work that is still needed so that the upscaling strategy that has been initiated in this PhD thesis can be used by at a larger scale including real applications. However, in spite of all the described limitations, we hope that we contributed with this work to initiate a long-term research topic.

Appendix A

Calculations related to Voronoi-Laguerre tessellation

A.1 Geometrical relationships

The gradient $\partial l_{ij}/\partial \underline{w}$ is obtained by considering the set of triple junctions:

$$I_3 = \left\{(i,j,k) \in \{1,\cdots,n\}^3, C_i \cap C_j \cap C_k \neq \varnothing\right\} \tag{A.1}$$

and the angles at the triple junctions denoted by β_{ijk}, where $(i,j,k) \in I_3$ and where the following symmetry rule holds $\beta_{ijk} = \beta_{kji}$. Triple junctions and the effect of weight variation on the length of the GB is presented figure A.1a. From simple geometrical consideration one obtains:

$$\begin{aligned} \dot{l}_{ij} = & \frac{\tan\left(\beta_{ijk}-\frac{\pi}{2}\right)+\tan\left(\beta_{ijm}-\frac{\pi}{2}\right)}{2d_{ij}}\dot{w}_i^* + \frac{\tan\left(\beta_{jik}-\frac{\pi}{2}\right)+\tan\left(\beta_{jim}-\frac{\pi}{2}\right)}{2d_{ij}}\dot{w}_j^* \\ & -\frac{1}{2d_{jk}\cos\left(\beta_{ijk}-\frac{\pi}{2}\right)}\dot{w}_k^* - \frac{1}{2d_{jm}\cos\left(\beta_{ijm}-\frac{\pi}{2}\right)}\dot{w}_m^* \end{aligned} \tag{A.2}$$

Moreover:

$$\dot{l}_{ij} = \left(\frac{\partial l_{ij}}{\partial \underline{w}}\right).\underline{\dot{w}}^* \tag{A.3}$$

Hence:

$$\frac{\partial l_{ij}}{\partial w_q} = \sum_{p=1}^{n} \widetilde{\delta}_{ijp}\left(\frac{\tan\left(\beta_{ijp}-\frac{\pi}{2}\right)}{2d_{ij}}\delta_{iq} + \frac{\tan\left(\beta_{jip}-\frac{\pi}{2}\right)}{2d_{ij}}\delta_{jq} - \frac{\delta_{pq}}{2d_{jp}\cos\left(\beta_{ijp}-\frac{\pi}{2}\right)}\right) \tag{A.4}$$

where δ_{ij} is th Kronecker symbol and:

$$\widetilde{\delta}_{ijk} = \begin{cases} 1 & \text{if} \quad (i,j,k) \in I_3 \\ 0 & \text{if} \quad (i,j,k) \notin I_3 \end{cases} \tag{A.5}$$

The gradient $\partial S/\partial \underline{w}$ is obtained by calculating the dimensionless area S_i of a grain i as a function of the heights h_{ij} of the triangles joining the seed i and the grain boundaries l_{ij} (where j denotes the neighboring grains), as shown in figure A.1b.

$$S_i = \frac{1}{2}\sum_{j=1}^{N} \tilde{\delta}_{ij} l_{ij} h_{ij} \tag{A.6}$$

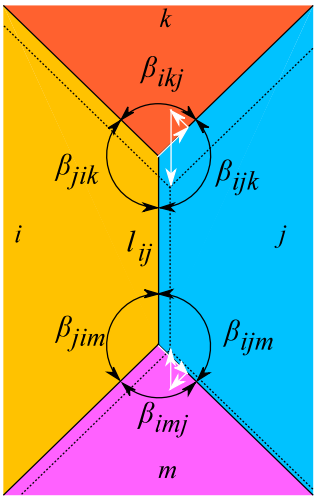

(a) Angles at the triple junctions

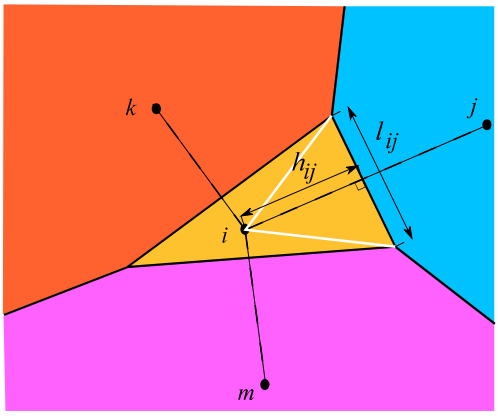

(b) Surface of grains

Figure A.1: Geometrical relationship

where $\tilde{\delta}_{ij} = 1$ if i and j are neighbors (i.e., $(i,j) \in I_{\text{RVE}}$) and $\tilde{\delta}_{ij} = 0$ otherwise, and the sum is taken over all the grains in the OT because GBs at the edges of the RVE connect grains not belonging to the RVE. The height h_{ij} is obtained by using the definition of the Voronoi-Laguerre tessellation:

$$h_{ij} = \frac{w_i - w_j + d_{ij}^2}{2d_{ij}} \tag{A.7}$$

Hence:

$$\dot{S}_i = \frac{1}{4}\sum_{j=1}^{N} \frac{\tilde{\delta}_{ij}}{d_{ij}} \left[\dot{l}_{ij} \left(w_i - w_j + d_{ij}^2 \right) + l_{ij} \left(\dot{w}_i - \dot{w}_j \right) \right] \tag{A.8}$$

Moreover:

$$\dot{S}_i = \frac{\partial S_i}{\partial \underline{w}} \cdot \underline{\dot{w}} \tag{A.9}$$

Hence:

$$\frac{\partial S_i}{\partial w_q} = \frac{1}{4}\sum_{j=1}^{n} \frac{\tilde{\delta}_{ij}}{d_{ij}} \left[\left(w_i - w_j + d_{ij}^2 \right) \frac{\partial l_{ij}}{\partial w_q} + \left(\delta_{iq} - \delta_{jq} \right) l_{ij} \right] \tag{A.10}$$

Hence:

$$\frac{\partial S}{\partial w_q} = \frac{1}{4}\sum_{i=1}^{n}\sum_{j=1}^{N} \frac{\tilde{\delta}_{ij}}{d_{ij}} \left[\left(w_i - w_j + d_{ij}^2 \right) \frac{\partial l_{ij}}{\partial w_q} + \left(\delta_{iq} - \delta_{jq} \right) l_{ij} \right] \tag{A.11}$$

where the sum on i is taken over grains belonging to the RVE.

A.2 Calibration with respect to curvature driven evolution law

The shrinkage of a circular grain in an infinite matrix with a misorientation $\Delta\theta$ is modeled according to according to the curvature driven evolution law (1.1). To calibrate the mobility $m(T)$ introduced in (3.22), the shrinkage of an hexagonal grain is modeled by OTUM as

shown in figure A.2. From (A.4) one obtains for the situation defined in figure A.2:

$$\forall j \in \{2,\cdots,7\}, \frac{\partial l_{1j}}{\partial w_1} = \frac{\partial l_{1j}}{\partial w_j} = -\frac{\partial l_{1j}}{\partial w_{j-1}} = -\frac{\partial l_{1j}}{\partial w_{j+1}} = \frac{1}{2\sqrt{3}R} \tag{A.12}$$

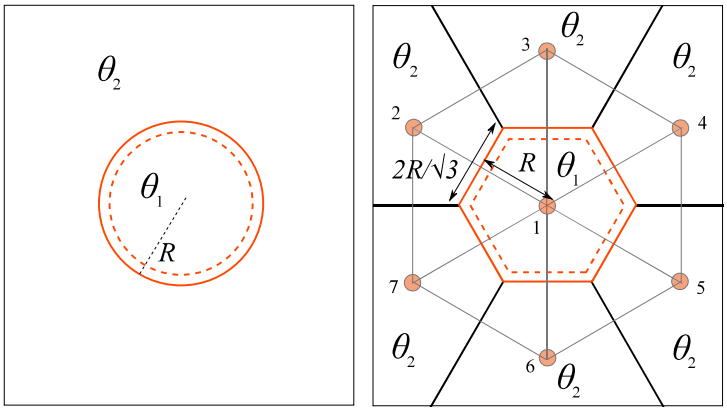

Figure A.2: Circular grain shrinkage in an infinite matrix

The second order tensor $\underline{\underline{\chi}}$ introduced in (3.31) reads:

$$\underline{\underline{\chi}} = \frac{2R}{\sqrt{3}} \frac{X(\Delta\theta)}{m(T)} \underline{\underline{I}} \tag{A.13}$$

Thus, the second order tensor $\underline{\underline{R}}$ introduced in (3.36) and it pseudo-inverse $\underline{\underline{M}}$ introduced in (3.53) are computed. Hence the evolution law (3.52) for the hexagonal situation can be used to obtain $\underline{\dot{w}}_{\text{meso}}$, and by using (3.32) one obtains the inward normal speed according to the proposed model:

$$v_{CD} = \frac{m(T)}{R} \frac{\gamma(T,\Delta\theta)}{X(\Delta\theta)} \tag{A.14}$$

Combining (1.1) and (A.14) one obtains:

$$m(T) = m_{CD}(T,\Delta\theta) X(\Delta\theta) \tag{A.15}$$

Bibliography

[1] W. T. Read, W. Shockley, Dislocation models of crystal grain boundaries, Physical review 78 (1950) 275.

[2] J. Humphreys, G. Rohrer, A. Rollett, Recrystallization and related annealing phenomena, Elsevier, 2017. Third edition.

[3] P. W. Nele Moelans, Bart Blanpain, An introduction to phase-field modeling of microstructure evolution., Calphad 32 (2008) 268–294.

[4] K. Hackl, Generalized standard media and variational principles in classical and finite strain elastoplasticity, Journal of the Mechanics and Physics of Solids 45 (1997) 667–688.

[5] M. A. Miodownik, A review of microstructural computer models used to simulate grain growth and recrystallisation in aluminium alloys, Journal of Light Metals 2 (2002) 125–135.

[6] D. Kandel, E. Domany, Rigorous derivation of domain growth kinetics without conservation laws, Journal of Statistical Physics 58 (1990) 685–706.

[7] E. A. Holm, G. N. Hassold, M. A. Miodownik, On misorientation distribution evolution during anisotropic grain growth, Acta Materialia 49 (2001) 2981–2991.

[8] E. A. Holm, M. A. Miodownik, A. D. Rollett, On abnormal subgrain growth and the origin of recrystallization nuclei, Acta Materialia 51 (2003) 2701–2716.

[9] J. Gruber, H. Miller, T. Hoffmann, G. Rohrer, A. Rollett, Misorientation texture development during grain growth. part i: Simulation and experiment, Acta Materialia 57 (2009) 6102–6112.

[10] L. Zhang, A. D. Rollett, T. Bartel, D. Wu, M. T. Lusk, A calibrated Monte Carlo approach to quantify the impacts of misorientation and different driving forces on texture development, Acta Materialia 60 (2012) 1201–1210.

[11] A. Kuprat, D. George, G. Straub, M. C. Demirel, Modeling microstructure evolution in three dimensions with grain3d and lagrit, Computational Materials Science 28 (2003) 199–208.

[12] J. Gruber, D. C. George, A. P. Kuprat, G. S. Rohrer, A. D. Rollett, Effect of anisotropic grain boundary properties on grain boundary plane distributions during grain growth, Scripta materialia 53 (2005) 351–355.

[13] H. a. Hallberg, Influence of anisotropic grain boundary properties on the evolution of grain boundary character distribution during grain growtha 2d level set study, Modelling and Simulation in Materials Science and Engineering 22 (2014) 085005.

[14] B. Scholtes, R. Boulais-Sinou, A. Settefrati, D. P. Muñoz, I. Poitrault, A. Montouchet, N. Bozzolo, M. Bernacki, 3d level set modeling of static recrystallization considering stored energy fields, Computational Materials Science 122 (2016) 57–71.

[15] J. Fausty, N. Bozzolo, M. Bernacki, A 2d level set finite element grain coarsening study with heterogeneous grain boundary energies, Applied Mathematical Modelling 78 (2020) 505–518.

[16] N. Ma, A. Kazaryan, S. Dregia, Y. Wang, Computer simulation of texture evolution during grain growth: effect of boundary properties and initial microstructure, Acta Materialia 52 (2004) 3869–3879.

[17] C. Krill Iii, L.-Q. Chen, Computer simulation of 3-D grain growth using a phase-field model, Acta materialia 50 (2002) 3059–3075.

[18] L. Vanherpe, N. Moelans, B. Blanpain, S. Vandewalle, Bounding box framework for efficient phase field simulation of grain growth in anisotropic systems, Computational Materials Science 50 (2011) 2221–2231.

[19] G. Abrivard, E. P. Busso, S. Forest, B. Appolaire, Phase field modelling of grain boundary motion driven by curvature and stored energy gradients. part i: theory and numerical implementation, Philosophical magazine 92 (2012) 3618–3642.

[20] G. Abrivard, E. P. Busso, S. Forest, B. Appolaire, Phase field modelling of grain boundary motion driven by curvature and stored energy gradients. part ii: application to recrystallisation, Philosophical magazine 92 (2012) 3643–3664.

[21] K. Chang, N. Moelans, Effect of grain boundary energy anisotropy on highly textured grain structures studied by phase-field simulations, Acta Materialia 64 (2014) 443–454.

[22] M. Upmanyu, D. Srolovitz, L. Shvindlerman, G. Gottstein, Misorientation dependence of intrinsic grain boundary mobility: simulation and experiment, Acta materialia 47 (1999) 3901–3914.

[23] M. Upmanyu, D. Srolovitz, L. Shvindlerman, G. Gottstein, Molecular dynamics simulation of triple junction migration, Acta materialia 50 (2002) 1405–1420.

[24] M. Upmanyu, D. J. Srolovitz, A. Lobkovsky, J. A. Warren, W. Carter, Simultaneous grain boundary migration and grain rotation, Acta Materialia 54 (2006) 1707–1719.

[25] F. Humphreys, Modelling mechanisms and microstructures of recrystallisation, Materials Science and Technology 8 (1992) 135–144.

[26] F. Wakai, N. Enomoto, H. Ogawa, Three-dimensional microstructural evolution in ideal grain growthgeneral statistics, Acta Materialia 48 (2000) 1297–1311.

[27] M. Syha, D. Weygand, A generalized vertex dynamics model for grain growth in three dimensions, Modelling and Simulation in Materials Science and Engineering 18 (2009) 015010.

[28] A. Vondrous, M. Reichardt, B. Nestler, Growth rate distributions for regular two-dimensional grains with ReadShockley grain boundary energy, Modelling and Simulation in Materials Science and Engineering 22 (2014) 025014.

[29] R. Quey, P. Dawson, F. Barbe, Large-scale 3d random polycrystals for the finite element method: Generation, meshing and remeshing, Computer Methods in Applied Mechanics and Engineering 200 (2011) 1729–1745.

[30] H. Telley, T. M. Liebling, A. Mocellin, F. Righetti, Simulating and modelling grain growth as the motion of a weighted voronoi diagram, in: Materials Science Forum, volume 94, Trans Tech Publ, pp. 301–306.

[31] E. Schüle, A justification of the hillert distribution by spatial grain growth simulation performed by modifications of laguerre tessellations, Computational materials science 5 (1996) 277–285.

[32] G. S. Rohrer, Grain boundary energy anisotropy: a review, Journal of materials science 46 (2011) 5881–5895.

[33] S. Plimpton, Fast parallel algorithms for short-range molecular dynamics, Journal of computational physics 117 (1995) 1–19.

[34] D. Wolf, Structure-energy correlation for grain boundaries in fcc metalsi. boundaries on the (111) and (100) planes, Acta metallurgica 37 (1989) 1983–1993.

[35] D. Wolf, Structure-energy correlation for grain boundaries in fcc metalsii. boundaries on the (110) and (113) planes, Acta Metallurgica 37 (1989) 2823–2833.

[36] D. Wolf, Structure-energy correlation for grain boundaries in fcc metalsiii. symmetrical tilt boundaries, Acta metallurgica et materialia 38 (1990) 781–790.

[37] D. Wolf, Structure-energy correlation for grain boundaries in fcc metalsiv. asymmetrical twist (general) boundaries, Acta Metallurgica et Materialia 38 (1990) 791–798.

[38] M. Tschopp, D. McDowell, Asymmetric tilt grain boundary structure and energy in copper and aluminium, Philosophical Magazine 87 (2007) 3871–3892.

[39] M. A. Tschopp, S. P. Coleman, D. L. McDowell, Symmetric and asymmetric tilt grain boundary structure and energy in cu and al (and transferability to other fcc metals), Integrating Materials and Manufacturing Innovation 4 (2015) 11.

[40] S. Ratanaphan, D. L. Olmsted, V. V. Bulatov, E. A. Holm, A. D. Rollett, G. S. Rohrer, Grain boundary energies in body-centered cubic metals, Acta Materialia 88 (2015) 346–354.

[41] P. Van Beers, V. Kouznetsova, M. Geers, M. Tschopp, D. McDowell, A multiscale model of grain boundary structure and energy: From atomistics to a continuum description, Acta Materialia 82 (2015) 513–529.

[42] V. V. Bulatov, B. W. Reed, M. Kumar, Grain boundary energy function for fcc metals, Acta Materialia 65 (2014) 161–175.

[43] S. Foiles, M. Baskes, M. S. Daw, Embedded-atom-method functions for the fcc metals cu, ag, au, ni, pd, pt, and their alloys, Physical review B 33 (1986) 7983.

[44] H. Chamati, N. Papanicolaou, Y. Mishin, D. Papaconstantopoulos, Embedded-atom potential for fe and its application to self-diffusion on fe (1 0 0), Surface Science 600 (2006) 1793–1803.

[45] K. Hackl, F. D. Fischer, On the relation between the principle of maximum dissipation and inelastic evolution given by dissipation potentials, Proceedings of the Royal Society A: Mathematical, Physical and Engineering Sciences 464 (2007) 117–132.

[46] J. Burke, Some factors affecting the rate of grain growth in metals, Aime Trans 180 (1949) 73–91.

[47] J. Burke, D. Turnbull, Prog. metal phys.(eds) b chalmers and r king, 1952.

[48] R. Viswanathan, C. Bauer, Kinetics of grain boundary migration in copper bicrystals with [001] rotation axes, Acta Metallurgica 21 (1973) 1099–1109.

[49] D. Demianczuk, K. Aust, Effect of solute and orientation on the mobility of near-coincidence tilt boundaries in high-purity aluminum, Acta Metallurgica 23 (1975) 1149–1162.

[50] Y. Huang, F. Humphreys, Measurements of grain boundary mobility during recrystallization of a single-phase aluminium alloy, Acta Materialia 47 (1999) 2259–2268.

[51] G. Gottstein, L. S. Shvindlerman, Grain boundary migration in metals: thermodynamics, kinetics, applications, CRC press, 2009.

[52] F. Humphreys, Review grain and subgrain characterisation by electron backscatter diffraction, Journal of materials science 36 (2001) 3833–3854.

[53] R. Sun, C. Bauer, Tilt boundary migration in nacl bicrystals, Acta Metallurgica 18 (1970) 639–647.

[54] F. Humphreys, Y. Huang, Title, in: Conf. Proc.Proceedings of the 21st Risø International Symposium on Materials Science: Recrystallization–Fundamental Aspects and Relations to Deformation Microstructure, ed. N. Hansen et al., Denmark, p. 71.

[55] R. Sandström, On recovery of dislocations in subgrains and subgrain coalescence, Acta Metallurgica 25 (1977) 897–904.

[56] R. Ørsund, E. Nes, Subgrain growth during annealing of heavily deformed metals, Scripta metallurgica 23 (1989) 1187–1192.

[57] Y. Huang, F. Humphreys, Transient dynamic recrystallization in an aluminium alloy subjected to large reductions in strain rate, Acta materialia 45 (1997) 4491–4503.

[58] Y. Huang, F. Humphreys, M. Ferry, The annealing behaviour of deformed cube-oriented aluminium single crystals, Acta Materialia 48 (2000) 2543–2556.

[59] M. Brocato, A. Ehrlacher, P. Tamagny, Détermination de la dissipation caractéristique dans la propagation d'un front de recristallisation, Comptes Rendus de l'Académie des Sciences-Series IIB-Mechanics-Physics-Astronomy 327 (1999) 179–184.

[60] M. Brocato, A. Ehrlacher, P. Tamagny, Stability of discontinuities in polycrystals, Waves and Stability in Continuous Media (1999) 57.

[61] F. Humphreys, A unified theory of recovery, recrystallization and grain growth, based on the stability and growth of cellular microstructuresI. the basic model, Acta Materialia 45 (1997) 4231–4240.

[62] F. Humphreys, Stability and growth of grain and subgrain structures in two-phase materials, in: Third international conference in grain growth in polycrystalline materials, volume 1, Minerals, Metals and Materials Society, 1998, pp. 13–22.

[63] M. Anderson, D. Srolovitz, G. Grest, P. Sahni, Computer simulation of grain growthi. kinetics, Acta metallurgica 32 (1984) 783–791.

[64] J. Von Neumann, Metal interfaces, American Society for Metals, Cleveland 108 (1952).

[65] W. W. Mullins, Two-dimensional motion of idealized grain boundaries, Journal of Applied Physics 27 (1956) 900–904.

[66] D. Moldovan, D. Wolf, S. Phillpot, A. Haslam, Mesoscopic simulation of two-dimensional grain growth with anisotropic grain-boundary properties, Philosophical Magazine A 82 (2002) 1271–1297.

[67] M. Hillert, On the theory of normal and abnormal grain growth, Acta metallurgica 13 (1965) 227–238.

[68] A. Rollett, W. Mullins, On the growth of abnormal grains, Scripta materialia 36 (1997).

[69] P. Rios, Comparison between a computer simulated and an analytical grain size distribution, Scripta materialia 40 (1999) 665–668.

[70] W. Fayad, C. Thompson, H. Frost, Steady-state grain-size distributions resulting from grain growth in two dimensions, Scripta materialia 40 (1999) 1199–1204.

[71] D. Piot, G. Smagghe, J. J. Jonas, C. Desrayaud, F. Montheillet, G. Perrin, A. Montouchet, G. Kermouche, A semitopological mean-field model of discontinuous dynamic recrystallization, Journal of materials science 53 (2018) 8554–8566.

[72] P. De Micheli, L. Maire, D. Cardinaux, C. Moussa, N. Bozzolo, M. Bernacki, Digimu®: Full field recrystallization simulations for optimization of multi-pass processes, in: AIP Conference Proceedings, volume 2113, AIP Publishing LLC, p. 040014.

[73] O. S. J. Merriman Barry, Bence James K., Motion of multiple junctions: A level set approach, Journal of Computational Physics 112 (1994) 334–363.

[74] M. Bernacki, Y. Chastel, T. Coupez, R. E. Logé, Level set framework for the numerical modelling of primary recrystallization in polycrystalline materials, Scripta Materialia 58 (2008) 1129–1132.

[75] A. Agnoli, N. Bozzolo, R. Logé, J.-M. Franchet, J. Laigo, M. Bernacki, Development of a level set methodology to simulate grain growth in the presence of real secondary phase particles and stored energy–application to a nickel-base superalloy, Computational Materials Science 89 (2014) 233–241.

[76] A. Ask, S. Forest, B. Appolaire, K. Ammar, O. U. Salman, A cosserat crystal plasticity and phase field theory for grain boundary migration, Journal of the Mechanics and Physics of Solids 115 (2018) 167–194.

[77] A. Ask, S. Forest, B. Appolaire, K. Ammar, A cosserat–phase-field theory of crystal plasticity and grain boundary migration at finite deformation, Continuum Mechanics and Thermodynamics 31 (2019) 1109–1141.

[78] J. W. Samuel M.Allen, A microscopic theory for antiphase boundary motion and its application to antiphase domain coarsening, Acta Metallurgica 27 (1979) 1085–1095.

[79] R.-J. Jhan, P. Bristowe, A molecular dynamics study of grain boundary migration without the participation of secondary grain boundary dislocations, Scripta Metallurgica et Materialia 24 (1990) 1313–1318.

[80] S. Sakout, D. Weisz-Patrault, A. Ehrlacher, Energetic upscaling strategy for grain growth. I: Fast mesoscopic model based on dissipation, Acta Materialia 196 (2020) 261–279.

[81] D. Weisz-Patrault, S. Sakout, A. Ehrlacher, Fast simulation of grain growth based on orientated tessellation updating method, Mechanics & Industry (2020 (in press)).

[82] A. L. Cruz-Fabiano, R. Logé, M. Bernacki, Assessment of simplified 2d grain growth models from numerical experiments based on a level set framework, Computational materials science 92 (2014) 305–312.

[83] J. Zhang, Y. Zhang, W. Ludwig, D. Rowenhorst, P. W. Voorhees, H. F. Poulsen, Three-dimensional grain growth in pure iron. part i. statistics on the grain level, Acta Materialia 156 (2018) 76–85.

[84] J. Mackenzie, Second paper on statistics associated with the random disorientation of cubes, Biometrika 45 (1958) 229–240.

[85] M. Miodownik, A. Godfrey, E. Holm, D. Hughes, On boundary misorientation distribution functions and how to incorporate them into three-dimensional models of microstructural evolution, Acta materialia 47 (1999) 2661–2668.

[86] M. Groeber, S. Ghosh, M. D. Uchic, D. M. Dimiduk, A framework for automated analysis and simulation of 3d polycrystalline microstructures. part 2: Synthetic structure generation, Acta Materialia 56 (2008) 1274–1287.

[87] E. B. Tadmor, R. S. Elliott, J. P. Sethna, R. E. Miller, C. A. Becker, The potential of atomistic simulations and the knowledgebase of interatomic models, Jom 63 (2011) 17.

[88] D. Wolf, A Read-Shockley model for high-angle grain boundaries, Scripta Metallurgica 23 (1989) 1713–1718.

[89] T. Cheng, D. Fang, Y. Yang, The temperature dependence of grain boundary free energy of solids, Journal of Applied Physics 123 (2018) 085902.

[90] A. Kagawa, T. Okamoto, H. Matsumoto, Young's modulus and thermal expansion of pure iron-cementite alloy castings, Acta Metallurgica 35 (1987) 797–803.

[91] Scilab, Scilab 6.0.0: Free and Open Source software for numerical computation v, Scilab Enterprises, Orsay, France (2019).

[92] S. Sakout, D. Weisz-Patrault, A. Ehrlacher, Energetic upscaling strategy for grain growth. II: Probabilistic macroscopic model identified by Bayesian techniques., Acta Materialia (2020 (submission)).

[93] M. D. Hoffman, A. Gelman, The no-u-turn sampler: adaptively setting path lengths in hamiltonian monte carlo., Journal of Machine Learning Research 15 (2014) 1593–1623.

[94] J. Salvatier, T. V. Wiecki, C. Fonnesbeck, Probabilistic programming in python using pymc3, PeerJ Computer Science 2 (2016) e55.

[95] G. Van Rossum, F. L. Drake, The python language reference manual, Network Theory Ltd., 2011.

[96] R. G. Ghanem, P. D. Spanos, Stochastic finite elements: a spectral approach, Courier Corporation, 2003.

École des Ponts
ParisTech

Titre: Modèle mésoscopique rapide de croissance de grain par mise à jour de tessellations orientées et homogénéisation probabiliste

Résumé: La croissance de grain est un phénomène thermiquement activé qui se produit généralement pendant les phases de recuit des métaux. Pendant la phase de croissance, certains grains grossissent au détriment dautres grains en fonction de leur taille et de leur orientation cristalline. Les descripteurs statistiques classiques du polycristal tels que la texture morphologique et cristallographique (taille des grains, distribution des orientations et des désorientations cristalline) évoluent pendant les procédés. Ainsi, pour différents procédés (ex. fabrication additive), les conditions de température pourraient être optimisées pour cibler des microstructures spécifiques. Cependant, prédire lévolution des microstructures implique de développer des modèles à léchelle du polycristal (joints de grain). Mais cette échelle est incompatible avec des simulations complètes de procédés qui nécessitent une description à large échelle. Le but de ce travail est donc de développer une stratégie de changement déchelle pour établir les bases dun modèle macroscopique de croissance de grain qui repose entièrement sur une description du phénomène aux échelles inférieures et dont les variables détat contiennent les descripteurs statistiques du polycristal. Cette stratégie repose sur une description de la croissance de grain à différentes échelles : (i) atomique (potentiel interatomique et arrangement cristallin), (ii) microscopique (joints de grain), (iii) mésoscopique (polycristal) et (iv) macroscopique (descripteurs statistiques). Puisque les concepts énergétiques existent à toutes les échelles et traversent tous les champs de la physique, notre démarche repose en substance sur différentes contributions énergétiques apparaissant aux différentes échelles. Cette stratégie énergétique est développée dans le cadre des milieux standards généralisés qui sont caractérisés par leur énergie libre et la puissance dissipée dans nimporte quelle évolution virtuelle. Cela consiste donc à déterminer ces potentiels thermodynamiques non pas de manière axiomatique avec des fonctions paramétriques, et une nécessaire calibration expérimentale, mais de manière plus physique et statistique en sappuyant sur la construction dune importante base de données constituée de calculs à léchelle mésoscopique. Sur cette base, nous pouvons identifier une énergie libre et un potentiel de dissipation macroscopiques en fonction de variables détat que nous définirons, pour obtenir une loi dévolution macroscopique qui porte sur les descripteurs statistiques de la microstructure. La base de donnée joue donc un rôle déterminant et nécessite pour être suffisamment riche dutiliser intensivement un modèle de croissance de grain à léchelle mésoscopique. Le temps de calcul de ce modèle est donc critique. Bon nombre dapproches existent, cependant le poids calculatoire est trop important. Un premier travail consiste au développement dun modèle mésoscopique simple et rapide pour créer la base de donnée. Ce modèle est formulé en deux dimensions pour ne pas compliquer les aspects techniques, lenjeu étant principalement de valider notre approche. Nous nous appuyons sur les techniques de tessellation de Voronoi-Laguerre. Des algorithmes très efficaces ont été développés et permettent de générer très rapidement des tessellations avec les orientations cristallines souhaitées. Lidee de notre modèle mésoscopique rapide est donc dapproximer lévolution dun polycristal par une succession de tessellations orientées, que lon met à jour à chaque pas de temps. Lexploitation de la base de donnée révèle un aspect important : la perte dinformation entre léchelle mésoscopique (détaillée) et léchelle macroscopique (statistique) introduit un alea épistémique dans le modèle. Donc, à partir dun modèle mésoscopique entièrement déterministe, nous construisons un modèle macroscopique probabiliste, qui peut être utilisé pour des structures de grande échelle subissant des traitements thermiques.

Title: Energetic upscaling strategy for grain growth

Abstract: Grain growth is a thermally activated phenomenon that generally occurs during annealing processes. During grain growth, some grains grow while others disappear. This coalescence is a function of the grain size and crystal orientation. Classical statistical descriptors of the polycrystalline structure such as morphological and crystallographic textures (e.g., grain size, shape and crystal orientation distributions) evolve during the process. Thus, for different fabrication or forming processes (e.g., additive manufacturing), temperature conditions could be optimized to obtain targeted microstructures, especially for large heterogeneous parts. However, mechanisms involved during grain growth arise at the scale of grain boundaries (GB). Thus, numerical simulations of the evolution of morphological and crystallographic textures may be difficult to perform for macroscopic parts, which hinders the development of optimization loops to adjust process parameters. Therefore, this PhD thesis aims at developing an upscaling strategy to establish a macroscopic model of grain growth that fully relies on finer scales and whose state variables contain statistical descriptors of the grain structure. The proposed upscaling strategy involves considering grain growth at various scales: (i) the atomic scale (e.g., crystal lattice and interatomic potential), (ii) the microscopic scale (e.g., grain boundaries), (iii) the mesoscopic scale (e.g., polycrystalline structure) and (iv) the macroscopic scale (statistical descriptors of the grain structure). As energetic concepts are valid at all scales, the upscaling strategy fundamentally relies on various energetic contributions arising at different scales. This energetic upscaling strategy is developed within the framework of standard generalized media that are caracterized by their free energy and dissipated power. The proposed upscaling strategy consists in determining these two potentials not axiomatically (with parametric functions and experimental calibration), but on a more physical basis by using a large database of results from computations carried out at the mesoscopic scale. On this basis, we can identify the macroscopic free energy and dissipated power as a function of the macroscopic state variables in order to obtain an evolution law that accounts for statistical descriptors of the grain structure. Therefore, the database requires to intensively use a mesoscopic model of grain growth. As a consequence, a sufficiently fast mesoscopic model should be established. Many different approaches have been proposed to model grain growth at the mesoscopic scale. However, the computational cost is usually incompatible with an intensive use as suggested within the proposed framework. In this work, a fast mesoscopic model called Orientated Tessellation Updating Method (OTUM) has been proposed. It fully relies on Voronoi-Laguerre tessellation to approximate polycrystals at the mesoscopic scale. For the sake of simplicity, the proposed upscaling methodology is established for plane hexagonal polycrystals. Very efficient algorithms have been developed with the possibility of controlling statistical distributions of grain size and shape and GB misorientation. OTUM relies on the idea that the evolution law of the mesoscopic structure can be formulated directly by modifying the parameters defining the OT. Exploring and analyzing the database raises an epistemic uncertainty, which corresponds to the loss of information in the process of reducing the amount of data. This epistemic uncertainty has been modeled with random variables, leading to a probabilistic macroscopic model, even though the mesoscopic model is completely deterministic. Such a model can be directly used for structures at large scales subjected to thermal treatments.

Navier

LMS